Title

DEVELOPMENT OF LI[SUP]- AND H[SUP]- ION SOURCES

Author

Walther, S.R

Publication Date

1988-12-01

LBL-26618 c.2

Lawrence Berkeley Laboratory
UNIVERSITY OF CALIFORNIA

Accelerator & Fusion Research Division

Development of Li^- and H^- Ion Sources

S.R. Walther
(Ph.D. Thesis)

December 1988

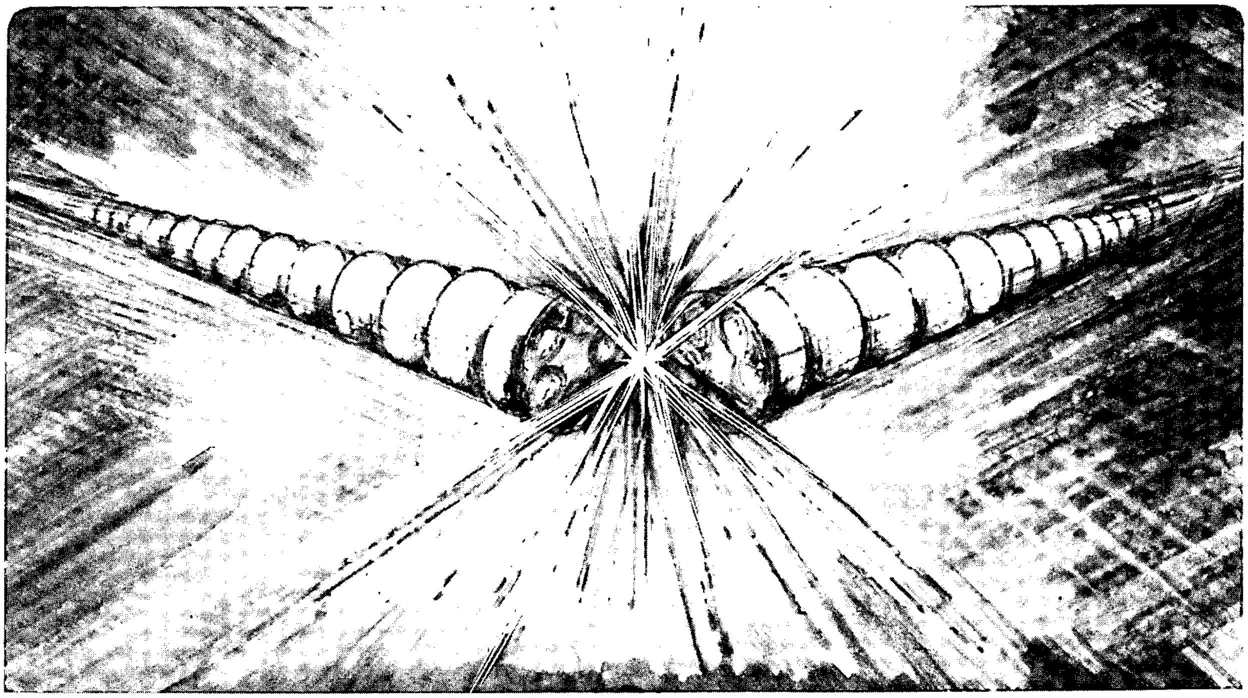

Prepared for the U.S. Department of Energy under Contract Number DE-AC03-76SF00098.

DISCLAIMER

LBL-26618

Development of Li$^-$ and H$^-$ Ion Sources*

Steven R. Walther

Ph.D. Thesis

Accelerator and Fusion Research Division
Lawrence Berkeley Laboratory
University of California
1 Cyclotron Road
Berkeley, CA 94720

December 1988

* This work supported by the Director, Office of Energy Research, Office of Fusion Energy, Development and Technology Division, of the U.S. Department of Energy under Contract No. DE-AC03-76SF00098 and the AFOSR under Contract No. AFOSR-ISSA-88-003.

Development of Li^- and H^- Ion Sources

Steven R. Walther

Accelerator and Fusion Research Division
Lawrence Berkeley Laboratory
University of California
1 Cyclotron Road
Berkeley, CA 94720

Abstract

Sources of Li^- and H^- ions are needed for diagnostic neutral beams and for current drive in fusion plasmas. Previous efforts to generate Li^- beams have focused on electron capture in a gas or production on a low work function surface in a plasma. Volume production of Li^- by dissociative attachment of optically pumped lithium molecules has also been studied. This thesis presents the first experimental results for volume production of a Li^- ion beam from a plasma discharge. A theoretical model for volume production of Li^- ions and separate model for Li_2 production in the lithium discharge are developed to explain the experimental results. The model is in good agreement with the experiment and shows favorable parameter scalings for further improvement of the Li^- ion source. A $^6Li^\circ$ diagnostic neutral beam based on this ion source is proposed for measurement of magnetic pitch angle in the International Thermonuclear Experimental Reactor (ITER).

Previous efforts in developing H^- ion sources have concentrated on volume production in a plasma discharge. Experiments to improve the H^- current density from a magnetically filtered multicusp ion source by seeding the discharge with cesium or barium have been conducted. A substantial (> factor of five) increase in H^- output is achieved for both cesium and barium addition. Further experiments with barium have shown that the increase is due to H^- production on the anode walls. The experiments with cesium are consistent with this formation mechanism. These results show that this new type of 'converterless' surface production H^- source provides greatly improved performance when compared to a volume H^- source.

Dedication

To my parents, Ken and Lois Walther, who are both good experimentalists around the house, for encouraging me to pursue my goals. And also to Kathy Grant, for her support and encouragement.

Table of Contents

Page

Acknowledgements v
List of Figures vii

Chapter 1 Overview of Negative Ion Sources for Fusion Applications 1
Introduction 1
Production of Negative Ions 5
The Filtered Multicusp Ion Source 13
Scope of This Thesis 18
Chapter 2 Theory - The Lithium Ion Source Model 20
Lithium Ion Source Model - First Chamber 21
Lithium Ion Source Model - Second or Extraction Chamber 25
Results for the Lithium Ion Source Model 27
Model for Dimer (Li_2) Formation in the Ion Source . 38
Results for the Dimer Model 43
Summary 50
Chapter 3 Li^- Ion Source - Design and Experiments 52
Source Design and Operation 52
Experimental Measurements for Discharge Evaporation of Lithium 57
1. Dimer Fraction in the Discharge 57
2. Neutral Lithium Density in the Ion Source 60

3. Negative Ion Species and Beam Current 61
4. Plasma Density in the Ion Source 62
5. Time Dependence of the Positive and Negative Ion Output 63
6. Comparison of Theory and Experiment for Li^- Ions 66
7. Comparison of Theory and Experiment for Li_2 Molecules 67
Experiments with a Lithium Oven 68
Shortcomings of These Experiments and Their Implications on Design of Future Negative Lithium Ion Sources 73
Summary 76
Chapter 4 Design of a Lithium Diagnostic Beam to Measure Magnetic Pitch Angle on ITER 77
Introduction 77
Overview of the TEXT Lithium Diagnostic Neutral Beam 78
$^6Li^\circ$ Beam Diagnostic for ITER 82
Conclusion 88
Chapter 5 Production of H^- Ions in a Cesium or Xenon-Seeded Hydrogen Discharge 90
Part I Experiments with a Small Ion Source 91
Experimental Apparatus 91
Experimental Results - Source Operation with Hydrogen and Cesium 91

Experimental Results - Source Operation with Hydrogen and Xenon 100
Discussion 105
Part II Experiments with a Larger High Power Ion Source 107
Experimental Apparatus 108
Experimental Results for Hydrogen-Cesium Operation 110
Part III Conclusion 117
Chapter 6 Production of H^- Ions in a Barium-Seeded Hydrogen Discharge 119
Part I Experiments with a Small Ion Source 119
Part II Experiments with a Larger Ion Source 126
Part III Conclusion 134
Chapter 7 Conclusion 137
Summary of Results 137
Future Research Options 138
Appendix 1 Rate Constants for the Lithium Ion Source Model . 140
References 144

Acknowledgments

A great number of people have been instrumental in assisting me. I thank them all and would like to acknowledge some of them here. Ka-ngo Leung has provided not only ideas, but motivation and support for much of this effort. Wulf Kunkel was always willing to hear the latest results and discuss their interpretation; he also has suggested numerous improvements in this thesis. Ed Morse has also offered many improvements and consistently provided a forum for discussing my experiments. Gary Guethlein and Al Lietzke were invariably available to discuss experimental problems and create theoretical ones, from which I profited greatly. Ken Ehlers and Joe Kwan have given me the benefit of their ion source experience, for low monthly payments. Geoffrey Stutzin, graduate student and conference chauffeur, was always around to discuss the latest success or failure. John Trow's thesis and magnetic field programs were extremely helpful in my work. Cheryl Hauck operated the high power pulsed source with cesium and barium, her help was essential to obtain some of the data in Chapter 5. Fabricating parts in the machine shop was 'no problem' thanks to David Moussa, Steve Wilde, and Mark West. Don Williams, Tom Downs, Dick Heep, Dean Kippenhan, Tom McVeigh, and Bud Leonard, made operating an experiment virtually painless. Peter Purgalis and Warren Stearns helped me to design relatively successful alkali metal ovens. Ken Fowler offered his comments and advice on this thesis. Kathy Grant played the role of thesis editor and will be rewarded by my returning the favor. A final thanks to my ale taste-testing crew who thought my future might be brighter as a brewer, Bill Scharff, Charlie Matuk, Don Williams, Cheryl Hauck, Glenn Ackerman, Ed Morse, Geoffrey Stutzin, and Wulf Kunkel.

This work was supported by the Director, Office of Energy Research, Office of Fusion Energy, Development and Technology Division, of the U.S. Department of Energy under Contract No. DE-AC03-76SF00098 and the AFOSR under Contract No. AFOSR-ISSA-88-003.

List of Figures

Figure 1-1	Schematic Diagram of a Neutral Beamline
Figure 1-2	Maximum Obtainable Neutral Fraction vs. Beam Energy
Figure 1-3	Conceptual Beamline Design for ITER
Figure 1-4	Schematic Diagram of a Double Charge Exchange Neutral Beam System
Figure 1-5	Schematic Diagram of a Surface Converter Negative Ion Source
Figure 1-6	Simplified Potential Energy Curve for Molecular Hydrogen Showing the Ground and an Upper Electronic State
Figure 1-7	A Schematic Diagram of a Volume Negative Ion Source
Figure 1-8	A Computer Plot of the Magnetic Field Produced by the Multicusp Magnets Surrounding the Ion Source. The Upper Half Plot Shows the Field Lines (1, 3, 10, 30 Gauss-cm), and the Lower Half Plot Shows the Field Intensity Contours (1, 3, 10, 30, 100, 300 Gauss).
Figure 2-1	A Plot of the Li^- Current Density vs. First Chamber Electron Density
Figure 2-2	A Plot of the Li^- Current Density vs. the Percentage of Lithium Molecules Present in the Discharge

Figure 2-3 A Plot of the Li^- Current Density vs. Atomic Neutral Density for both Double and Single Chamber Discharge Configurations

Figure 2-4 A Plot of the Li^- Current Density vs. the Length of the Extraction Chamber

Figure 2-5 A Plot of the Li^- Current Density vs. Second Chamber Electron Temperature

Figure 2-6 A Plot of the Lithium Adsorption Energy vs. Lithium Coverage

Figure 2-7 A Plot of the Percentage of Lithium Evaporating as Molecules vs. the Temperature of the Hot Wall Area for the Cases of Fixed and Variable Wall Area

Figure 2-8 A Plot of the Percentage of Lithium Evaporating as Molecules vs. the Neutral Atomic Lithium Density in the Ion Source

Figure 2-9 A Plot of the Percentage of Lithium Evaporating as Molecules vs. the Fraction of the Ion Source Wall that is Hot

Figure 2-10 A Plot of the Lithium Coverage on the Ion Source Walls vs. the Fraction of the Wall Surface that is Hot

Figure 3-1 A Schematic Diagram of the Lithium Ion Source, Mass Separator, and Faraday Cup

Figure 3-2 Mass Spectrometer Traces Showing (a) the Positive Ion Species in the Extracted Beam and (b) the Negative Ion Species in the Extracted Beam

Figure 3-3 Time Dependence of the Positive Lithium Ion Species

Figure 3-4 Time Dependence of the Negative Lithium Ion Current

Figure 3-5 A Schematic Diagram of the Lithium Oven and Ion Source

Figure 3-6 Mass Spectrometer Traces of (a) the Positive Ion Species, and (b) the Negative Ion Species when the Lithium Oven is Used as the Source of Lithium

Figure 4-1 Penetration of TEXT Diagnostic Beam into the TEXT Plasma (a=27 cm)

Figure 4-2 Atomic Lithium Beam Penetration into the ITER Plasma as a Function of Energy

Figure 5-1 A Schematic Diagram of the Small Ion Source

Figure 5-2 Mass Spectrometer Traces of (a) the Positive Ion Species in a Pure Hydrogen Discharge, (b) with Cesium Added, and (c) at Low Extraction Voltage with Cesium Added

Figure 5-3 Mass Spectrometer Traces of (a) the Negative Ion Species in a Pure Hydrogen Discharge, (b) with Cesium Added

Figure 5-4 A Graph of the H^- Output Signal as a Function of the Cesium Oven Temperature

Figure 5-5 A Graph of the H^- Output Signal as a Function of Hydrogen and Xenon Partial Pressures

Figure 5-6 A Graph of the H^- Output Measured by the Mass Spectrometer and the Faraday Cup as a Function of the Hydrogen Pressure

Figure 5-7 Mass Spectrometer Traces of (a) the Positive Ion Species in a Pure Hydrogen Discharge, (b) with

Xenon Added, and (c) at Low Extraction Voltage with Xenon Added
Figure 5-8 Mass Spectrometer Traces of (a) the Negative Ion Species in a Pure Hydrogen Discharge, and (b) with Xenon Added
Figure 5-9 A Schematic Diagram of the Three Inch Multicusp H^- Ion Source
Figure 5-10 A Graph of the H^- Current Density as a Function of Discharge Current and Cesium Addition (1 mm Aperture)
Figure 5-11 A Graph of the H^- Current Density as a Function of Discharge Current and Cesium Addition
Figure 5-12 A Graph of the Electron to H^- Ion Ratio as a Function of Discharge Current and Cesium Addition
Figure 5-13 An Oscilloscope Picture Showing the Time Dependence of the Discharge Voltage and Current, and the Extracted Electron and H^- Ion Currents
Figure 6-1 A Graph of the Vapor Pressure of Cesium and Barium as a Function of Temperature
Figure 6-2 A Schematic Diagram of the Small Ion Source Seeded with Barium
Figure 6-3 Mass Spectrometer Traces of (a) the Negative Ion Species, (b) the Positive Ion Species for Pure Hydrogen Operation, and (c) the Positive Ion Species or Operation with Barium in the Discharge
Figure 6-4 A Graph of the H^- and Ba^+ Ion Signals as a Function of the Temperature of the Liner

Figure 6-5 A Schematic Diagram of the Three Inch Dual Cathode Ion Source

Figure 6-6 A Plot of Mass Spectrometer Signals for Operation with Pure Hydrogen and (a) a Positive Plasma Potential, or (b) a Negative Plasma Potential Produced by Injection of Low Energy Electrons

Figure 6-7 An Illustration of the Relation Between the Energy of an H^- Ion and the Potential of the Source Plasma for Volume and Surface-Produced H^- Ions

Figure 6-8 A Plot of Mass Spectrometer Signals for Operation with (a) a Positive Plasma Potential, and (b) a Negative Plasma Potential Produced by Injection of Low Energy Electrons into the Barium-Seeded Plasma

Chapter I Overview of Negative Ion Sources for Fusion Applications

Introduction

Sources of H^-, D^-, and Li^- ions are needed to generate efficient neutral beams with energies in excess of 150 keV per nucleon for fusion research.[1] For purposes of neutral beam heating and current drive in fusion plasmas, D^- ion beams with energies of 1-2 MeV are considered the most appropriate. Fusion plasma diagnostics using H^- and Li^- ions to generate high energy neutral beams of H° and Li° with energies of .5 to 5 MeV have also been proposed.[2,3,4] Therefore the development of negative ion sources is of considerable importance for fusion applications.

Generation of high energy neutral beams requires production of negative ions, acceleration of these ions to high energies, and then neutralization of these ions to allow penetration of the beam into the magnetic field confining the fusion plasma (Fig. 1-1 from Ref. 5). Before discussing the ion source in detail, some mention should be made of the other components in the beamline. After exiting the ion source, ions enter an accelerator structure which increases ion energy into the MeV range. Development of a new accelerator technology is required at these energies, and is being addressed in several conceptual designs.[6,7] These designs investigate both DC and RF schemes to accelerate ions into the MeV energy range.

Once the ion beam has been accelerated to the desired energy, the beam ions must be neutralized as efficiently as possible. In this case, efficiency is given by the percentage of beam ions

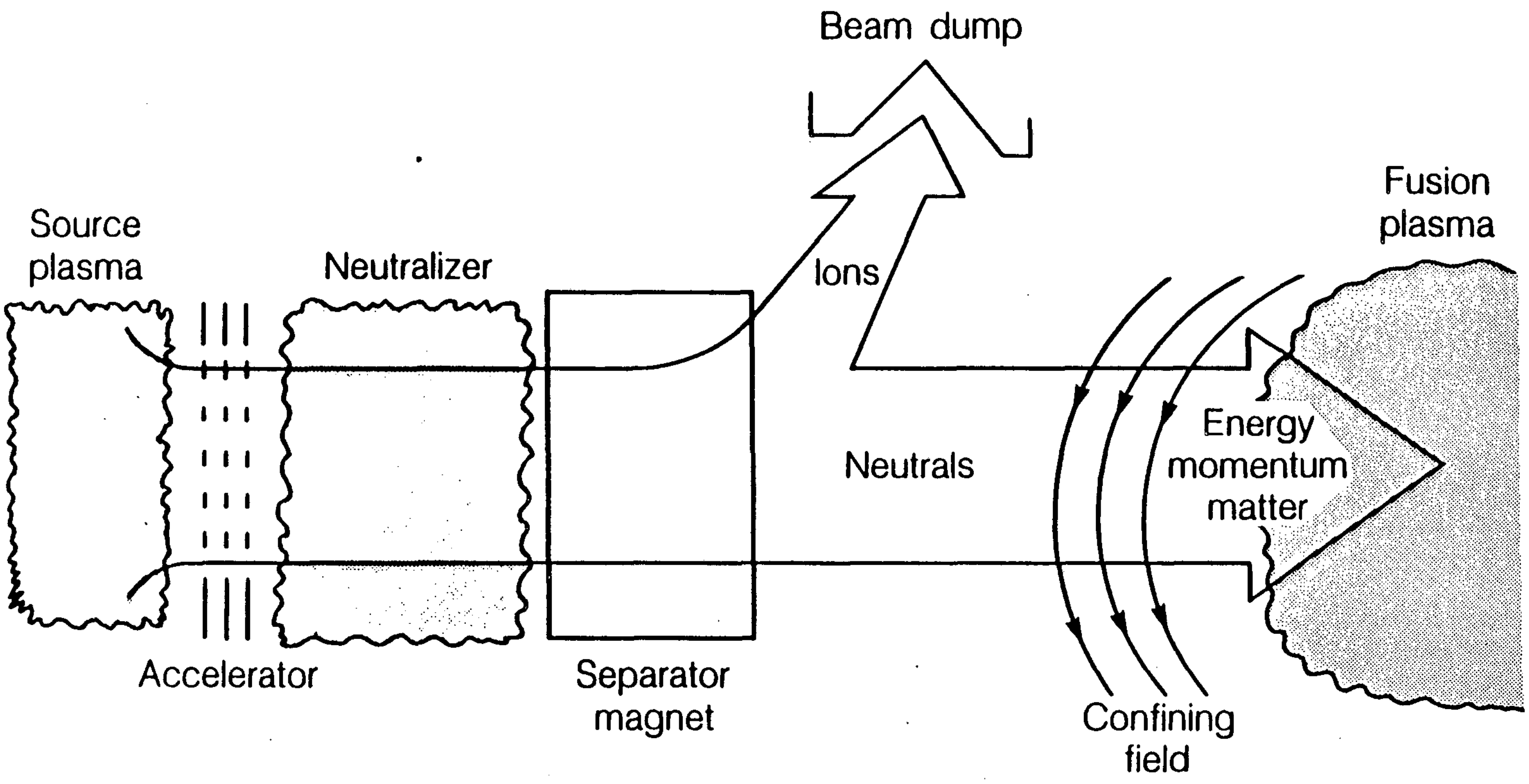

XBL 852-9758

Fig. 1-1 Schematic Diagram of a Neutral Beam Line neutralized. The positive-ion-based neutral beam systems now in use rely on a gas target to neutralize the positive ions. This method becomes very inefficient for energies above 75 keV per nucleon (Fig. 1-2, from ref. 5). However, negative ion based neutral beams can be efficiently neutralized at any energy of interest for fusion applications (Fig. 1-2). With a gas target, efficiencies of ~60% can be obtained, while use of a plasma target can improve this to ~85%. The use of a laser photoneutralizer could provide efficiencies in excess of 95%.

The gas target neutralizer consists of a gas cell containing an optimal 'thickness' or line density of gas atoms or molecules. The beam ions undergo charge exchange or electron detachment when colliding with the neutralizer gas particles and are neutralized. However, subsequent charge exchange between the neutralized beam and the target limits the efficiency obtainable in this type of neutralizer.[8] The plasma neutralizer is a subject of current research.[9] The advantage of using a plasma target is the large neutralization cross-section available. Utilizing plasmas with high ionic charge states enhances this process. The most efficient negative ion beam neutralizer uses a laser to photodetach the weakly bound electron from the negative ion. In this case, the photon energy is large enough to strip the extra electron, but not enough to cause subsequent ionization of the neutralized beam atoms. In theory, a 100% neutralization efficiency can be obtained using this process.

Other components in the neutral beam line include the bending magnet and beam dump. Their purpose is to remove unwanted ions

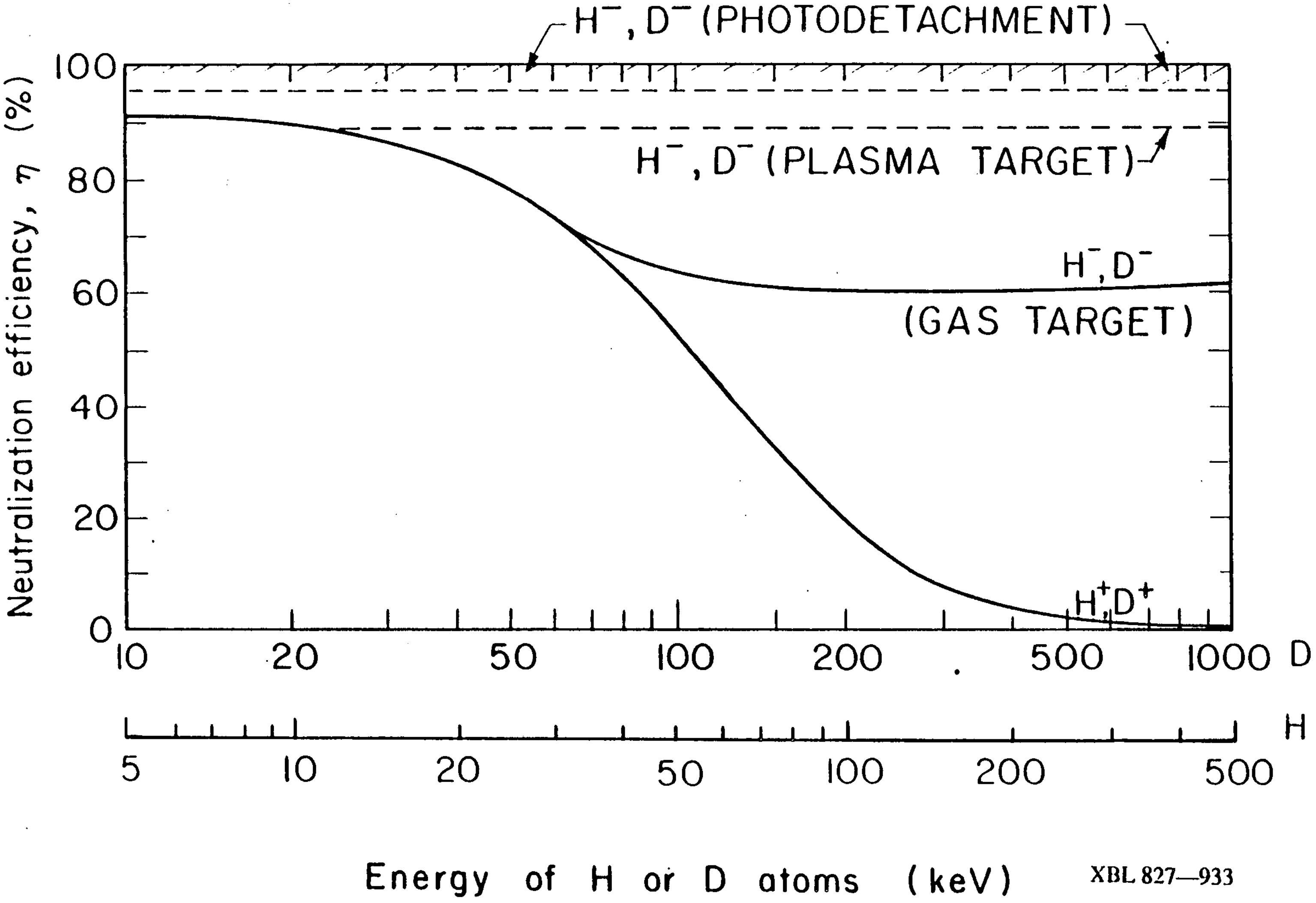

Fig. 1-2 Maximum Obtainable Neutral Fraction vs. Beam Energy

from the beam, both positive and negative. These high energy ions could cause damage to the entrance duct of the fusion plasma vacuum vessel. Another consideration is neutron shielding, since the neutral beam system has a direct line-of-sight to the fusion plasma, and next generation fusion devices will produce sizable amounts of 14 MeV neutrons from fusion reactions. However, the neutron flux is inversely proportional to the square of the distance from the reactor wall, therefore the use of long beamlines can substantially reduce neutron irradiation of some beamline components. This idea is incorporated in recent conceptual beamline designs (Fig. 1-3, from ref. 6).

Production of Negative Ions

There are presently three different methods for producing H^- ions: double charge exchange, surface production or conversion, and volume production. These also apply to Li^- and D^- ion production. In order to be useful for fusion applications, a negative ion source must achieve high delivered ion current densities with low emittance to the accelerator. The delivered current density should be of the order of tens of mA/cm^2 in order to achieve an economical heating and current drive system. Likewise, the requirement for low emittance dictated by the long beamlines makes a low negative ion energy spread very desirable. Ion source requirements for diagnostic beams vary widely depending on the application.

Double charge exchange negative ion sources utilize a positive ion beam that passes into a vapor cell where many ions

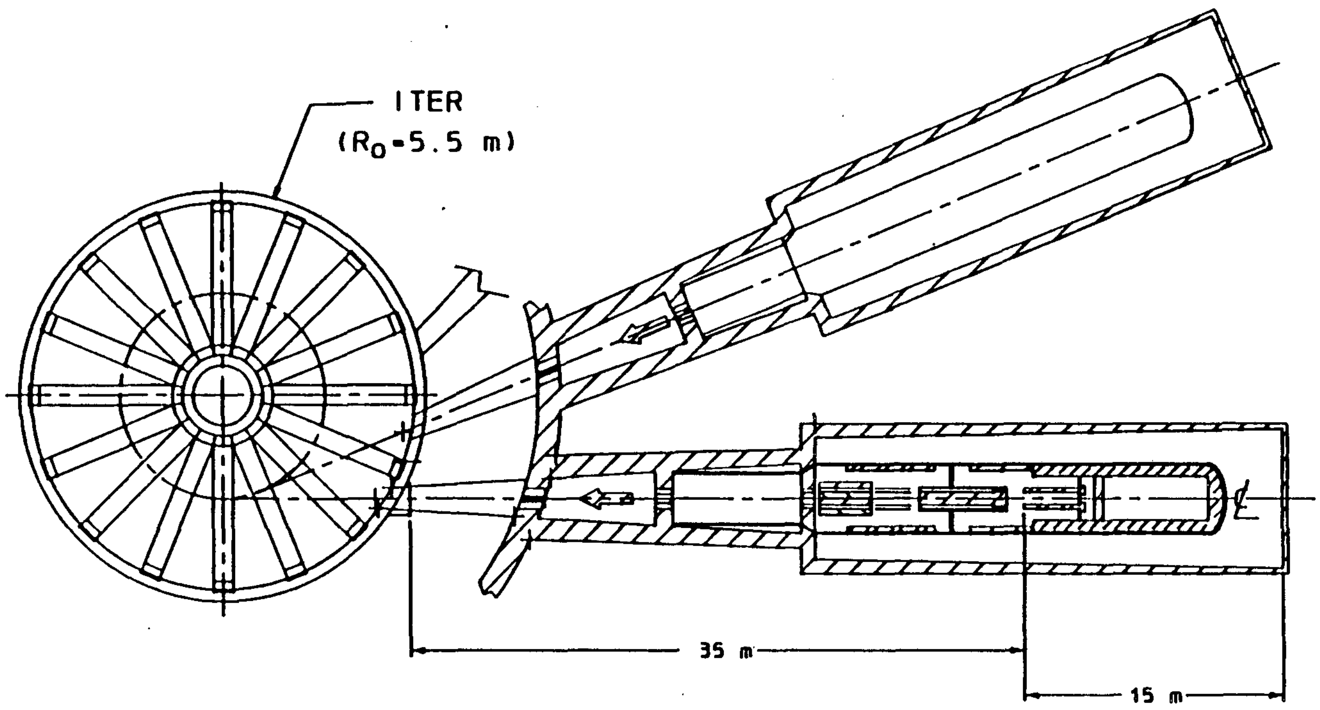

Fig. 1-3 Conceptual Beamline Design for ITER

XBL 891—258

undergo two electron capture reactions with vapor atoms to produce the negative ions (Fig. 1-4, from ref. 5).[10,11] The positive ion beam is typically at energies of 1 to 10 keV in order to optimize the charge capture cross section. The vapor is usually an alkali or alkaline earth metal. Efficiencies of approximately 10% are obtainable for a 10 keV proton beam in sodium, and 50% for a 250 eV proton beam in strontium.[12] This method of negative ion production suffers from several problems. Since the positive ion beam must have a relatively low energy, one must either tolerate the low current densities obtainable from positive ion sources at these energies or use an accel-decel system. Accel-decel systems are highly divergent due to space charge effects and therefore are generally unattractive. Moreover, the use of metal vapors as the charge exchange target can cause voltage holding problems in accelerator structures. Metal vapors are also difficult to confine to the source region and may appear as impurities in the fusion plasma. As a consequence of these problems, very little work is now being done on double charge exchange negative ion sources.

Surface production or conversion sources utilize a low work function surface immersed in a plasma to generate negative ions (Fig. 1-5, from ref. 5).[13,14,15,16] This low work function surface is usually made of molybdenum with a coating of cesium. A cesium coverage of about 0.5 monolayer results in a minimum in the work function.[17,18] This surface is biased negative with respect to the plasma in order to attract positive ions to the surface. These ions can interact with the surface in two ways to produce negative ions. As ions collide with the surface, they may pick up two electrons

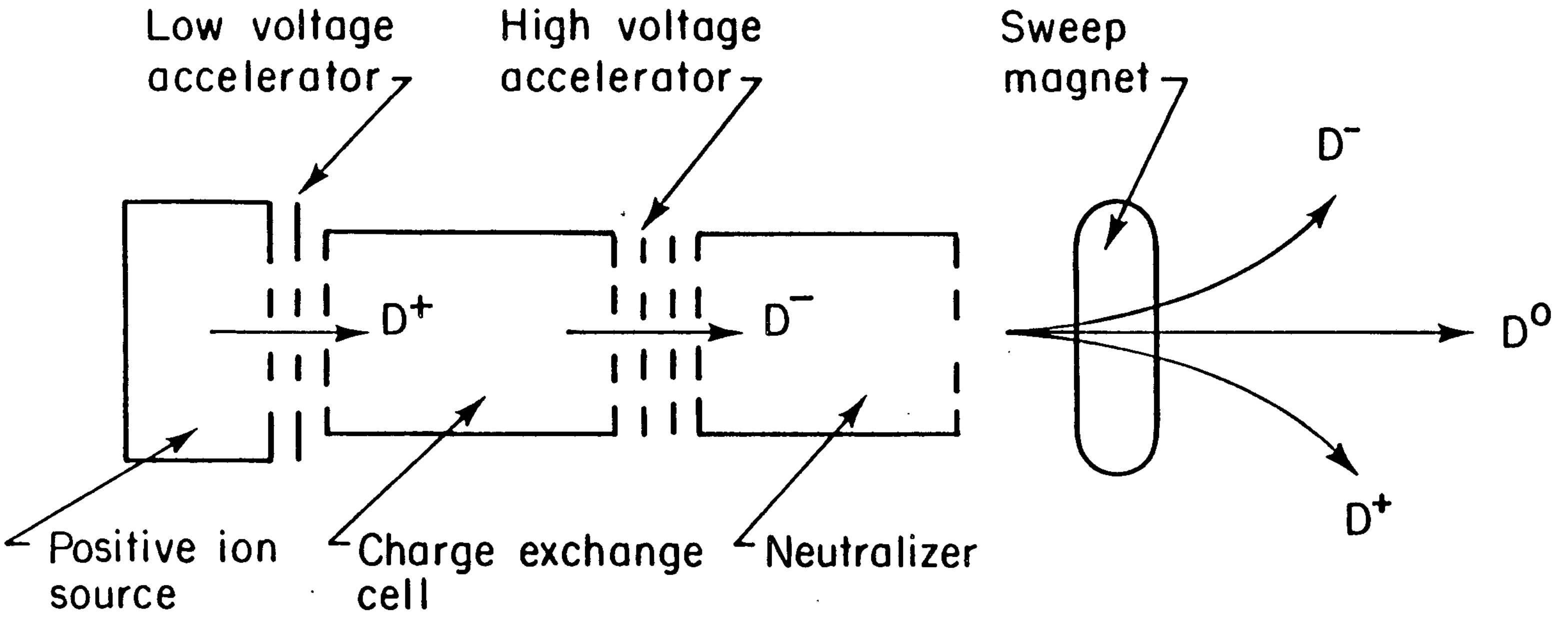

XBL 827 – 931

Fig. 1-4 Schematic Diagram of a Double Charge Exchange Neutral Beam System

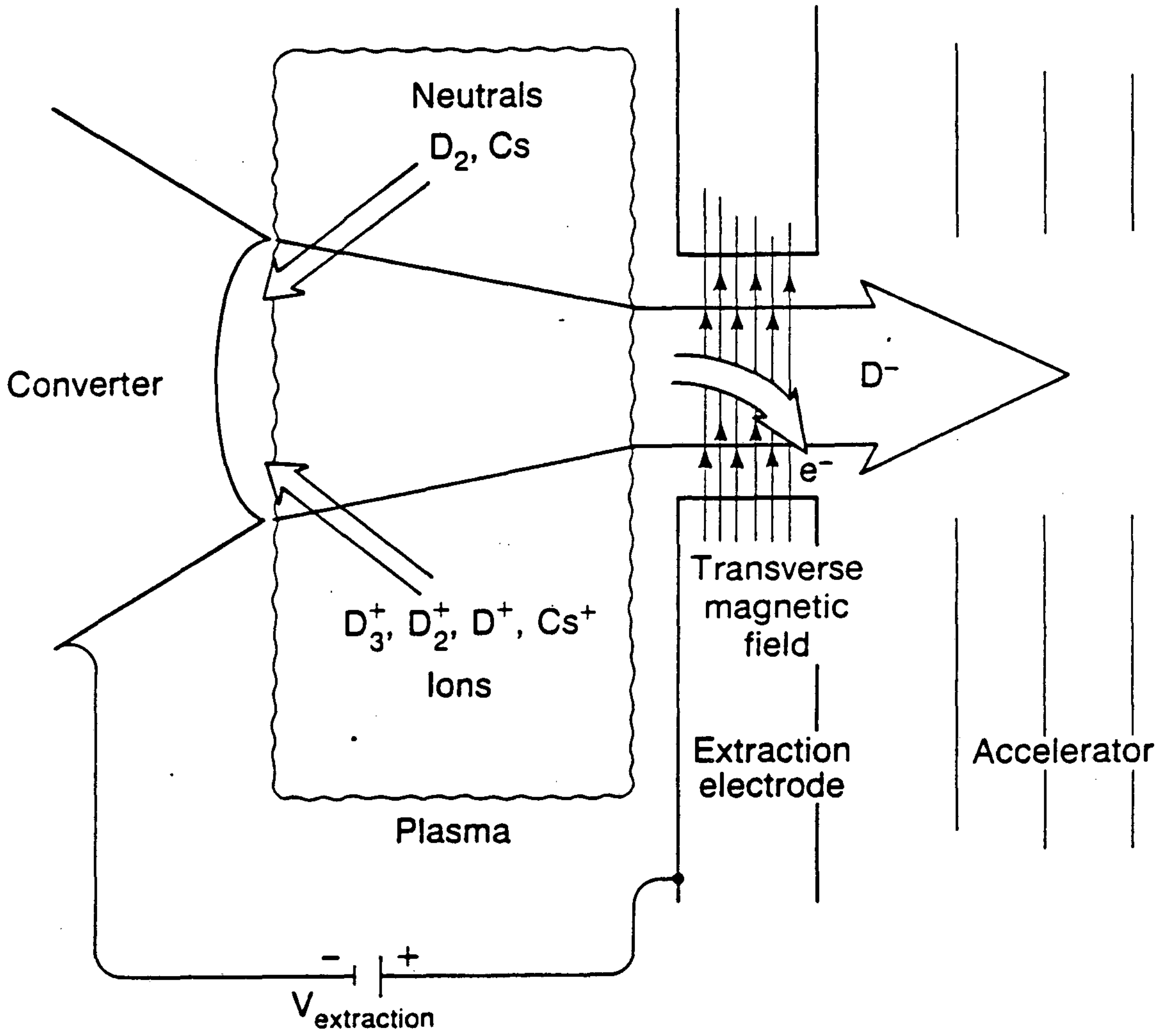

XBL 8411-6368

Fig. 1-5 Schematic Diagram of a Surface Converter Negative Ion Source and leave the surface negatively charged.[19,20] In this case, the positive ions are converted by the surface into negative ions which are further accelerated by the negative potential bias applied to the surface. Negative ions can also be formed by sputtering adsorbed gas atoms off of the low work function surface. These sputtered atoms can leave the surface with an additional electron to create a negative ion, which is accelerated into the plasma by the bias potential. Surface-conversion sources can produce large amounts of negative ions, of the order of amps per cm^2, on a pulsed basis (for H^-).[13] When operated in steady state, these sources produce a much smaller current density due to the difficulty of maintaining the cesiated surface under intense ion bombardment.[21] Problem areas for the surface source include the large energy spreads of the negative ions and the migration of cesium to accelerating structures causing electrical breakdowns. Some work continues on this type of negative ion source, however most of the research effort is now directed at volume production ion sources.

Volume production negative ion sources create negative ions through reactions in the volume of the plasma, although surface effects may be important here also. The relevant negative-ion-producing reactions are detailed in the literature.[22,23,24] Dissociative attachment is presumed to be the dominant mechanism for H^- ion production in most ion source plasmas, and has been shown to be the only known mechanism consistent with H^- ion production in low power discharges.[25] The dissociative attachment reaction proceeds as follows:

$$e_{slow}(< 1\ \mathrm{eV}) + H_2(v,J) \rightarrow H^- + H \ . \qquad (1\text{-}1)$$

Since almost all of the work presented here concerns low power discharges, the dissociative attachment reaction will be considered in some detail.

The cross section for dissociative attachment is a strong function of the internal energy of the molecule, and for hydrogen increases almost an order of magnitude for each vibrational state from 1 to 4, with smaller increases for higher states.[26,27] Thus it is important to populate the higher vibrational states in order to increase negative ion production. The most likely mechanism to populate these higher vibrational states is electron impact excitation of higher molecular electronic states which radiatively decay back to the ground electronic state.[28,29] This reaction proceeds as follows:

$$e + H_2 \rightarrow e + H_2^* \rightarrow e + H_2(v,J) + h\nu, \qquad (1\text{-}2)$$

and is detailed in Fig. 1-6 for several possible final states. After the radiative decay, the molecule can be left in a vibrationally and rotationally excited state.[28] Other mechanisms for populating the higher vibrational levels include wall neutralization of molecular ions[30] and recombinative desorption.[31,32]

The requirement for fast or primary electrons to populate high vibrational states is at odds with the high destruction cross section for negative ions interacting with fast electrons.[33] To increase the negative ion production efficiency, volume sources use

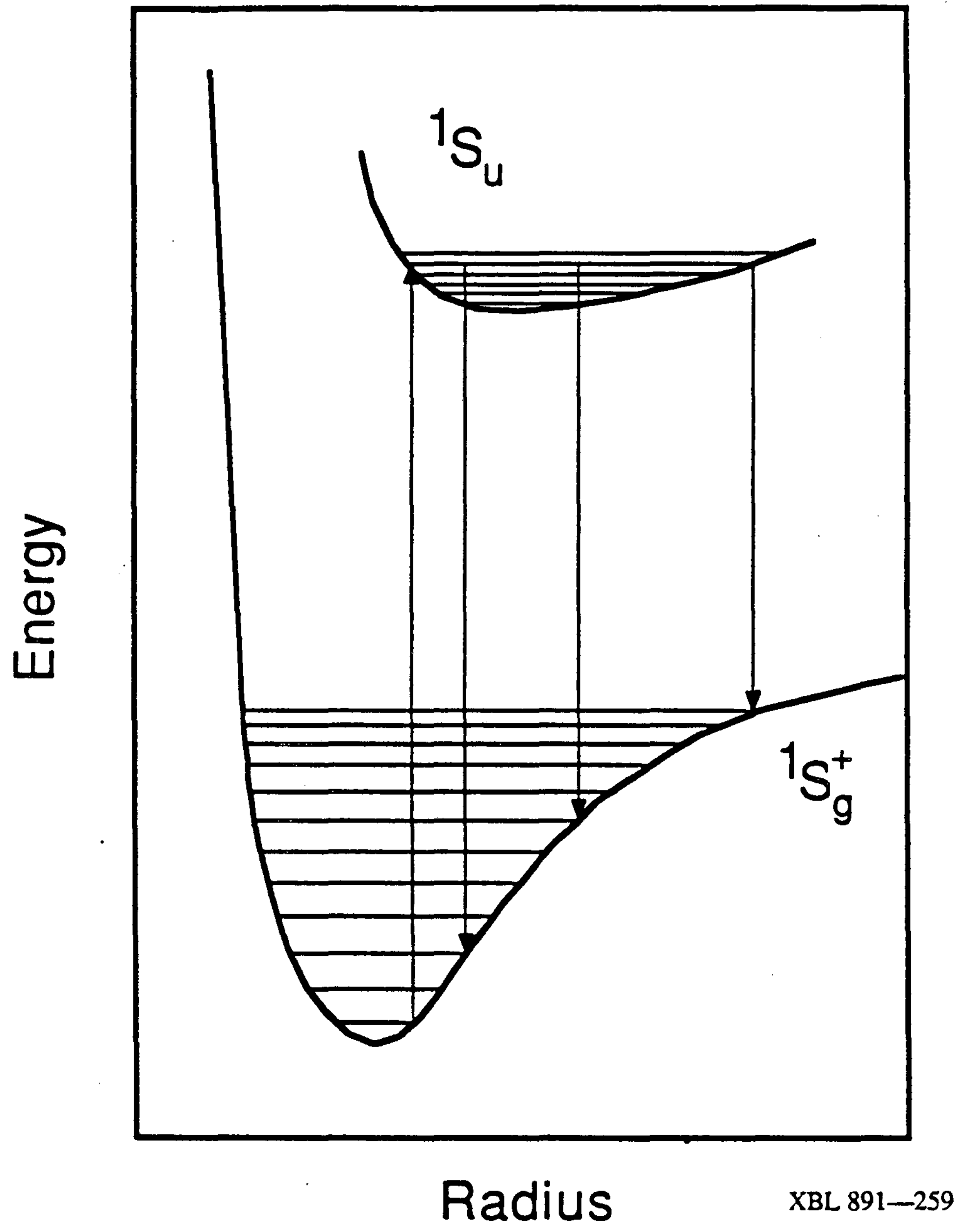

Fig. 1-6 Simplified Potential Energy Curve for Molecular Hydrogen Showing the Ground and Upper Electronic State

a two-region plasma. The first region, which contains the electron emitter, has a relatively high electron temperature and an energetic nonthermal component of electrons that is favorable for production of vibrationally excited molecules. The second region, where negative ion extraction takes place, has a low electron temperature ($T_e < 1$ eV) which is favorable for dissociative attachment. How this is achieved in practice is detailed in a later section.

Volume sources using the two region or tandem geometry (Fig. 1-7, from ref. 25) are being intensively developed in many laboratories, such as the Lawrence Berkeley Laboratory, Culham Laboratory (U.K.), and the Japan Atomic Energy Research Institute (JAERI). Improvements in achievable current density have made this negative ion source the most suitable for fusion applications. No cesium is required for ion source operation, and the ion energy spread from these sources is theoretically very low. A drawback is the large gas consumption of these sources, which can reduce negative ion output through stripping of the negative ions in the accelerator.

The Filtered Multicusp Ion Source

The filtered multicusp ion source creates a quiescent plasma[34] that is largely magnetic field free[35] (Fig. 1-8) and has two regions of differing electron temperature to maximize volume negative ion production.[22,23] Primary electrons are emitted from a hot tungsten or lanthanum hexaboride (LaB_6) cathode which is placed in a region of low magnetic field. These primary electrons

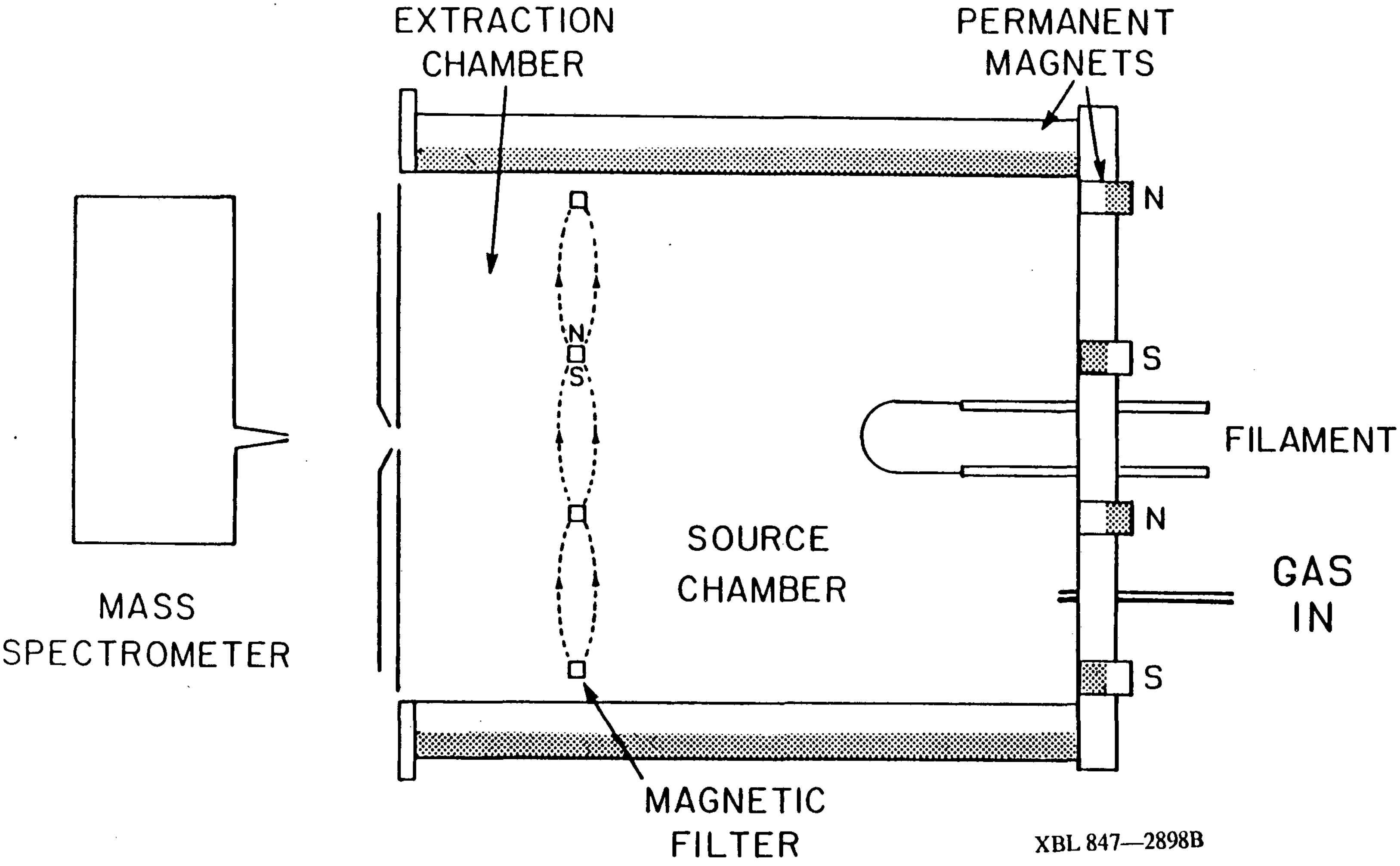

Fig. 1-7 Schematic Diagram of a Volume Negative Ion Source

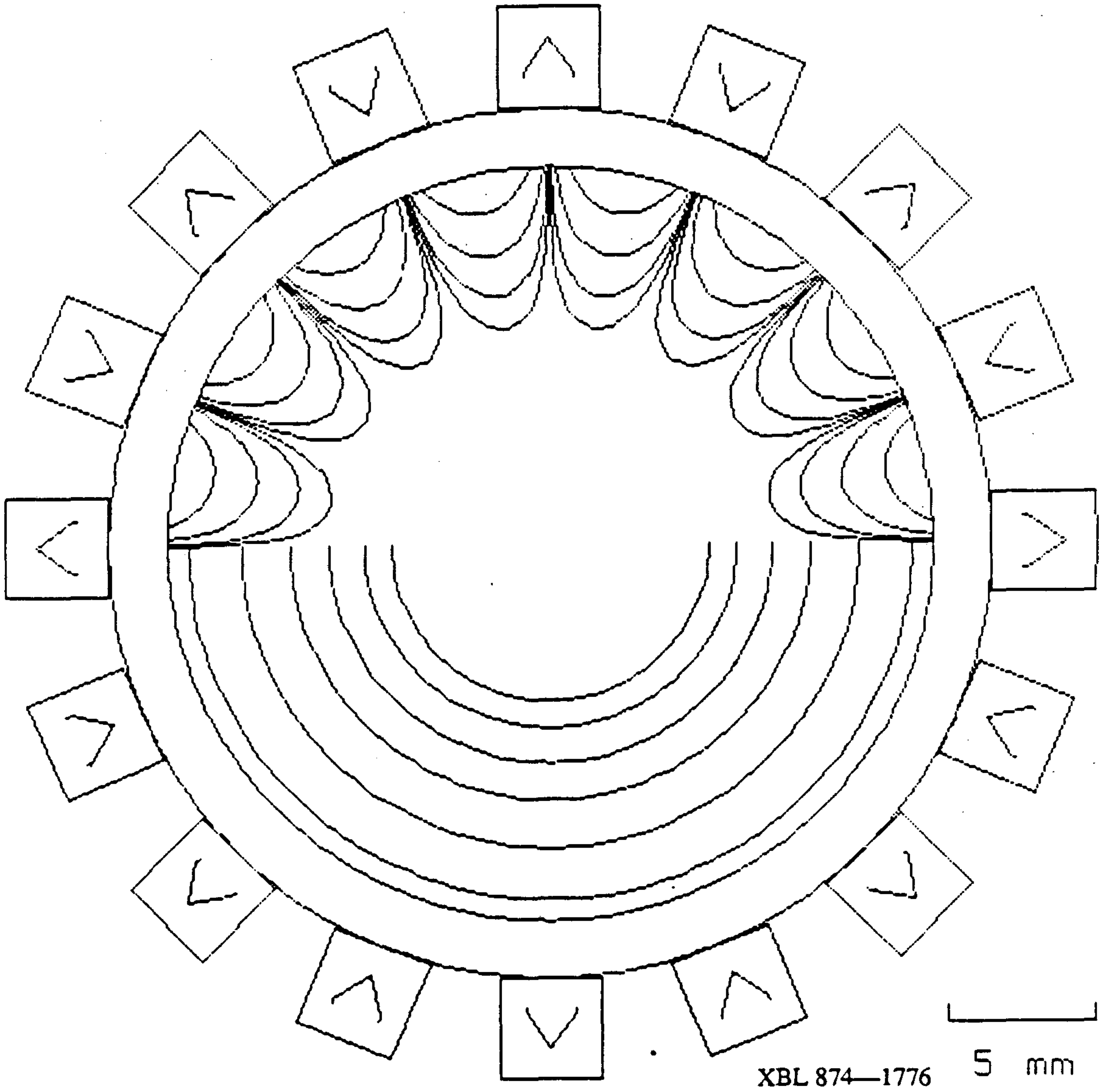

Fig. 1-8 A Computer Plot of the Magnetic Field Produced by the Multicusp Magnets Surrounding the Ion Source. The Upper Half Plot Shows the Field Lines (1, 3, 10, 30 gauss-cm), and the Lower Half Plot Shows the Field Intensity Contours (1, 3, 10, 30, 100, 300 Gauss).

gain energy in the cathode sheath and make ionizing collisions in the volume of the discharge. The multicusp magnets surrounding the ion source serve to reflect electrons back into the plasma thus randomizing the velocity distribution of the primary electrons and increasing the efficiency of the discharge. Losses are largely confined to the cusp lines where the electrons are subject to mirror like confinement. Thus, the multicusp configuration is well suited to generating large volumes of moderate density quiescent plasma.

In order to create the two-temperature or tandem discharge geometry, some way of excluding high energy or primary electrons from the low electron temperature region must be found. A simple but effective technique is to separate the high and low temperature regions with a localized transverse magnetic field strong enough to make the primary electron gyroradius small compared to the transverse width of the magnetic field. A strong transverse field makes the electron thermal conductivity across the field extremely small. This provides a form of insulation between the hot region, where the cathode is located, and the cold region where negative ions are extracted. Therefore, the filter is a mechanism for sustaining a two-temperature plasma, where the second region has an electron temperature of about 1 eV or less.[36]

The geometry of the filtered multicusp source is detailed in Fig. 1-7. As previously mentioned, the first region contains the cathode in a relatively magnetic-field-free region, while the entire ion source wall serves as anode for the discharge. The primary electrons emitted by the cathode are well confined in the first region, however, ions, low energy electrons, and neutrals including vibrationally excited molecules can diffuse into the second or extraction region. In the extraction region, the low electron temperature and the availability of vibrationally excited molecules from the first region contribute to substantially enhanced negative ion production over comparable single chamber systems.[22] In addition, the low electron temperature in the extraction region results in a lower plasma potential, which aids negative ion extraction.[37] The filter itself can be realized in a number of ways. One method is the use of filter rods in which permanent magnets are placed (as shown in Fig. 1-7). The plasma electrode is an electrically independent element which is usually biased very close to the anode potential. Biasing this surface affects electron and ion transport across the filter and as such is a useful tool in optimizing negative ion production.

Obviously there are a great number of design variables involved in developing the full potential of these ion sources. Much of the research in developing and optimizing the filtered multicusp source has been empirical. This is due to the difficulty in attempting to accurately model all of the processes relevant to negative ion production, especially when not all of the necessary atomic physics data are available. However, attempts to model the filtered multicusp geometry have rapidly improved over the past ten years. Most notable is the work of Hiskes,[22,23] who has provided theoretical estimates of attainable negative ion current density and optimal extraction chamber lengths for H^- ion sources.

Scope of This Thesis

This thesis presents both experimental and theoretical work concerning negative ion production and extraction from a filtered multicusp ion source. Chapter 2 details a theoretical model for production of Li^- and Li_2 in the multicusp geometry. Parameter scalings for both of these species are presented. In the case of Li_2 production, nonuniform lithium evaporation is shown to be the dominant production process. Chapter 3 provides experimental results for production of Li^-. These results are compared to the model of chapter 2 and show that there is substantial room for improvement in the Li^- current density produced by this source. An upgraded version of the Li^- ion source is proposed on the basis of this work. One possible use for this source is a magnetic pitch angle diagnostic for the International Thermonuclear Experimental Reactor (ITER), which is described in chapter 4. This proposed diagnostic uses a high energy Li° beam and is based on the Li^- ion source of chapter 3. Measurements of magnetic pitch angle, in situ and spatially resolved, could be achieved during a single pulse. Chapters 5 & 6 detail experiments on impurity seeding of hydrogen plasmas in order to improve the H^- current density that can be extracted from a multicusp source. Xenon, cesium, and barium are used as the impurities. In the case of cesium and barium, substantial evidence is presented for a new type of surface H^- production without the use of a converter. High power pulsed operation of a cesium-seeded hydrogen discharge is also detailed. A conclusion and summary of results is given in chapter 7. The future role of converterless surface production in negative ion sources is also discussed.

Chapter 2 Theory - The Lithium Ion Source Model

Introduction

High energy beams (> 500 keV) of lithium atoms are of interest for fusion plasma heating[38] and for plasma diagnostics. At present, the principal interest is for the diagnostic applications, which require much smaller beam currents than those needed for neutral beam heating. Diagnostic uses for lithium beams include in situ measurements of magnetic field, magnetic pitch angle, and current density in a tokamak. These measurements have already been demonstrated on the Texas EXperimental Tokamak (TEXT) with a positive ion based system at low energies (~100 keV).[39] It has also been proposed to use a neutral lithium beam to measure the velocity distribution of fast confined fusion alpha particles.[2]

A great deal of work, as noted in chapter 1, has been devoted to H^- (D^-) ion source development and relevant atomic processes. Due to the similarity of the H^- and Li^- systems, it is assumed that the relevant H^- atomic physics can be adapted to the Li^- system. An important difference is the ratio of atoms to molecules in the ion source. In a H^- ion source, H atoms are assumed to be a small but important fraction of the neutral species. In a Li^- ion source, it is the Li_2 molecules which are in the minority, because of the small binding energy of the Li_2 molecules (1.06 eV). The dimer molecules are important, since H^- and Li^- ions are believed to be formed predominantly by dissociative attachment:[22-25]

$$H_2(v^*) + e^- \rightarrow H + H^-, \tag{2-1}$$

$$Li_2(v^*) + e^- \rightarrow Li + Li^-, \tag{2-2}$$

where $X(v^*)$ denotes a vibrationally excited molecule. The lack of Li_2 molecules in equilibrium makes Li^- production difficult. Nonequilibrium situations, such as supersonic expansion through a nozzle, can be used to increase the dimer fraction in a Li^- ion source however.

To model the filtered multicusp ion source for the case of a lithium discharge, a rate equation approach similar to that of McGeoch and Schlier[40] will be taken. However, the dimer fraction will be inferred from experimental measurements, and modeled separately in a later section. The electron collisional detachment process will be included, and a two-chamber system modeled rather than a single discharge region. With these alterations, the Li^- ion density and extracted current will be modeled for various discharge conditions.

Lithium Ion Source Model - First Chamber

As in the case for a hydrogen discharge, the first chamber contains the filament and hence high energy electrons, which are necessary for ionization and vibrational excitation. Therefore this chamber also has a relatively high electron temperature (T_e). Production of $Li_2(v^*)$ is assumed to be predominantly via electron collisions.

$$Li_2 + e^- \rightarrow Li_2^* \rightarrow Li_2(v^*) + e^- + h\nu \ . \qquad (2\text{-}3)$$

Wadehra and Michels have analyzed this process and find that electron energies of $1.8 < \varepsilon < 2.5$ eV should be suitable for populating high vibrational states.[29] To model this process, 10% of the electron population in the first chamber are assumed to be in this energy range, an assumption also made by McGeoch and Schlier. With this, reaction (2-3) is calculated to proceed with a rate constant of $k_e = 1.2\text{x}10^{-8}$ cm^3s^{-1} for all electrons. Calculation of the rate constants is detailed in Appendix I.

$Li_2(v^*)$ is lost through wall collisions at a rate Ω, which is dependent on the ion source geometry, but for comparison with later experimental results it is calculated to have a value of $1\text{x}10^5$ s^{-1}. Wall collisions are assumed to completely de-excite $Li_2(v^*)$, since the sticking coefficient for lithium on surfaces is approximately unity by analogy with sodium[41], as was assumed by McGeoch and Schlier in ref. 43. De-excitation via atomic lithium collisions proceeds as:

$$Li_2(v^*) + Li \rightarrow Li_2 + Li, \qquad (2\text{-}4)$$

with a rate constant k_R of $5\text{x}10^{-10}$ cm^3s^{-1}.[42]

Li^- ions are created via dissociative attachment as illustrated in equation (2-2). This process has a 'rate constant' k_D of $2\text{x}10^{-8}$ cm^3s^{-1} for low energy electrons.[43] The fraction of electrons with low energy, suitable for dissociative attachment, in the first chamber is designated S_1. S_1 is calculated by integrating a maxwellian electron distribution, with temperature T_e, from zero energy up to a limiting energy where k_D becomes small by analogy to hydrogen.

Li^- ions are lost by mutual neutralization

$$Li^- + Li^+ \rightarrow 2Li, \tag{2-5}$$

and electron collisional detachment:

$$Li^- + e^- \rightarrow Li + 2e^- \ . \tag{2-6}$$

Mutual neutralization proceeds with a rate constant k_M of 1.5×10^{-7} cm^3s^{-1}.[44] Detachment proceeds with a 'rate constant' k_d of 2.7×10^{-6} cm^3s^{-1} for electrons with energies of 5 eV or greater.[45] The fraction of electrons with these energies in the first chamber is designated f_1. As in the case for vibrational excitation, f_1 is given an assumed value, since the confinement time of fast electrons is not well understood. Li^- ions are electrostatically confined by the positive plasma potential, and so are not lost via wall collisions. Li^- ions do, however, undergo charge exchange with atomic lithium:

$$Li^- + Li \rightarrow Li + Li^- \tag{2-7}$$

This process can act to cool the ions, and thus reduce their average speed. The cross section for this reaction is unknown at thermal energies, so the importance of reaction (2-7) cannot be evaluated. However, H^- ion beams are known to have random (or thermal) energies well above theoretical values when the equivalent reaction to (2-7) is significant for hydrogen. The negative ions created in the extraction region can gain random energy through several mechanisms, such as collisions with ions, locally varying plasma potentials due to the magnetic field of the filter, or poorly optimized extraction from the ion source. These higher H^- ion energies are similar to the energies of the positive hydrogen ions in the discharge. Thus, for simplicity it will be assumed that the Li^- ions have the same transverse energy as do Li^+ ions.

Using the rate constants for the above processes, rate equations for the $Li_2(v^*)$ and Li^- densities can be formulated. The neutral atomic and molecular lithium, $Li_2(v^*)$, electron, and Li^- densities are represented by n_1, n_2, n_2^*, n_e, and n^- respectively. For the vibrationally excited lithium molecules, a rate equation can be stated as,

$$dn_2^*/dt = k_e n_2 n_e - k_r n_2^* n_1 - k_D n_2^* n_e S_1 - \Omega n_2^*, \qquad (2\text{-}8)$$

while for negative lithium ions the equation becomes:

$$dn^-/dt = k_D n_2^* n_e S_1 - k_M n^-(n^- + n_e) - k_d n^- n_e f_1 \ . \qquad (2\text{-}9)$$

In equation 2-9 the positive ion density (n^+) is given by ($n^- + n_e$) through charge neutrality.

In steady-state operation, the time derivatives vanish and the equations can be solved for n_2^* in terms of n_1, n_2, n_e, and S_1; and for n^- in terms of n_e, n_2^*, f_1, and S_1. Solving for n_2^*, one arrives at:

$$n_2^* = (k_e n_2 n_e)/(k_r n_1 + k_D n_e S_1 + \Omega) \quad . \qquad (2\text{-}10)$$

For n^-, the following equation is obtained:

$$n^- = (n_e/2)\{[A^2 + 4k_D n_2^* S_1/(k_M n_e)]^{1/2} - A\}; \qquad (2\text{-}11)$$

where $A = (1 + k_d f_1/k_M)$. To calculate the extractable Li^- ion current density (J^-), the average velocity ($\underline{v}$) of the Li^- ions (calculated in Appendix 1) is used:

$$J^- = qn^-\underline{v}/4, \qquad (2\text{-}12)$$

where q is the electronic charge. These equations apply for a single chamber discharge.

Lithium Ion Source Model - Second or Extraction Chamber

The extraction chamber has a fundamental difference when compared to the first chamber, and that is the relative absence of energetic electrons. Measured electron temperatures in this region are quite low,[37] low enough to make rates of excitation, ionization, and detachment by electron impact negligible. In this chamber, the fast electron fraction is effectively zero. The rate equations for the second chamber are essentially the same as for the first chamber, with a few modifications. These include setting k_e and f_1 to zero (no energetic electrons), and allowing the plasma density and electron temperature to change from their first chamber values. This approach is similar to, but less sophisticated, than the model developed by Hiskes[22,23] for modeling H^- ion sources. Since there is no volume source term for $Li_2(v^*)$, the rate equation can be written as:

$$dn_2^*/dt = -k_r n_2^* n_1 - k_D n_2^* n_e S_2 - \Omega n_2^*, \qquad (2\text{-}13)$$

where S_2 is the fraction of the electron population with energies low enough for dissociative attachment. This results in an exponentially decaying n_2^* population. Let v_2^* be the average velocity of the excited molecules. By dividing both sides of equation (2-13) by v_2^*, an axial (z) dependence of n_2^* can be determined.

$$(1/v_2^*)(dn_2^*/dt) = (dt/dz)(dn_2^*/dt) = dn_2^*/dz \quad . \qquad (2\text{-}14)$$

$$dn_2^*/dz = -n_2^*(k_r n_1 + k_D n_e S_2 + \Omega)/v_2^* \quad . \qquad (2\text{-}15)$$

$$n_2^*(z) = n_2^*(0) \ \exp[-(k_r n_1 + k_D n_e S_2 + \Omega)(z/v_2^*)] \quad . \qquad (2\text{-}16)$$

In equation (2-16), z=0 represents the plane of the magnetic filter, and $n_2^*(0)$ is the bulk density at the edge of the filter in the first chamber. This is an approximation, since one does not expect a spatially uniform density of $Li_2(v^*)$ in the first chamber. For a given extraction chamber length, an average value of n_2^* can be calculated. This is given by:

$$<n_2^*> = n_2^*(0)\ (1/\Sigma z_{max})(1 - \exp(-\Sigma z_{max})), \qquad (2\text{-}17)$$

where Σ is $(k_r n_1 + k_D n_e S_2 + \Omega)/v_2^*$, and z_{max} is the length of the extraction region of the ion source. The negative ion density can now be solved to obtain:

$$n^- = (n_e/2)\{[1 + 4k_D<n_2^*>S_2/(k_M n_e)]^{1/2} - 1\}, \qquad (2\text{-}18)$$

where n_e is the electron density in the extraction region. These equations may now be used to calculate the extractable negative ion current from a discharge under a variety of conditions. The required input data are the atomic and molecular neutral densities and temperatures, plasma density in both regions, and electron temperature in both regions. In the next section, the single and tandem discharge systems will be compared and the effect of various discharge parameters on Li^- output will be explored.

Results for the Lithium Ion Source Model

The equations of the previous section were solved to yield extracted current densities for both the single and two chamber (tandem) systems. As noted above, plasma density and T_e for both chambers must be known in order to evaluate the equations. It has been observed experimentally that the plasma density in the extraction chamber is approximately a factor of five lower than in the first chamber for an ion source with a strong magnetic filter.[46] Therefore, only one plasma density needs to be specified. A first chamber electron density of 10^{12} cm^{-3} is assumed for most of the calculations. The measured electron temperatures of a low power filtered multicusp ion source, 1.4 eV in the first chamber and 0.35 eV in the second chamber, operating with hydrogen, are used as representative values.[37]

Other data needed to complete the solution are the neutral atomic lithium density (taken as 10^{15} cm^{-3} here), the percentage of lithium molecules in the neutral population (taken as 10% and further detailed in a later section), the wall temperature (taken from experimental data as 700°K and used for neutral velocity calculations), and the extraction chamber length (taken as 4 mm and used in experiments). With a complete set of data, the scaling of Li^- current density with various parameters can be evaluated. This information provides clues to optimizing the Li^- output from the source.

One of the most important parameters to ion source operation is the electron density in the source, since it roughly scales with the discharge power. In order to achieve the necessary current densities for fusion applications, ion sources will be scaled up in power density, with hopefully corresponding increases in negative ion density. Therefore, it is important to evaluate the scaling of current density with the electron density. Fig. 2-1 is a graph of the Li^- current density as a function of the electron density in the first chamber (n_{e1}). The second chamber electron density (n_{e2}) is,

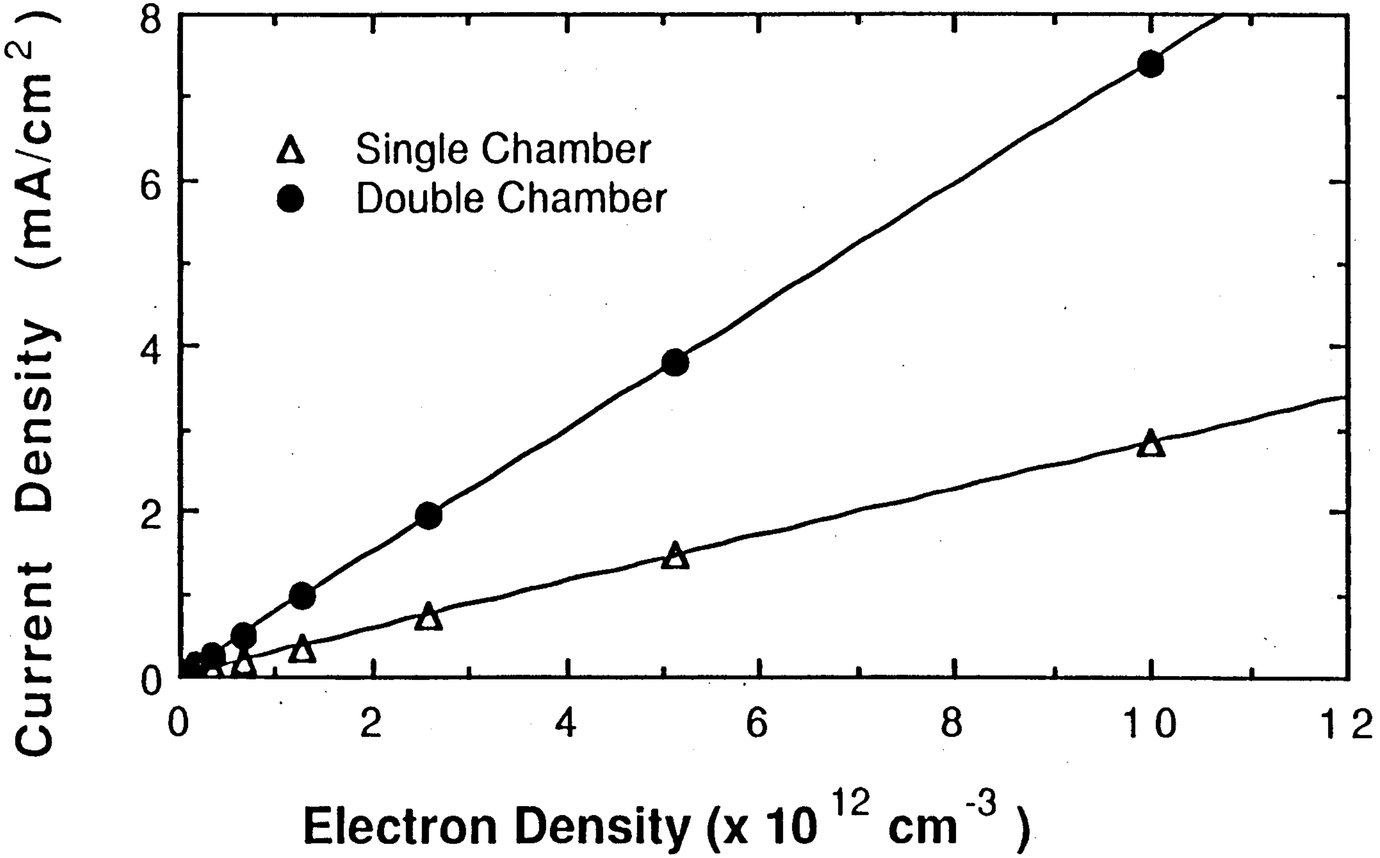

XBL 891—260

Fig. 2-1 A Plot of Li^- Current Density vs. First Chamber Electron Density as previously mentioned, taken to be $n_{e1}/5$. Over the range of densities plotted, the Li^- current density for both single and two chamber systems scales directly with electron density. Only when the negative ion loss terms, such as mutual neutralization, become comparable to the dissociative attachment term, will the scaling saturate. Saturation is hinted at in Fig. 2-1 by a very slight droop in the current density plot at the highest electron densities. That is due to the onset of mutual neutralization, and will ultimately cause the current density to saturate, but at extreme electron densities. The plasma density scaling seems very favorable. However it should be noted that high density plasmas tend to also have high rates of dissociation, which could reduce the molecular fraction, assumed constant at 10%.

The fraction of Li_2 in the neutral population is expected to be the most critical parameter in the lithium ion source. In equilibrium, the fraction of Li_2 in lithium vapor is very small (typically one percent or less). In nonequilibrium evaporation or supersonic expansion, the percentage of molecules can be very high (greater than ten percent).[47] Fig. 2-2 is a plot of the Li^- current density as a function of the molecular fraction. As expected, the current density for both the single and two chamber systems increases with the percentage of Li_2 in the ion source. The single chamber system exhibits a linear relationship with the molecular percentage, while the two chamber system encounters a slight saturation effect as higher percentages are reached. However, these higher percentages are unlikely to be achieved in a steady-state system.

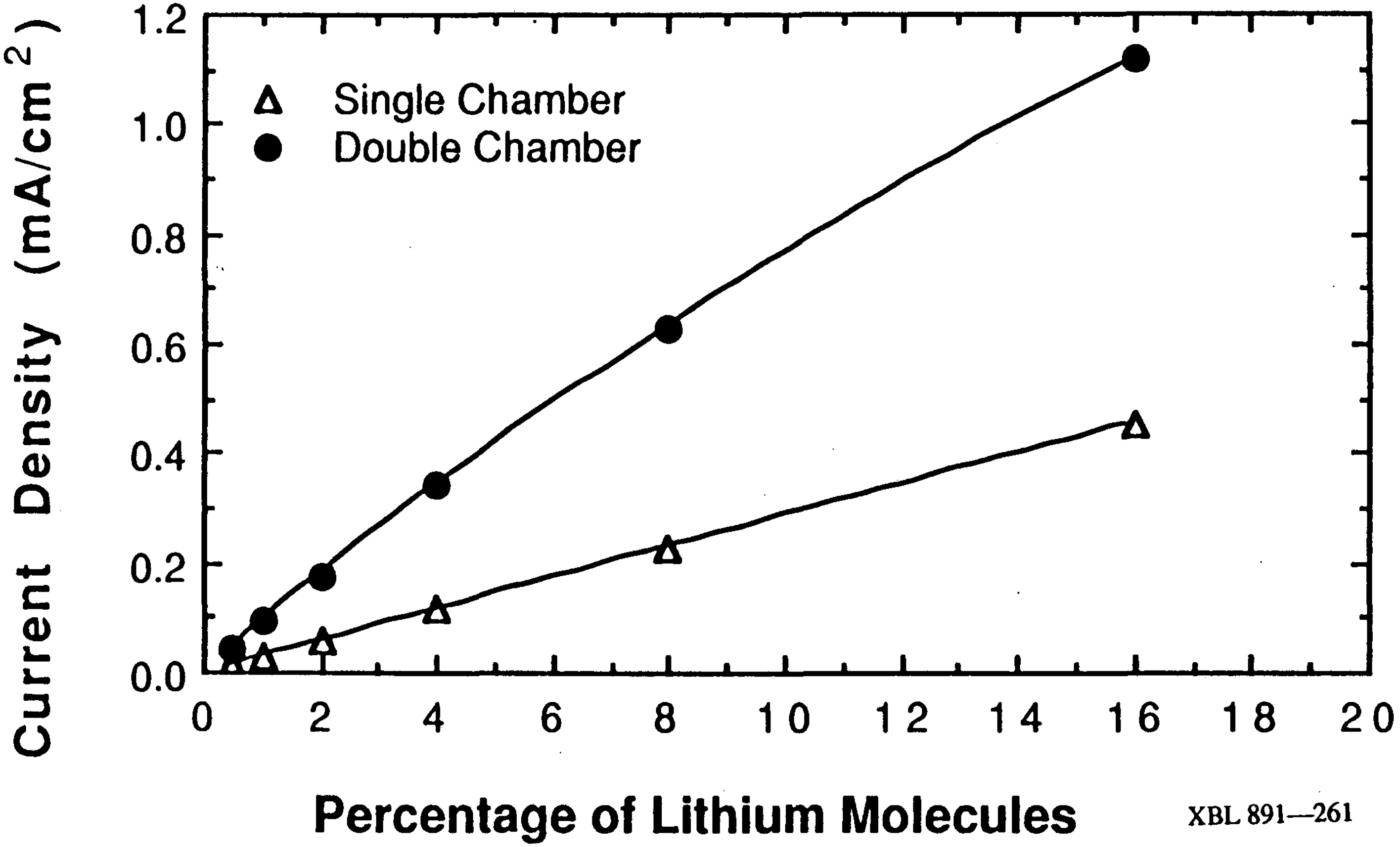

XBL 891—261

Fig. 2-2 A Plot of Li^- Current Density vs. the Percentage of Lithium Molecules Present in the Discharge

An experimental variable that is relatively easy to control is the gas density in the source. Low gas densities are preferred, in order to reduce stripping of the negative ions outside of the source and in the accelerator. Unfortunately, best results in terms of current density are usually obtained with high gas densities in the ion source. The extracted current density as a function of the atomic lithium density is plotted in Fig. 2-3. The behavior of the single and two chamber systems are distinctly different as the density is increased. The single chamber system current density initially increases rapidly until saturation sets in at about 5×10^{14} cm^{-3}. Saturation is due to the de-excitation of the molecules by collisions with atoms. Likewise, the two chamber system output decreases quickly after peaking at about 5×10^{14} cm^{-3}. Since the electron density is lower in the second chamber, the atomic de-excitation rate rapidly eclipses the dissociative attachment rate as the neutral density is increased. This effect is amplified in the two chamber system due to the exponential decay of the excited molecule population with distance from the filter.

To emphasize that last point, the current density as a function of the extraction chamber length is plotted in Fig. 2-4. The current density decays roughly exponentially due to the exponential decrease in $Li_2(v^*)$ with distance from the midplane of the magnetic filter. This plot would imply that the optimal extraction chamber length should be zero. In practical terms, the effect of the fringing magnetic filter field on negative ion extraction limits how short this length can be.

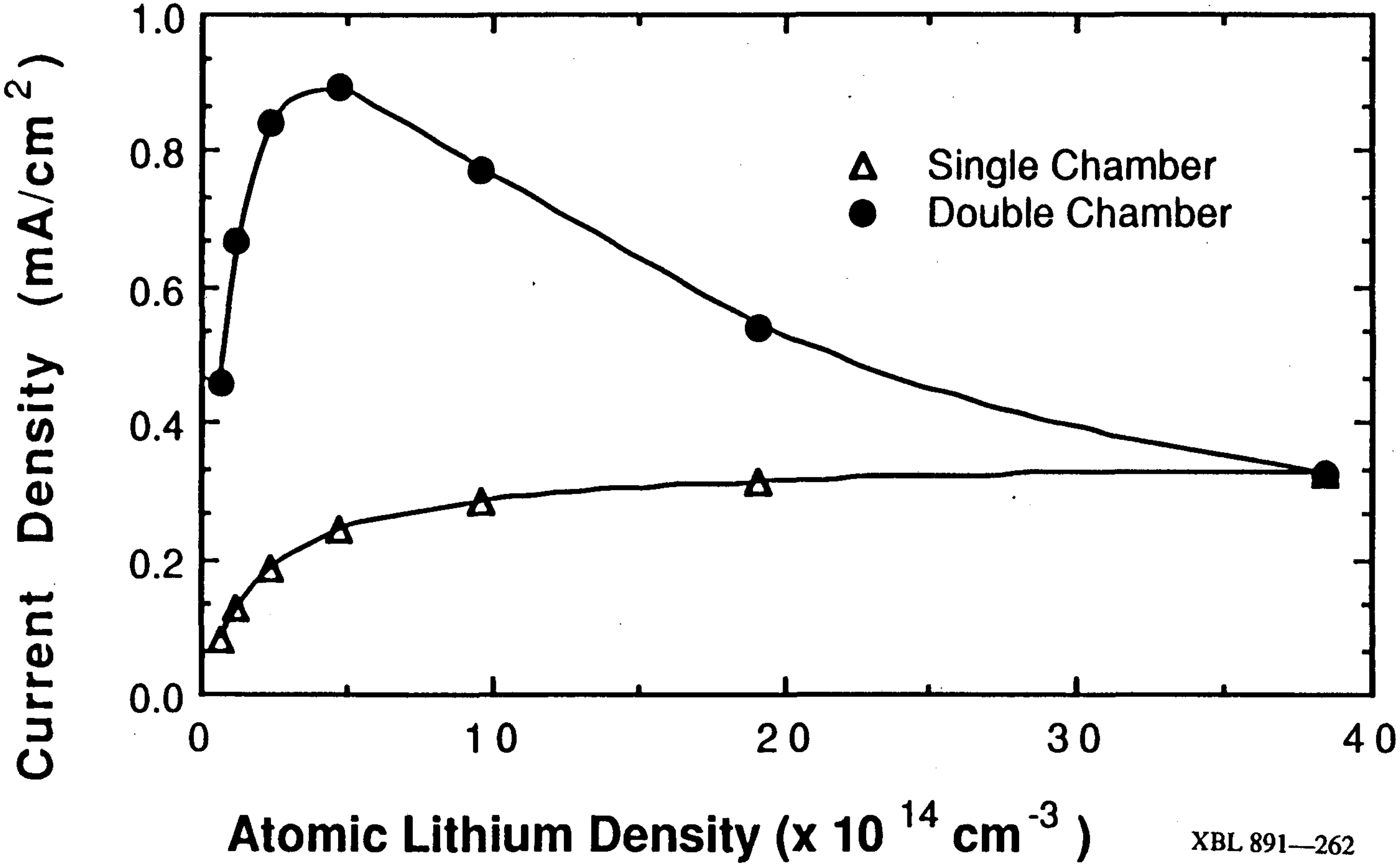

Fig. 2-3 A Plot of Li^- Current Density vs. Atomic Neutral Density for Both Double and Single Chamber Discharge Configurations

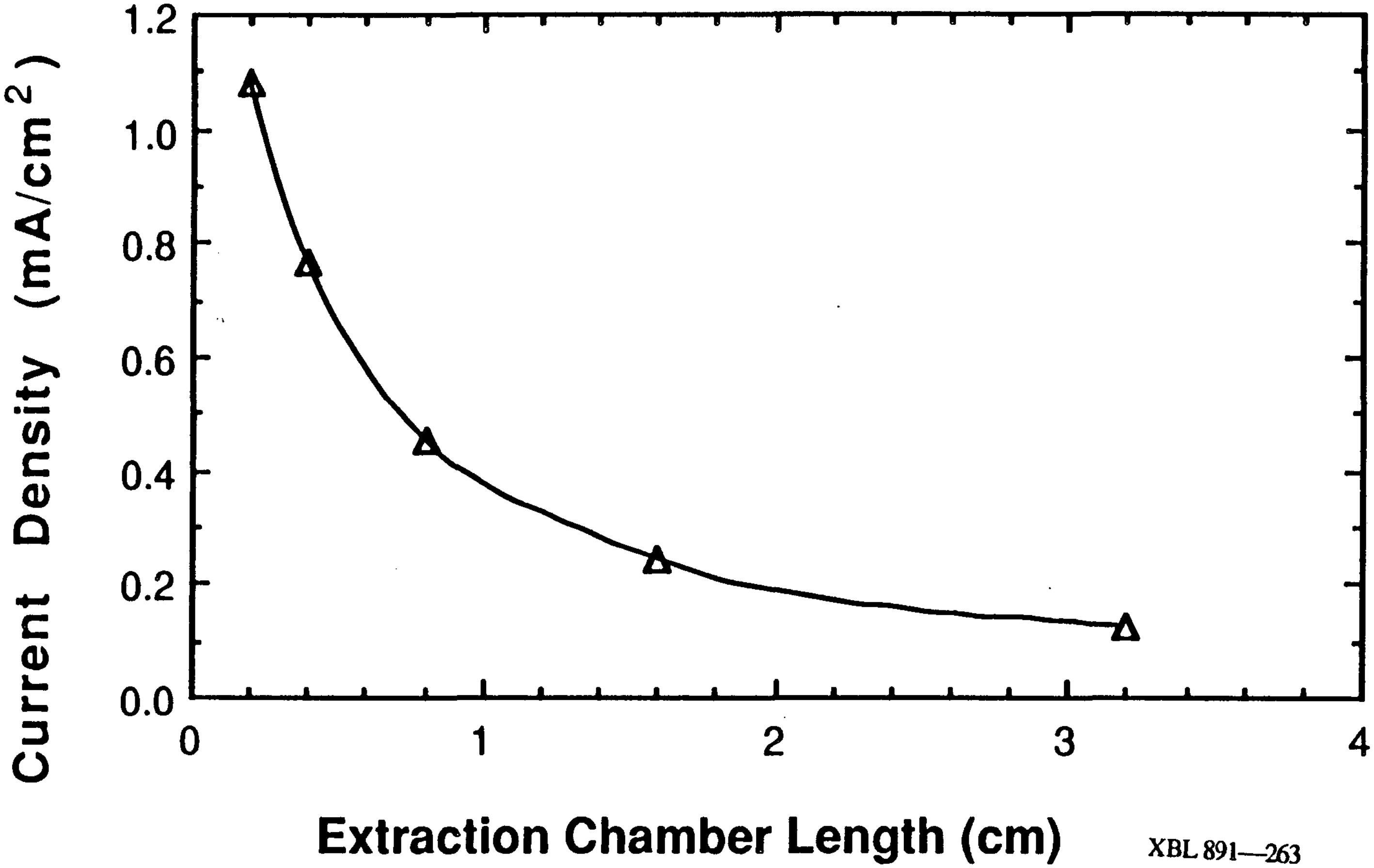

XBL 891—263

Fig. 2-4 A Plot of Li$^-$ Current Density vs. the Length of the Extraction Chamber

The second chamber electron temperature is also an important parameter for negative ion production in the two chamber system. Although the measured T_e is very low for strongly filtered systems (0.35 eV), Fig. 2-5 shows that further decreases in T_e could provide substantial increases in Li^- current density. The increase is due to the peaking of the dissociative attachment cross section for very low energy electrons. If T_e is allowed to increase, a steady drop in current density results. The first chamber electron temperature only affects the two chamber system output by changing the negative ion temperature in the second chamber. However, the single chamber system current density will decrease substantially for higher T_e, due to fewer electrons of the proper energy for dissociative attachment, and increased electron collisional detachment of Li^-.

These results show the advantage of the two chamber system versus a single chamber discharge. Higher current densities are obtained by the tandem system because there is no loss of Li^- by electron collisional detachment. As expected, the electron density, molecular fraction, and second chamber electron temperature are extremely important parameters. Both the electron density and molecular fraction should be increased as much as possible. The second chamber T_e should be minimized, which can be accomplished with a stronger filter, but at a cost of some electron density in the second chamber. The use of a tandem discharge configuration also allows a lower optimum pressure than a single chamber discharge, which becomes important when stripping of the negative ion beam outside of the source is considered.

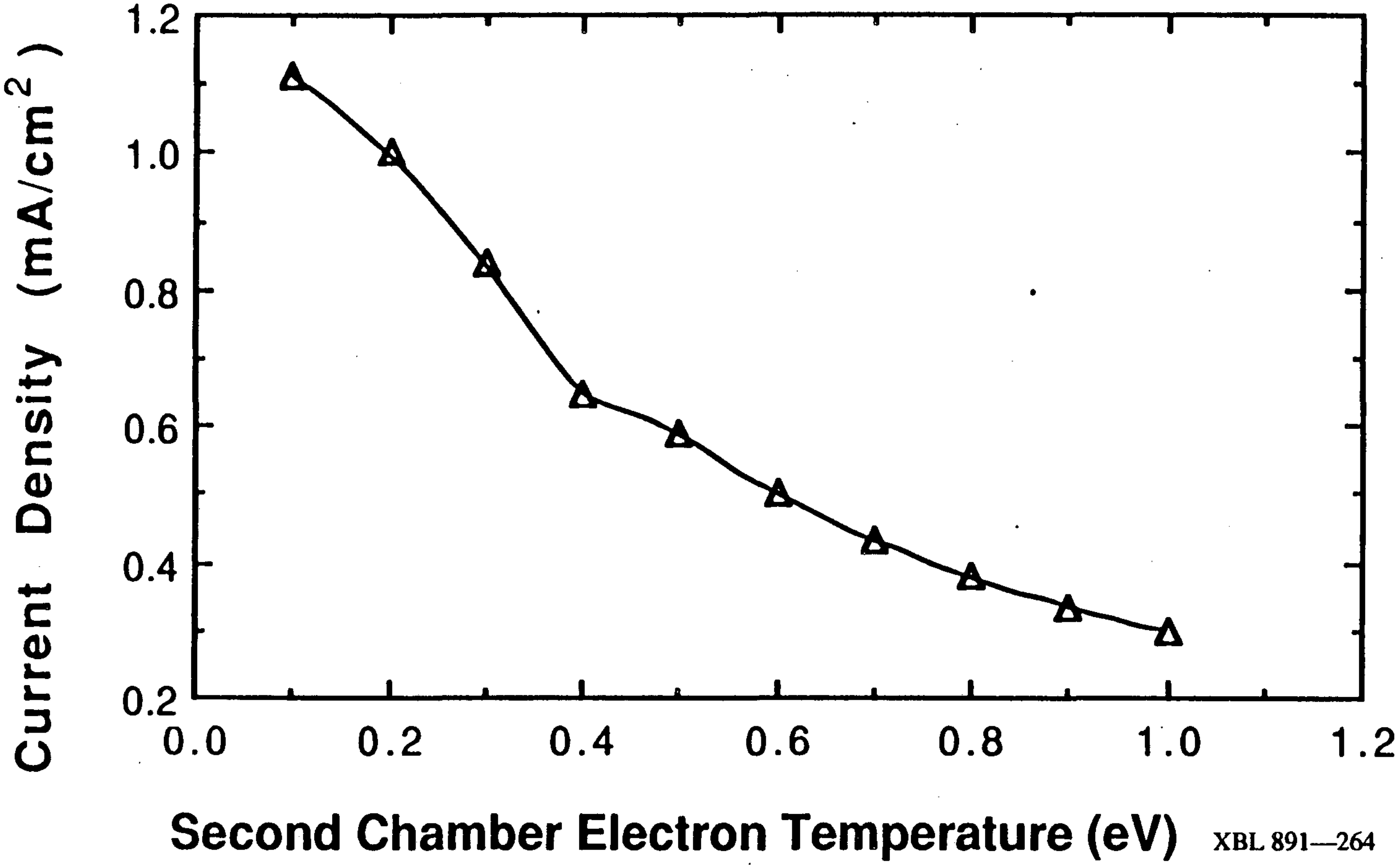

XBL 891—264

Fig. 2-5 A Plot of Li$^-$ Current Density vs. Second Chamber Electron Temperature

In addition to negative ion current density, the number of electrons extracted from the ion source is of considerable importance. These electrons increase the requirements on extraction and acceleration power supplies, cause stripping of the beam, add to space charge in the beam, create additional heat loading on the extraction and acceleration electrodes, and can increase voltage breakdown problems in high voltage structures. Therefore, the extracted electron current should be reduced as much as possible. The tandem geometry provides a large improvement over the single chamber system in this respect as well. Not only is the electron density in the extraction region substantially reduced, but the T_e of these electrons is also much lower. This results in about an order of magnitude reduction in the extracted electron current density for the tandem configuration.

Useful Li^- current densities appear achievable with the tandem discharge geometry. In contrast to the result given by McGeoch and Schlier of 0.026 mA/cm^2 for a single chamber discharge (with low molecular fraction), current densities of several mA/cm^2 can be produced in the optimized two chamber ion source. The most critical factor in these calculations has been the assumption of a relatively high molecular fraction ~10%, which was inferred from experimental observations.[48] The following section will model the Li_2 surface formation process in order to determine how molecules are predominantly formed and whether the 10% figure can be explained and possibly improved.

Model for Dimer (Li_2) Formation in the Ion Source

Previous results show the importance of achieving a high dimer fraction of the neutral species in the ion source. For lithium vapor in thermal equilibrium, dimer fractions are limited to less than two percent for vapor pressures of interest.[49] The dimer fraction increases with evaporation rate, i. e. the liquid surface temperature, but a practical limit is reached when Li^- ion stripping by neutral particle collisions becomes significant. Source pressures greater than 0.1 Torr are thus not feasible. Increasing the dimer fraction will therefore require a nonequilibrium approach to dimer formation.

There are several methods to create high dimer fractions in alkali metal vapors. One of the most well known is to use a high temperature oven to produce a vapor at high pressure which is expanded through a supersonic nozzle, the approach advocated by McGeoch and Schlier.[40] The drawback to this method is that the lithium vapor makes only one pass through the ion source before it must be collected and piped back to the oven. This makes for a complicated arrangement, particularly if the source is to operate steady state for long periods of time. An alternative method, which does not require the use of an external oven, is to allow lithium evaporation from a very restricted area of the wall of the ion source.

If the temperature of the ion source wall is allowed to vary significantly with position, the local evaporation rate will also vary strongly with position. Thus, the effective area for lithium evaporation can be greatly reduced by making most of the ion source wall relatively cold ($T_{wall} < 750°K$). The local rate of evaporation of the hotter regions of the wall must be increased to compensate, since all surfaces contribute to lithium condensation. A high local evaporation rate is conducive to higher rates of dimer formation. The picture of the source now is one where most of the wall is cold and acts as a sink for lithium vapor. The lithium condensate moves to a hotter region where it evaporates under conditions favorable for dimer formation.

There are two mechanisms to passively transport the lithium condensate to the hot region. One is to use gravity to move a thin ($< 10^{-4}$ m) film of condensate to the bottom of the ion source where a hot region is located. The second is to use the natural tendency of lithium adsorbates (submonolayer) to spread out in order to minimize surface concentration.[50] However, this second approach is unlikely to be feasible since the colder walls of the ion source will undoubtedly have a multiple monolayer (ML) lithium coverage due to the high rate of condensation. Hence, transport via gravity of a thin film of lithium condensate is the mechanism assumed here.

To model this situation, a small fraction (β) of the ion source wall area will be assumed hot and the rest relatively cold. The cold region has a negligibly small evaporation rate, but lithium condenses on these surfaces and is transported to the hot region. The hot region is where the vast majority of lithium is vaporized due to higher temperatures. Since the sticking coefficient of lithium is approximately unity, any lithium atom or molecule which collides with a wall surface is removed from the vapor phase. Steady state operation requires that the rate of condensation on all wall surfaces be balanced by evaporation from the hot region. This section develops rate equations for these processes with the goal of finding a practical way of significantly enhancing the dimer fraction in the ion source.

To determine the condensation rate, the neutral species will be assumed to have a maxwellian velocity distribution at a gas temperature equal to the temperature of the hot wall surface, while the gas density is left as a free variable to be given later. The gas temperature may be modified by evaporative cooling, collisions with the hot filament surface, and collisions with the plasma electrons and ions. However, the use of the hot wall temperature seems both reasonable and convenient, since wall collisions are dominant compared to any other dimer collision process. The rate of condensation can then be given as:

$$R_{con} = (n_1 v_1 + 2n_2 v_2)A/4, \qquad (2\text{-}19)$$

where v_1 is the average velocity of the lithium atoms, v_2 the average velocity of the dimers, and A is the wall area of the ion source.

The rate of atomic desorption is given by:[51]

$$R_{de1} = K_1 m, \qquad (2\text{-}20)$$

where K_1 is a rate constant and m is the surface concentration of lithium atoms. K_1 is approximately given by:

$$K_1 \approx (2\pi kT/h)\exp(-E_a/kT), \qquad (2\text{-}21)$$

where k is Boltzmann's constant, h is Planck's constant, and E_a is the adsorption energy of a lithium atom on the wall surface. The molecular desorption rate (in atoms) is given by:[51]

$$R_{de2} = K_2 m^2, \qquad (2\text{-}22)$$

where K_2 is given by :

$$K_2 \approx S_2(2\pi kT/h)^2(\pi MkT)^{1/2}(p_2/p_1^2)\exp(-2E_a/kT), \qquad (2\text{-}23)$$

where S_2 is the molecular sticking coefficient (also unity), M is the atomic mass of lithium, and p_1 and p_2 are the equilibrium partial pressures of the atomic and molecular vapor respectively.

In order to evaluate these expressions, values for E_a, p_1, p_2, and m are required. E_a is a function of m in the low coverage limit and has been measured for lithium on tungsten,[52] since no other similar data are available, a tungsten wall surface will be modeled in all calculations. Values of p_1 and p_2 have been tabulated as a function of temperature.[49] Given this information, the atomic and molecular desorption rates can be calculated. The dimer fraction of the ion source will be evaluated as a function of the temperature of the hot wall surface, its fractional area (ß), and the neutral density in the ion source. The surface coverage is iterated until the rates of adsorption (condensation) and desorption (evaporation) are equal.

Fig. 2-6 is a graph of the adsorption energy (E_a) of lithium on a (110) tungsten surface as a function of lithium coverage (from Ref. 52). This dependence of E_a on surface coverage is extremely important. At coverages of about one ML, the adsorption energy is significantly lower than the energy required for evaporation from a pure lithium surface (~1.61 eV).[49] Since dimer desorption is very sensitive to this energy, a lithium on tungsten surface can provide a substantial enhancement in dimer production over a pure lithium substrate. In order to calculate results at high coverages, E_a is assumed to be at a minimum at 1.2 ML. Although there is no data for coverages above 1.2 ML, it is reasonable to assume a minimum somewhere at or above 1.2 ML, since this approaches the pure lithium case which has a higher E_a of ~1.6 eV.

The (110) surface of tungsten was used in these calculations since it had the lowest adsorption energy measured. A polycrystalline surface is the most common experimentally, and will have a variety of crystal planes exposed. However, the use of the (110) surface is justifiable because the surface with the lowest E_a will have the largest evaporation rate and hence the most influence on desorption characteristics. The important variable to be minimized though, is (E_a/kT), as can be seen in equation (2-23). So, the adsorption energy must be minimized at the maximum possible temperature.

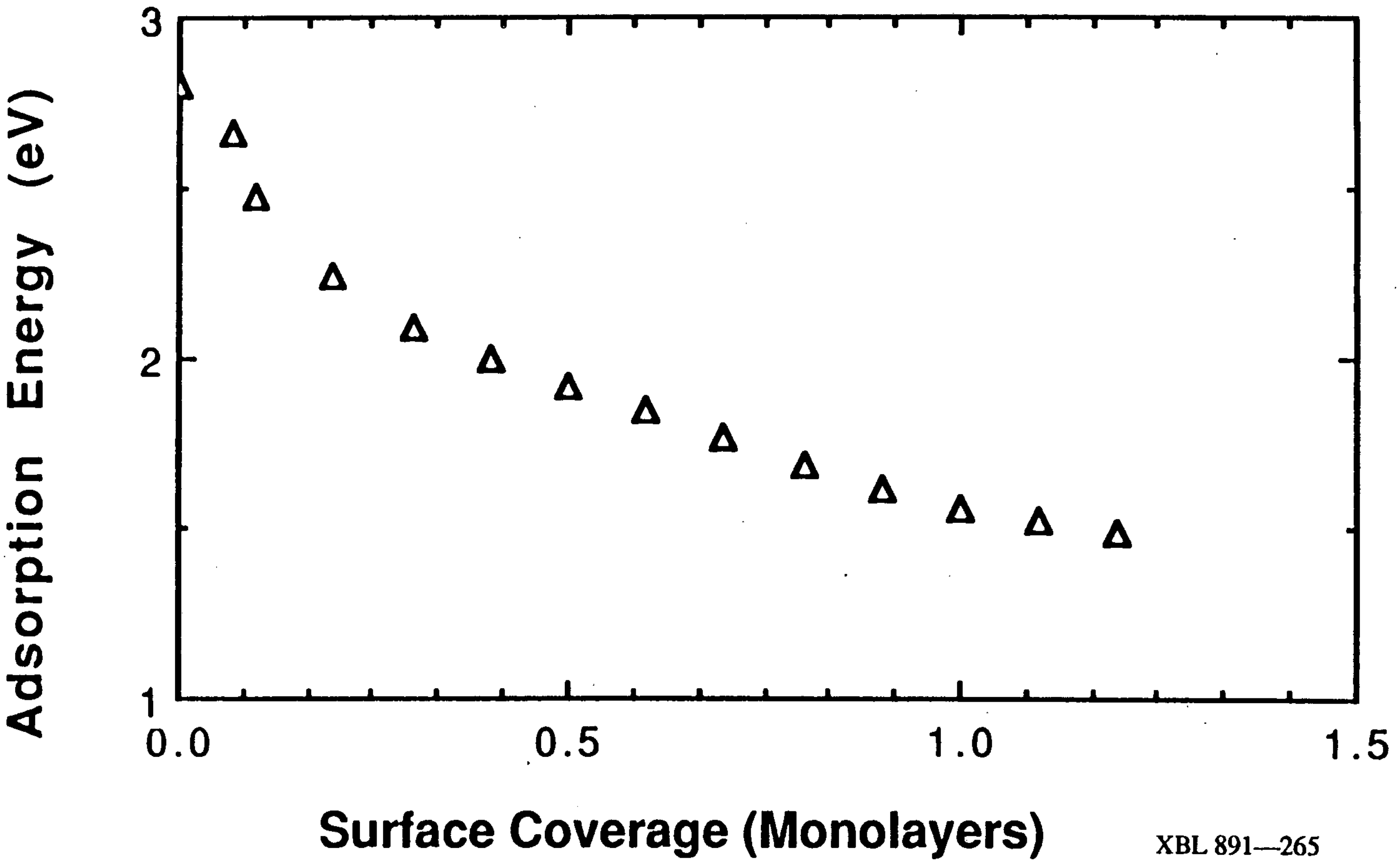

XBL 891—265

Fig. 2-6 A Plot of the Lithium Adsorption Energy vs. Lithium Coverage

Results for the Dimer Model

Fig. 2-7 is a plot of the percentage of lithium evaporating in the form of molecules, as a function of the temperature of the hot wall area. The source density (both atoms and molecules) was maintained at 10^{15} cm^{-3}. The upper curve (area variable) was calculated with ß varied to achieve the maximum dimer fraction. ß was given a lower limit of 0.1% as a matter of practicality. Lower values would be extremely difficult to achieve experimentally. The optimum fractional area ranged from 0.1% to 4%, with the lower temperature points requiring a larger ß for evaporation to offset the lower evaporation rates. Without the lower bound on ß, the dimer output would increase continuously with higher temperature as expected. The lower bound however, causes the dimer output to drop at higher temperatures due to a higher E_a caused by low lithium coverage (see Fig. 2-6). The best results of ~40% were obtained at a temperature of 1100°K.

The lower curve (area fixed) represents the results obtained when all temperatures are constrained to have a ß of 5%. The dimer yield goes down with temperature due to low surface coverage of lithium. For this curve, 900°K is optimal with a dimer fraction of over 18%. Lower temperatures would not improve this figure since the 900°K point is already at the minimum of the E_a curve.

The variation of the dimer fraction as a function of the ion source density is shown in Fig. 2-8 for a temperature of 1100°K. Again, the upper curve (variable area) is calculated with ß

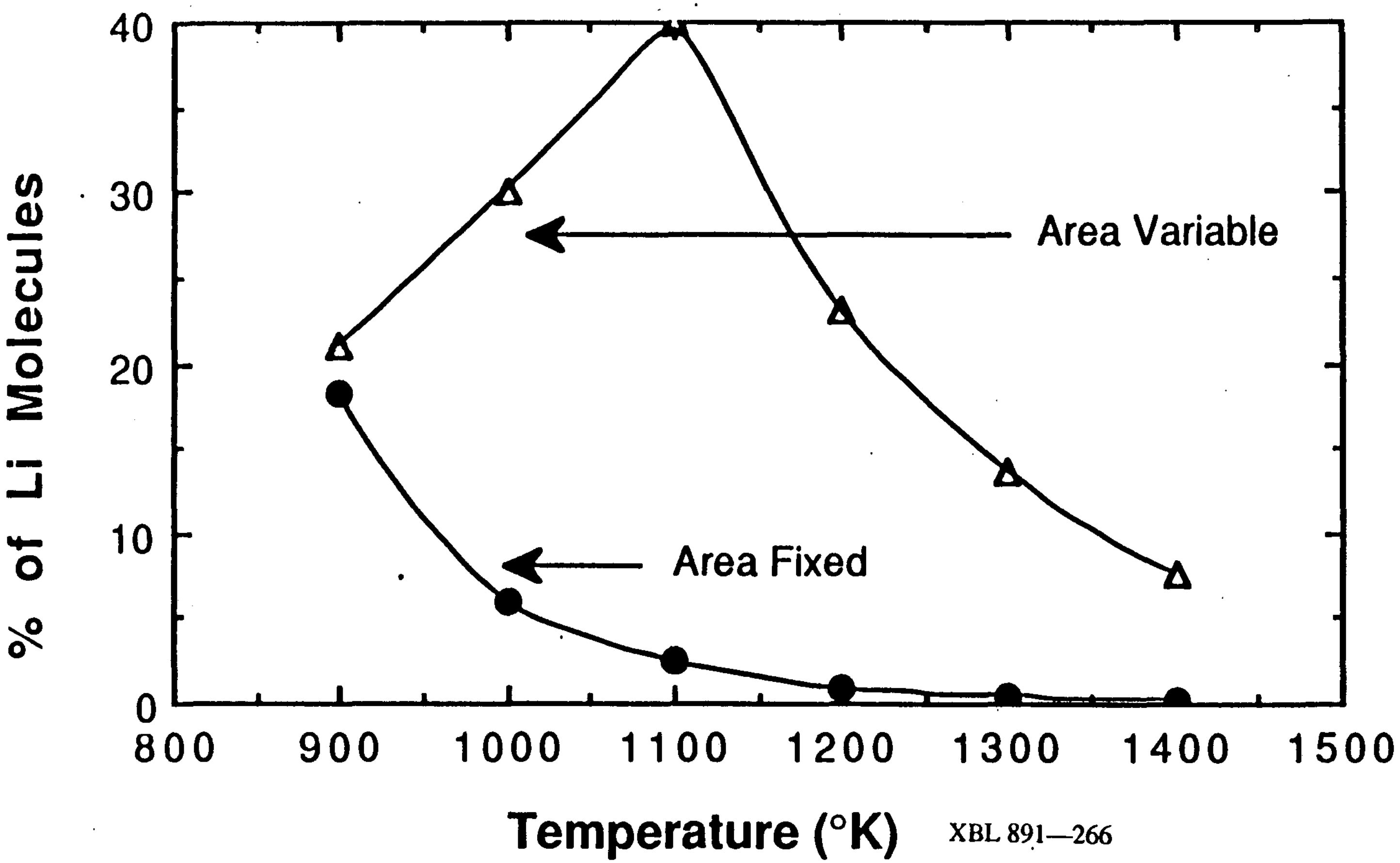

Fig. 2-7 A Plot of the Percentage of Lithium Evaporating as Molecules vs. the Temperature of the Hot Wall Area for the Cases of Fixed and Variable Wall Area

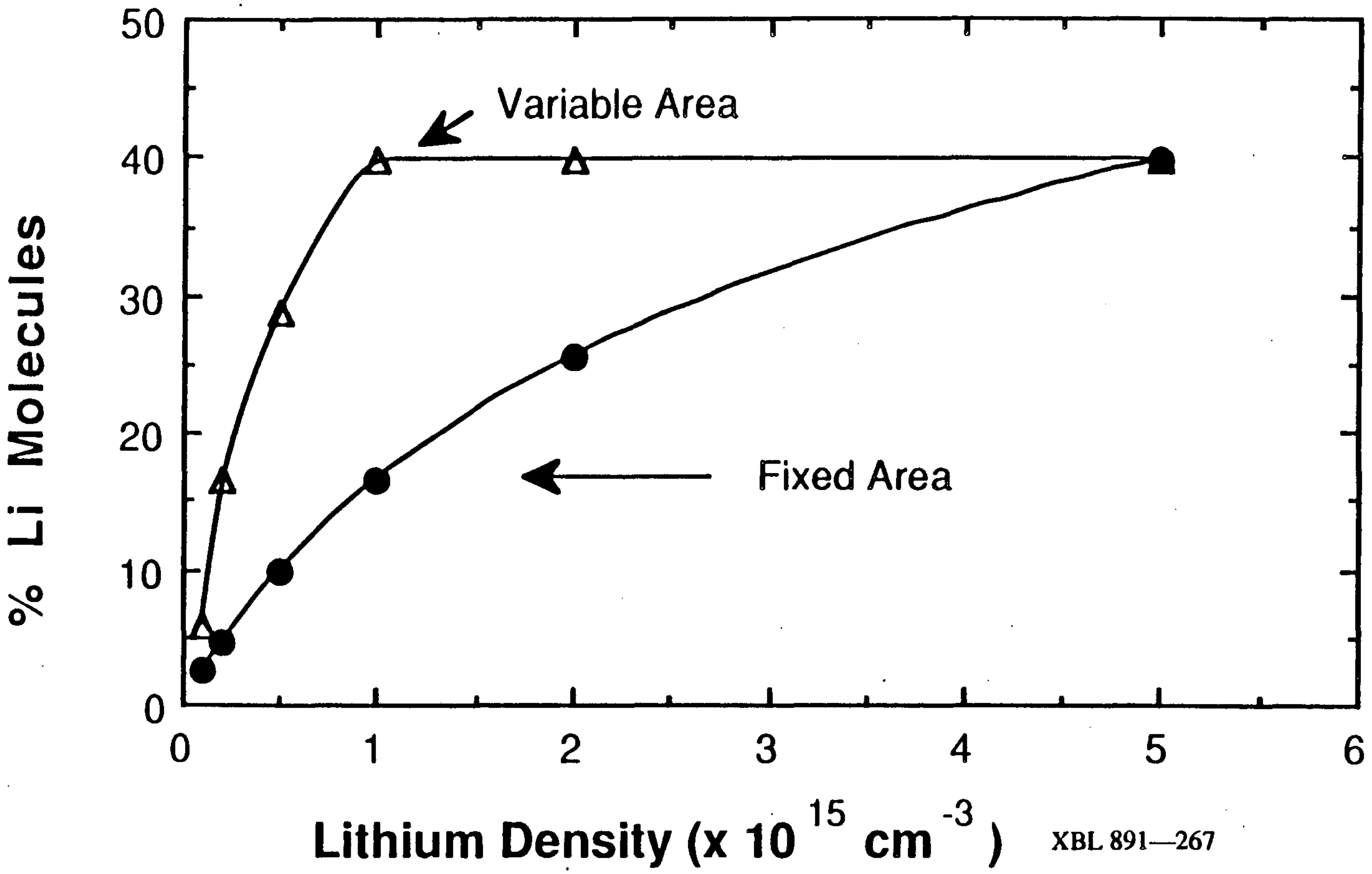

Fig. 2-8 A Plot of the Percentage of Lithium Evaporating as Molecules vs. the Neutral Atomic Lithium Density in the Ion Source

optimized, but subject to the 0.1% lower bound. As the density increases, so does the dimer fraction until the surface coverage reaches 1.2 ML. At this coverage E_a is minimized, and no further improvement in dimer fraction can be achieved at this temperature. The lower curve (ß of 0.5%) has a similar behavior, only the surface coverage limit is not reached until the source density reaches 5×10^{15} cm^{-3}. This result points to operating the source at high neutral densities for high dimer output, as noted earlier for pure lithium.

Fig. 2-9 is a plot of the dimer fraction as a function of ß for a temperature of 1100°K and a source density of 10^{15} cm^{-3}. The dimer output is a steep function of ß. Fig. 2-10, which is a graph of the lithium coverage as a function of ß for the same conditions, shows that for a larger ß the lithium coverage is reduced. Lower coverages increase E_a and decrease the dimer output in turn, so the ß dependence of Fig. 2-9 is really due to the change in E_a.

These results indicate that the optimal situation is to minimize ß, and use the highest temperature that maintains at least one ML coverage of lithium on the tungsten surface. Even if a ß of 0.1% is impractical, 5% provides a dimer fraction (18%) that is much larger than a similar equilibrium case. Dimer fractions of greater than 10% seem feasible without exotic lithium plumbing and at reasonable source neutral densities. It should be noted that these calculations represent only the atoms and molecules leaving the wall surface, once in the discharge dissociation will tend to reduce the steady state dimer fraction. However, this effect is not expected to be large, since the dimer lifetime due to wall

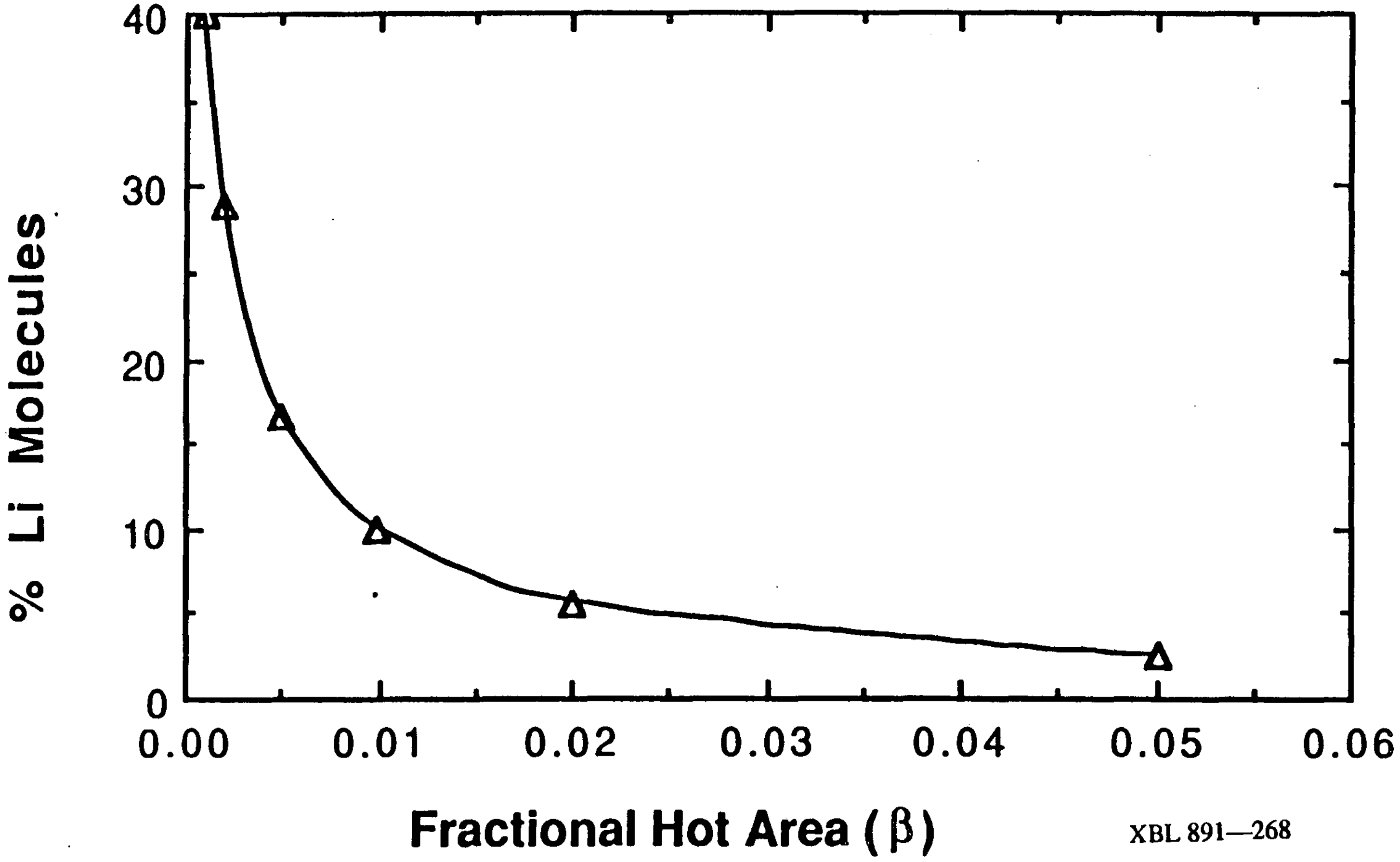

Fig. 2-9 A Plot of the Percentage of Lithium Evaporating as Molecules vs. the Fraction of the Ion Source Wall that is Hot

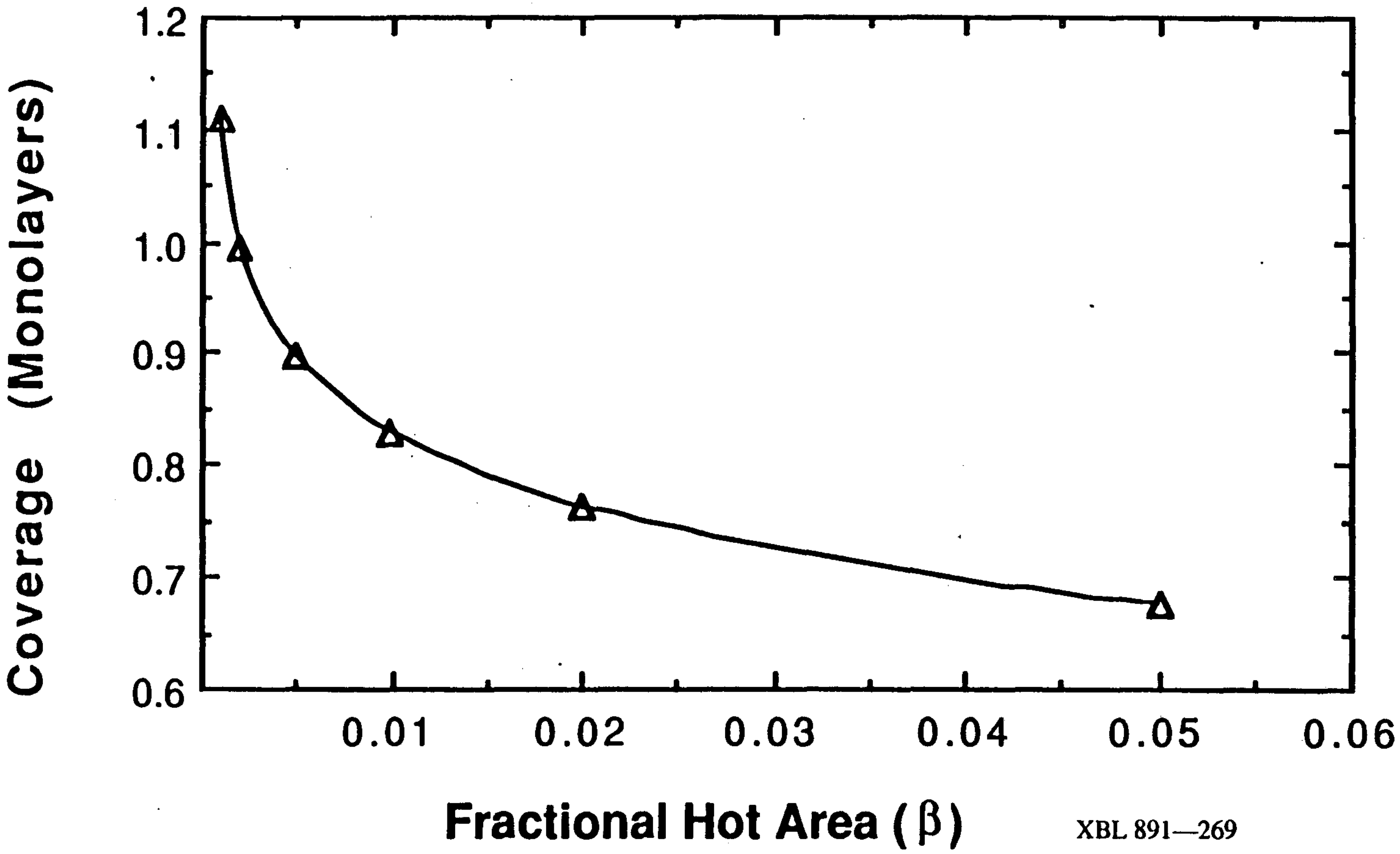

XBL 891—269

Fig. 2-10 A Plot of the Lithium Coverage on the Ion Source Walls vs. the Fraction of the Ion Source Wall that is Hot collisions is extremely short. In fact, wall loss of dimers dominates all other losses in a small ion source with a moderate plasma density by orders of magnitude.

Summary

This chapter has presented a model for how both Li^- and Li_2 are formed in the ion source, and calculated how experimental parameters can be optimized to achieve the best results. The use of a tandem discharge geometry has been shown to provide a significant improvement in Li^- output versus a single chamber discharge. To obtain high current densities of Li^-, increasing the plasma density and dimer fraction are of fundamental importance. The calculated current density scales almost directly with both parameters. The source neutral density clearly has an optimum, which is governed by collisional de-excitation of $Li_2(v^*)$ by atoms. Densities at or below 10^{15} cm^{-3} are most appropriate. In the extraction chamber, as short a length as practical is best along with as low of an electron temperature as possible. This result is similar to that obtained by Hiskes for H^- ion sources.[23] The model predicts that current densities of several mA/cm^2 should be achievable with plasma densities in the mid 10^{12} cm^{-3} range.

Implicit in most of the results of the ion source model was a fairly high dimer fraction (ten percent). The results of the dimer formation model show that this figure is not unreasonable and may be improved. High dimer fractions (up to forty percent) are obtainable with very localized evaporation from a hot tungsten surface coated with lithium. Best results are achieved when only a very small fraction of the ion source wall is 'hot', the rest being at a relatively cool temperature (T_{wall} < 750°K). Hot wall temperatures in the range of 900 to 1300°K appear feasible, with hotter temperatures favored if at least a monolayer coverage of lithium can be maintained on the surface. This improvement, when compared to pure lithium, stems from the lower adsorption energy of a lithium atom on a lithium coated tungsten surface and the nonuniform evaporation.

These results show that a modest ion source design should be able to provide current densities appropriate for fusion diagnostic purposes. Scale-up in density and further improvements in the dimer fraction may allow consideration of Li^- ion beams as alternatives to D^- for generating neutral beams for heating and current drive in tokamaks.

Chapter 3 Li^- Ion Source - Design and Experiments

Ion Source Design and Operation

The motivation for this experiment was not to test the theoretical model developed in chapter 2, but to provide a proof of principle test of volume Li^- production in a plasma discharge. In fact, the model was developed long after the experiment was completed. Volume Li^- ion production by optically exciting high vibrational states in Li_2 molecules, which subsequently dissociatively attach to low energy electrons produced by photoionization, has been demonstrated by McGeoch and Schlier.[40] However, it is much more economical to produce Li^- ions in a discharge, since the efficiency of electron impact excitation or ionization is much higher than that of corresponding photon processes, assuming the required cw lasers existed for this purpose. Demonstration of current densities in the mA/cm^2 range would be required for diagnostic purposes, and this experiment will determine if this is feasible.

The first consideration is how to provide lithium for ion source operation. Most experiments involving lithium vapor use a high temperature (>1000°K) oven with a hot (>1100°K) transfer tube to move lithium to the region of interest. However, designing and building a lithium oven and transport system is a project in itself and introduces additional complexity to the operation of the ion source. To avoid these difficulties initial experiments used solid lithium, which was placed inside the ion source prior to operation.

A lithium discharge was initiated by using a low power argon discharge to heat the ion source wall, which evaporated some of the lithium. Once in the vapor phase, lithium completely dominated the ion species in the discharge and the argon gas was removed. Although a pure lithium discharge can be achieved in this manner, there is a time dependence to the neutral density in the ion source. Lithium vapor can escape through the extraction aperture and leave the ion source, or find a cold spot on the ion source wall and condense in solid form. Thus, the neutral lithium density in the source will decrease with time.

An important issue when using alkali metals at elevated temperature is materials compatibility. Lithium at high temperatures reacts with several common materials used in ion sources. Copper and most metal oxide ceramics react strongly with lithium, so the ion source design should reflect that. Covering the standard copper wall surface with refractory metals such as molybdenum and tantalum provided for reliable operation at any temperature used. Insulating surfaces posed a more difficult problem, since the most common high temperature insulators are metal oxide ceramics. Use of a non-oxide ceramic, such as boron nitride (BN), was essential to maintain both the structural integrity and insulating qualities of the ceramic. Only BN insulators were used in the ion source for this reason.

The design of the ion source is very similar to multicusp H^- ion sources but smaller. The reason for using a small ion source is two-fold. First, the magnetic filter can be implemented external to the ion source so that filter rods are not needed. This simplifies the wall design considerably. Second, a small ion source reduces requirements on power supplies and simplifies fabrication. These advantages outweigh the disadvantages such as diagnostic access.

The ion source is constructed of a cylindrical water-cooled copper chamber (2.5 cm diameter by 5 cm long) with the open end enclosed by a two-grid ion extraction system. A schematic diagram of the ion source is displayed in Fig. 3-1. The source chamber is surrounded externally by 16 columns of ceramic magnets to form a longitudinal line-cusp configuration for primary electron and plasma confinement. A computer plot of the magnetic field produced by the longitudinal line-cusp magnets is shown in Fig. 1-8. The use of 16 columns, as opposed to a smaller number, allows a larger 'field-free' region ($B < 10$ G) where the filament is placed and primary electrons are emitted. The magnet columns on the cylindrical wall are connected at the end flange by two rows of samarium cobalt magnets that are also in a line-cusp configuration.

A samarium cobalt magnetic filter near the plane of extraction and external to the ion source divides the chamber into an arc discharge and an extraction region. The filter magnets provide a transverse magnetic field ($B = 250$ G at the center), which serves to prevent energetic primary electrons from reaching the extraction region. However, positive ions, negative ions, and low energy electrons can diffuse across the filter into the extraction region to form a plasma there. The length of the extraction region from the plasma electrode to the center of the filter field is approximately 4 mm.

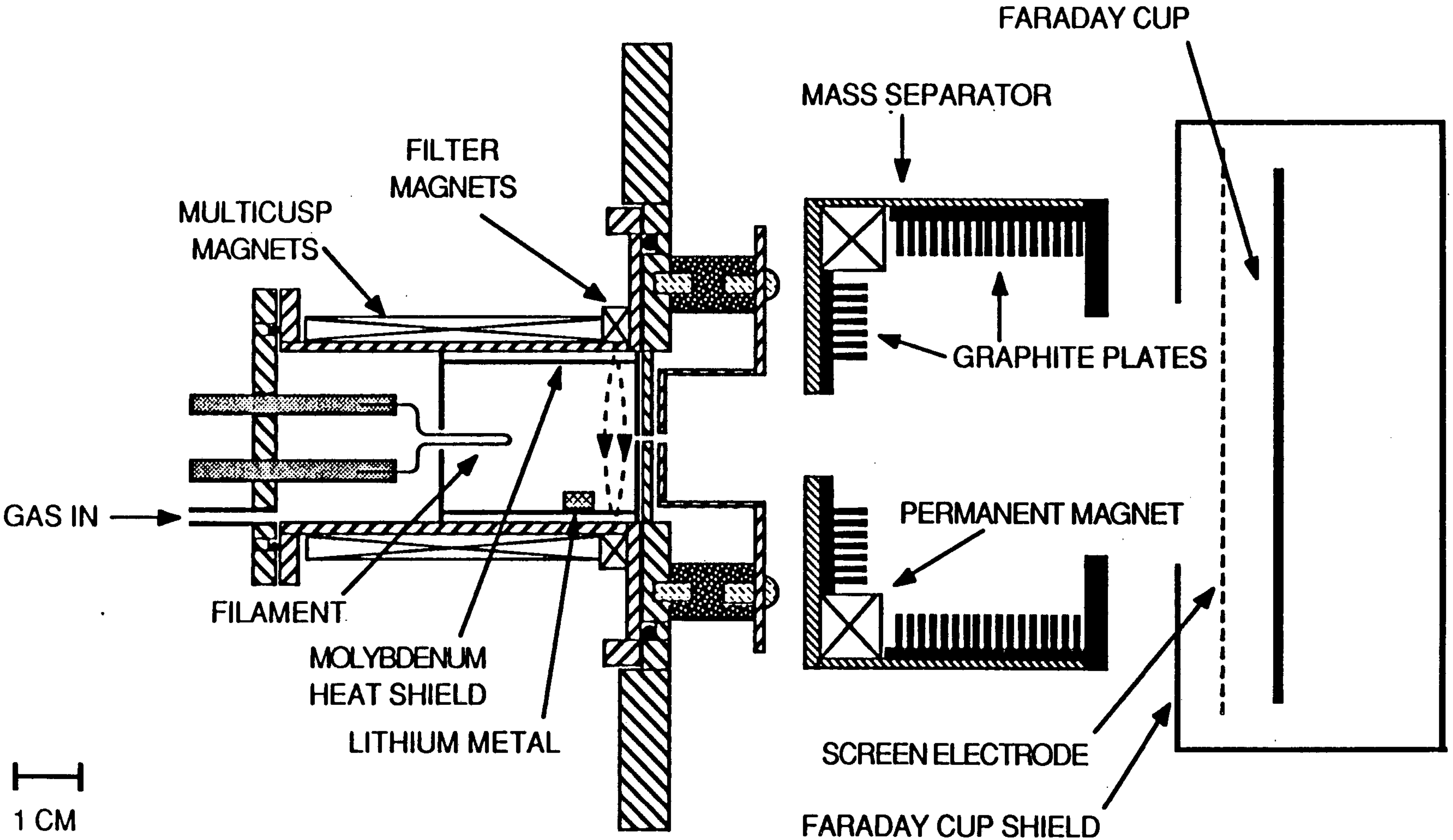

XBL 874—1775

Fig. 3-1 A Schematic Diagram of the Lithium Ion Source, Mass Spectrometer, and Faraday Cup

Inside the source chamber is a heat shield constructed of molybdenum sheet metal (7.6×10^{-3} cm thick), which forms the wall surface. A solid sample of lithium metal is placed in the heat shield and evaporates during operation due to discharge heating. In this manner a substantial vapor pressure of lithium is obtained, at which time the flow of argon support gas can be turned off and a self-sustained lithium plasma is produced. In rough similarity to the model of the previous chapter, a local hot spot is initially produced by the lithium sample, since it sticks into the plasma and is preferentially heated relative to the rest of the ion source wall.

A two-electrode acceleration system is attached to the open end of the chamber. The extraction aperture is 1 mm in diameter giving an extraction area of 7.85×10^{-3} cm^2. The source and the first or plasma electrode are biased negative for negative ion extraction and positive for positive ion extraction. The second electrode is electrically grounded. A plasma is produced by primary electrons emitted by a 0.5-mm-diameter hairpin tungsten filament. The chamber wall, heat shield, and plasma electrode serve as the anode for the discharge.

Located downstream from the second electrode is a compact magnetic deflection spectrometer[53] for measurement of the positive or negative ion species in the extracted beam. In order to measure the negative ion current, the electrons in the extracted beam are removed with a permanent magnet mass separator,[37] which generates a B field strong enough to remove electrons but does not perturb the ion trajectories significantly. The electrons are collected on ridged graphite plates in the mass separator and the current is measured. The remaining beam, composed solely of negative ions, is collected in a Faraday cup. This arrangement, schematically represented in Fig. 3-1, provides the total negative ion current and the ratio of extracted electrons to negative ions.

Although it would be advantageous to have included a Langmuir probe in the source design, reliable probe operation in a lithium vapor environment would be extremely difficult to achieve, even if access for a probe were available. Lithium would condense on the insulating surface of the probe causing a substantial change in collection area, or shorting to the outer conductor. Also, the fabrication of a probe without using metal oxide ceramics is both more difficult and expensive, since suitable BN tubing is not commercially available. Additionally, the small size of the ion source makes the believability of the resulting data dubious, since the probe is likely to significantly perturb the small plasma volume. This is especially true when one considers the probe as both a source and a sink for neutral lithium depending on the temperatures of the probe, insulator, and outer conductor.

Experimental Measurements for Discharge Evaporation of Lithium

1. Dimer Fraction in the Discharge

The ion source was operated with an arc voltage of 40 V and an arc current of 4 A as typical discharge parameters. The mass spectrometer was used to measure both the positive and negative extracted ion species. Fig. 3-2(a) shows the mass spectrometer output signal for the positive extracted ion beam. $^6Li^+$, $^7Li^+$, and Li_2^+ are present in the beam, with $^7Li^+$ composing ~81% of the

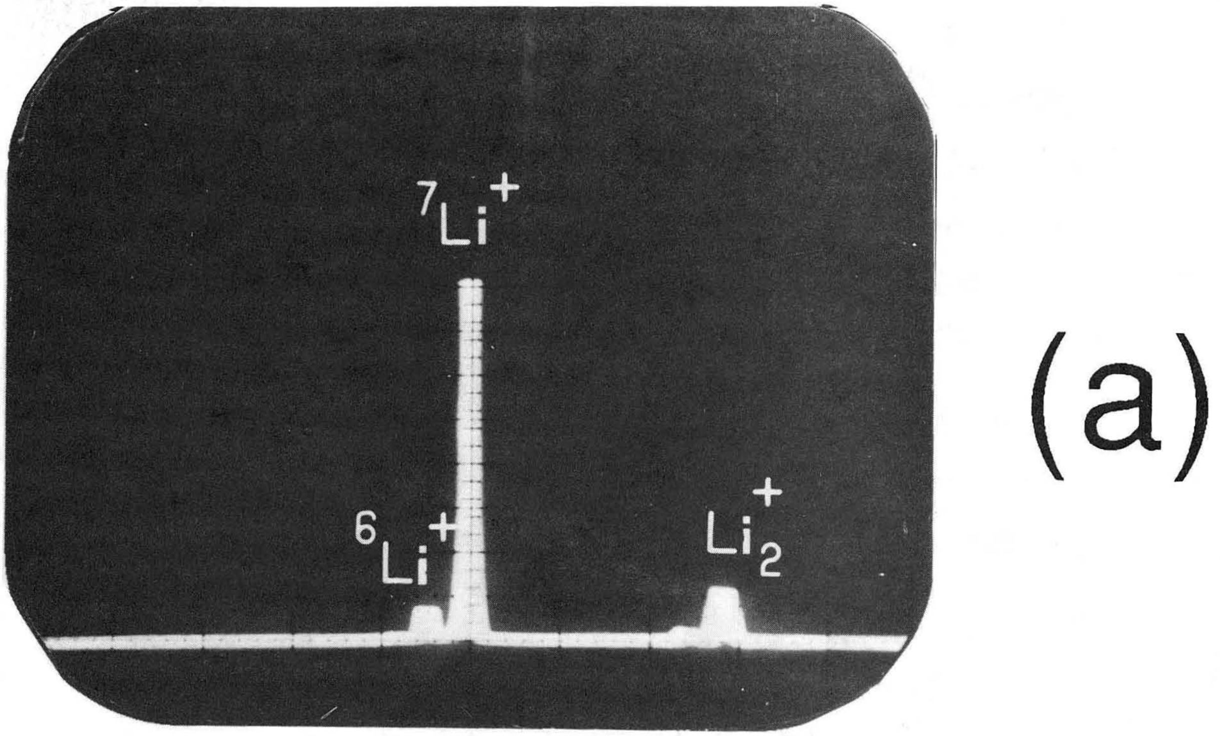

Fig. 3-2 Mass Spectrometer Traces Showing (a) the Positive Ion Species and (b) the Negative Ion Species in the Extracted Beam

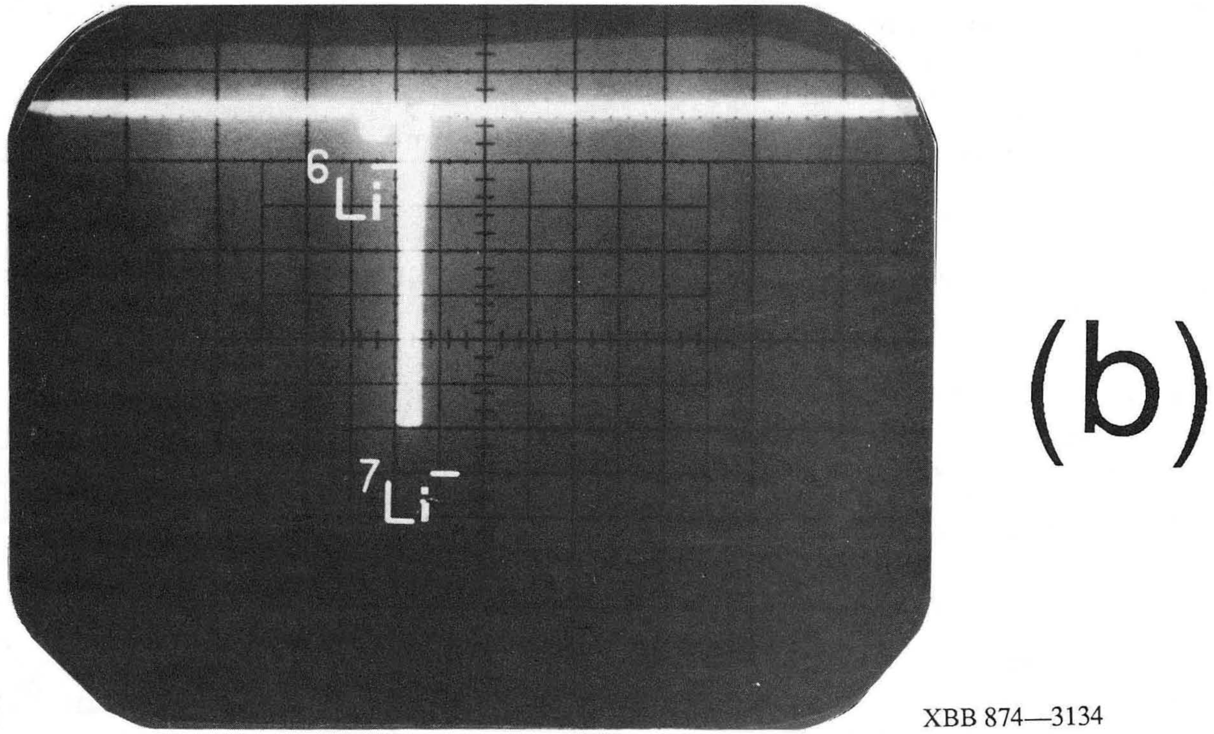

XBB 874—3134

beam current. The small peak at mass 13 is presumably Li_2^+ ions formed by the combination of ^{6}Li and ^{7}Li atoms. The ratio of $^6Li^+$ to $^7Li^+$ ions is exactly that of the natural isotopic mix of lithium.

Using this information, the dimer fraction in the ion source can be estimated. Li_2^+ ions compose ~12.3% of the total lithium positive ion current. To calculate the corresponding ion fraction in the ion source, the velocity difference between atomic and molecular ions in the beam must be taken into account. Li_2^+ ions in the beam have a velocity that is $2^{-1/2}$ that of $^7Li^+$, hence the percentage of Li_2^+ ions in the ion source is $2^{1/2}$ times that in the beam or 18.4%. To infer the neutral species ratio from this, the difference of ionization cross sections must be accounted for. Unfortunately, the electron impact ionization cross section for Li_2 is not known. However, an estimate can be made using hydrogen data, since only the ratio of the atomic to molecular ionization cross section is needed. The lithium discharge is characterized by 40 eV primary electrons, which perform most of the ionization. To translate this to the hydrogen system, a corresponding electron energy is given by 40 eV multiplied by the ratio of hydrogen to lithium ionization energies (13.6/5.4), giving an electron energy of ~100 eV. For an electron energy of 100 eV, the ratio of atomic to molecular hydrogen ionization cross sections is ~0.67.[54] Hence, to infer the percentage of Li_2 in the neutral species of the discharge the percentage of molecular ions (18.4) must be corrected for the larger ionization cross section of the molecules relative to the atoms (~0.67). This gives a value of 12.3% as the percentage of Li_2 in the neutral species in the ion source. The preceding calculation is subject to some error due to using the hydrogen data to determine the lithium ionization cross section ratio, but this error should not be too large because other atomic/molecular systems have similar cross section ratios (0.56 for nitrogen, 0.57 for oxygen).[54] Therefore, the use of a ten percent dimer fraction in the calculations of chapter 2 is experimentally justified.

2. Neutral Lithium Density in the Ion Source

Lithium vapor pressure is not easily measured, since most measurement systems cannot be maintained at a temperature sufficient to prevent lithium condensation. However, an estimate of the lithium density can be made by using a known argon density in the source and measuring the ratio of $^7Li^+$ to Ar^+ ion peaks. A small amount of argon was in the discharge, but Ar^+ was not detected in Fig. 3-2(a), since the extraction energy was too high. If the extraction energy is lowered to allow the mass spectrometer to scan to higher masses, a small Ar^+ peak is noted, which is approximately two percent of the $^7Li^+$ ion peak (or 1.6% of the total beam), for an arc voltage of ~20 V. The ionization cross sections for atomic lithium and argon are well known and allow an estimate to be made of the lithium density in the ion source, if the argon density is known.

The argon pressure in the ion source has been measured with a barocell as about 5.0 mTorr without a discharge (giving a density of $\sim 1.6 \times 10^{14}$ cm^{-3}). When a discharge was present, the argon flow rate was constant, implying that the product of argon neutral density and velocity is also constant. Therefore, the argon density during discharge operation (wall temperature ~673°K), corrected for the change in ion source temperature, was ~1.6×10^{14} cm^{-3} x $(273°K/673°K)^{1/2}$, or ~1.1×10^{14} cm^{-3}.

To determine the neutral lithium density, the ratio of lithium to argon ionization cross sections and beam ion velocities is needed. For an electron energy of 20 eV (primary electron energy), the ratio of cross sections is 7.6.[54] The velocity ratio is given by the inverse of the square root of the mass ratio. Hence, the percentage of argon ions in the ion source is 1.6% x $(40/7)^{1/2}$, or 3.8%. Correcting for the ionization efficiency, the neutral argon percentage is 3.8 x 7.6 or ~29%. The density of lithium would then be 1.1×10^{14} cm^{-3} x 100%/29% or 3.8×10^{14} cm^{-3}, as a rough approximation. This value is near the optimum value calculated in chapter 2 (see Fig. 2-3), which is fortunate since there is very little experimental control over this parameter.

3. Negative Ion Species and Beam Current

Fig. 3-2(b) shows a mass spectrometer trace of the ion species in the extracted negative ion beam. Only Li^- ions (both $^6Li^-$ and $^7Li^-$) were detected. Under normal operation no H^- or O^- impurities were found in the extracted beam. Hence, the negative ion current measured by the Faraday cup was Li^- ions. As previously stated, measurements of the extracted negative ion current and the ratio of extracted electrons to negative ions were made with a permanent magnet mass separator and the Faraday cup. The maximum negative ion current measured was 14.9 μA (corresponding to a current density of 1.9 mA/cm^2) for a discharge voltage of 40 V and a discharge current of 4 A. Actual current densities could be higher, since no effort was made to improve the ion optics.

4. Plasma Density in the Ion Source

The extracted electron current measured by the mass separator was 3.75 mA, which gives an electron to ion ratio of 250 to 1 for the extracted beam. This ratio can presumably be improved when the magnetic filter geometry is optimized.[55] The extracted electron current measurement allows an estimate to be made of the plasma density in the extraction region of the ion source, if the electron temperature is known. Without probe measurements, this information is not available, but a good estimate can be obtained by using the electron temperature measured in similar hydrogen discharges, as done in chapter 2 where T_e was given a value of 0.35 eV.[37] The density in the extraction region is given by:

$$n_e = 4I/(evA), \qquad (3\text{-}1)$$

where I is the electron current, e is the electronic charge, v is the thermal electron velocity $(8KT_e/\pi m_e)^{1/2}$, m_e is the electron mass, and A is the extraction area. Using the appropriate values for T_e, A, and I, an electron density of 3×10^{11} cm^{-3} is obtained. This is the extraction chamber density and corresponds to a first chamber density of 1.5×10^{12} cm^{-3}, for comparison with the model of chapter 2.

5. Time Dependence of Positive and Negative Ion Output

The time dependence of the Li^+ ion signal and the percentage of dimer ions in the extracted ion beam are plotted in Fig. 3-3. As expected, the Li^+ signal decreases with time due to a decrease in neutral density in the source with time. Likewise, the dimer ion fraction falls off very quickly in time, which can be explained in several ways. As the neutral density in the source becomes smaller, the surface coverage of lithium on the heat shield is reduced, which increases the adsorption energy, resulting in a lower dimer evaporation rate. Also, the lithium sample, which was preferentially heated by the plasma, is melted and dispersed over time, giving rise to a more even heat shield temperature distribution, which is less favorable to dimer formation.

Negative ion output as a function of time is plotted in Fig. 3-4. The Li^- ion signal quickly decreases with time, then reaches a region of very gradual decay after ten minutes. The reason for the decline is obvious, since both the plasma density and dimer fraction (inferred from the fraction in the beam) decrease with time. However, the Li^- signal is still present even when the dimer ion fraction is negligible. This implies either there are dimers that do not survive long enough to leave the ion source as ions, or that there is another source of Li^- ions in addition to dissociative attachment. The second case may involve surface production or perhaps charge transfer between neutral and electronically excited lithium atoms. At moderate to high neutral densities, it appears that dissociative attachment is the dominant formation process for

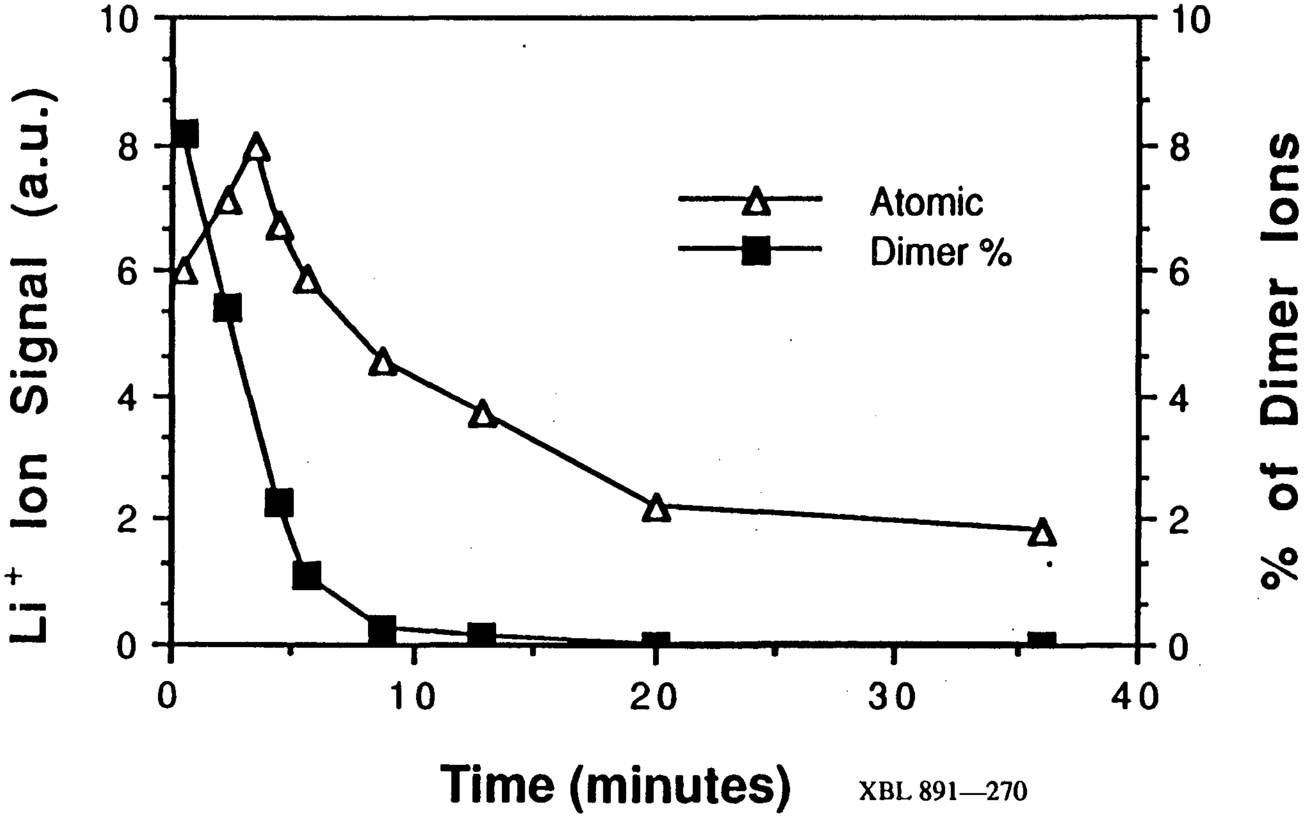

Fig. 3-3 Time Dependence of the Positive Lithium Ion Species

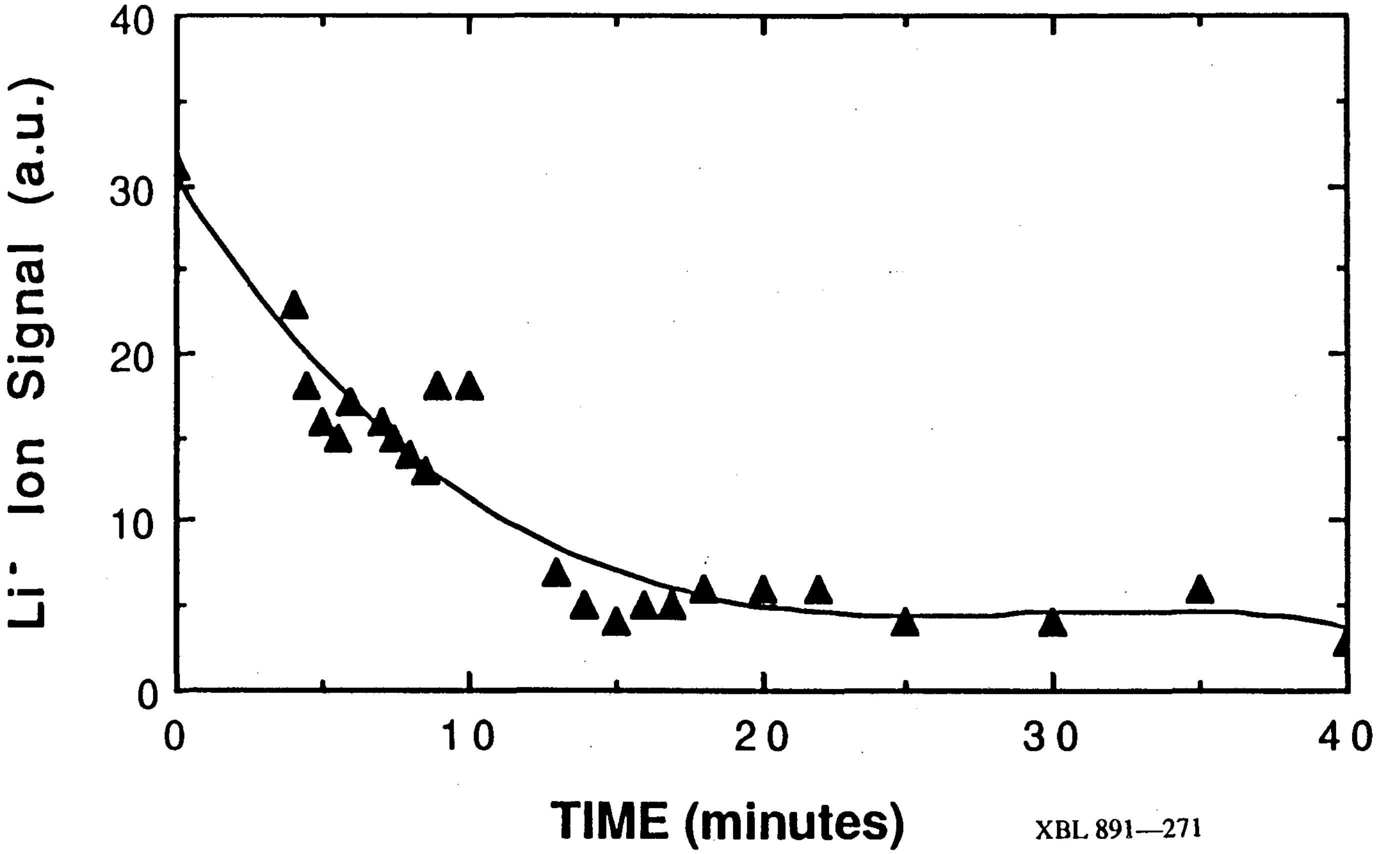

Fig. 3-4 Time Dependence of the Negative Lithium Ion Current

Li^- ions, due to the observed dependence on dimer molecules and the need for a magnetic filter to achieve optimal results. (Elaborated on in the following section.)

6. Comparison of Theory and Experiment for Li^- Ions

With the experimental results presented above, a comparison between the the theoretical model of the lithium ion source and experiment can be made. The experimental parameters were an electron density $3x10^{11}$ cm^{-3} in the extraction chamber (or $1.5x10^{12}$ cm^{-3} in the first chamber), a dimer fraction of 12.3%, a neutral lithium density of $3.8x10^{14}$ cm^{-3}, and an extraction chamber length of 4 mm. The electron temperatures for both regions used in the model will again be used for comparison. A model calculation using these parameters gives an extracted Li^- current density of 1.6 mA/cm^2 for a tandem discharge. This is in excellent agreement with the experimental value of 1.9 mA/cm^2. Given the number of approximations and assumptions, the error of about fifteen percent is much better than one has a right to expect. It should be noted that the experimental value of Li^- current density is the best achieved, and not an average.

If the filter magnets are removed from the ion source, a single chamber results. The model predicts approximately a factor of four decrease in Li^- current density. Experimentally, the Li^- ion output drops to a negligible value without the presence of the magnetic filter. This implies that the model may in fact be underestimating the effects of electron collisional detachment. If this is the case, then only the single discharge results of the model would be affected. This result is consistent with the assumption of dissociative attachment as the dominant Li^- ion formation mechanism.

It would have been useful to investigate parameter scalings, but the nature of the experiment makes this difficult. Ordinarily, plasma density is easily controlled by adjusting the arc current and voltage in the discharge. However, the coupling of the evaporation rate to discharge heating and hence to plasma density, and the rapid time evolution of the discharge as the lithium sample evaporates makes scaling studies a problem. In any case, the point of the experiment was a proof of principle test of volume Li^- production in a discharge, not a validation of as yet underived theoretical models. In this respect the test was quite successful, showing the feasibility of a tandem plasma discharge for producing Li^- ion beams for diagnostics.

7. Comparison of Theory and Experiment for Li_2 Molecules

The lithium ion source was found to have a dimer content of approximately 12.3%. Since little is known about the actual temperature and area of the effective lithium evaporation zone, the model for Li_2 formation may provide some clues about conditions in this region. It is likely, due to the amount of lithium placed in the ion source, that the hot region is large. The lithium sample was of an area of ~1 cm^2, while the heat shield had a total surface area of ~32 cm^2. Therefore the fractional hot area, β, is roughly three percent. It follows that the temperatures involved were at the low end of the scale. Using Fig. 2-7, one can estimate that the hot temperature, where the lithium sample was placed, was ~950°K since this gives a dimer fraction of about ten percent with a ß of five percent. Using the model and solving for the conditions of 12.3% dimers, a ß of three percent, and a neutral density of 3.8×10^{14} cm^{-3}, a wall temperature of ~920°K is obtained. The graph of Fig. 2-7 (area fixed) would imply that slightly lower temperatures should be more advantageous, but there is no temperature control knob for the liner.

Experiments with a Lithium Oven

In order to operate the ion source in steady state, a lithium oven was fabricated to maintain a constant neutral density in the ion source. The requirements for this oven are operation at high temperatures, up to 1300°K, small size, ease of lithium loading, and reasonable power consumption. Since the oven and ion source must be connected by some kind of lithium vapor transport pipe which restricts vapor flow, high oven temperatures are required to drive sufficient vapor into the source to maintain a high neutral source density. The need for small size is due to the necessity for joining the oven to the ion source, which itself is quite small, and the physical space available at the test stand where the experiment was conducted. Periodically the oven will have to be reloaded with lithium after the previous supply is used up. Hence, the oven should be easy to load with lithium even after extended operation at high temperatures. Reasonable power consumption is dictated by the need to fit all power supplies into a high voltage area with limited line power supplied through isolation transformers.

At an operating temperature well over 1000°K, an effective vacuum seal for the oven is very difficult to fabricate. The approach taken for this oven was to enclose it in a separate water cooled vacuum enclosure with standard O-ring seals. Thus, high temperature vacuum seals are unnecessary. Ordinarily, a valve is placed in the connection between the oven and the ion source in order to control the vapor flow. Again, designing a functional valve at these temperatures is a problem, therefore flow control was maintained by controlling the operating temperature of the oven and the valve was eliminated.

Materials compatibility is a serious problem for the oven. Metal oxide ceramics were avoided as much as possible, and replaced by BN insulators. The oven itself, with a volume of ~8 cm^3, was of welded 314 stainless steel construction, as was the transport tube and radiation shielding. Electrical connections were made using stainless steel or tungsten wire. The oven was heated with commercially available heater wire that used an inner nichrome heating element surrounded by magnesium oxide electrical insulation and covered with a sheath made of inconel which was welded to the outside of the oven (see Fig. 3-5). The top of the oven was welded to the transport tube and bolted to the lower part of the oven. A nickel gasket formed a vapor seal to keep lithium from escaping at the joint. The transport tube was composed of two concentric tubes welded at the top. A current was passed through the tubes to electrically heat them to

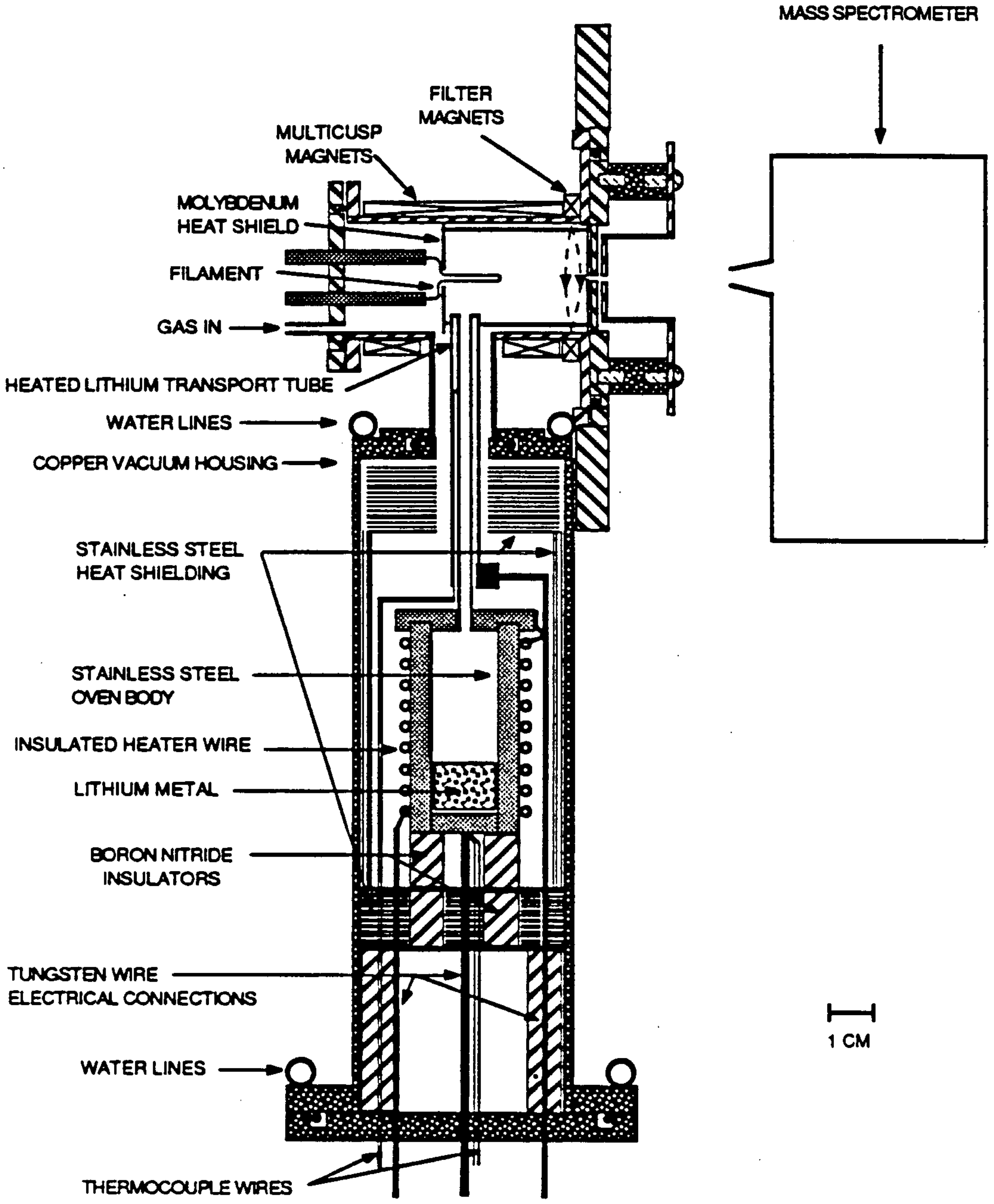

XBL 891—272

Fig. 3-5 A Schematic Diagram of the Lithium Oven and Ion Source operating temperatures. When the copper vacuum housing of the oven assembly was connected to the ion source, the top of the transport tube fit into a hole in the heat shield of the ion source as shown in Fig. 3-5.

Temperature monitoring was provided by two alumel-chromel thermocouple junctions. One was spot welded to the base of the oven, and the other was spot welded to the inner transport tubing and insulated with quartz cloth. The oven and the transport tube had separate power supplies for independent temperature control, since the transport tube should be operated hotter than the oven in order to prevent lithium condensation. For operation at ~1270°K, the oven required about 180 W and the transport tube ~50 W of power.

Experiments using the lithium oven as the source of lithium for the ion source had very different results than those obtained by evaporating lithium in the ion source. Fig. 3-6 (a) shows the output of the mass spectrometer when a positive ion beam is extracted from the ion source operating with an arc voltage of 80 V and an arc current of 3 A. The oven was maintained at a temperature of ~1100°K. The dimer ion fraction is less than two percent and the signal intensity is lower than previous results. Thus, both the neutral density in the ion source and the dimer fraction are likely to be low. This explains the very low Li^- ion output shown in Fig. 3-6 (b), when the source is operating at the same conditions except for an arc current of 2 A. In light of the results of the model for Li_2 formation, the low dimer output is due to both a low neutral density in the ion source and the lack of any preferential

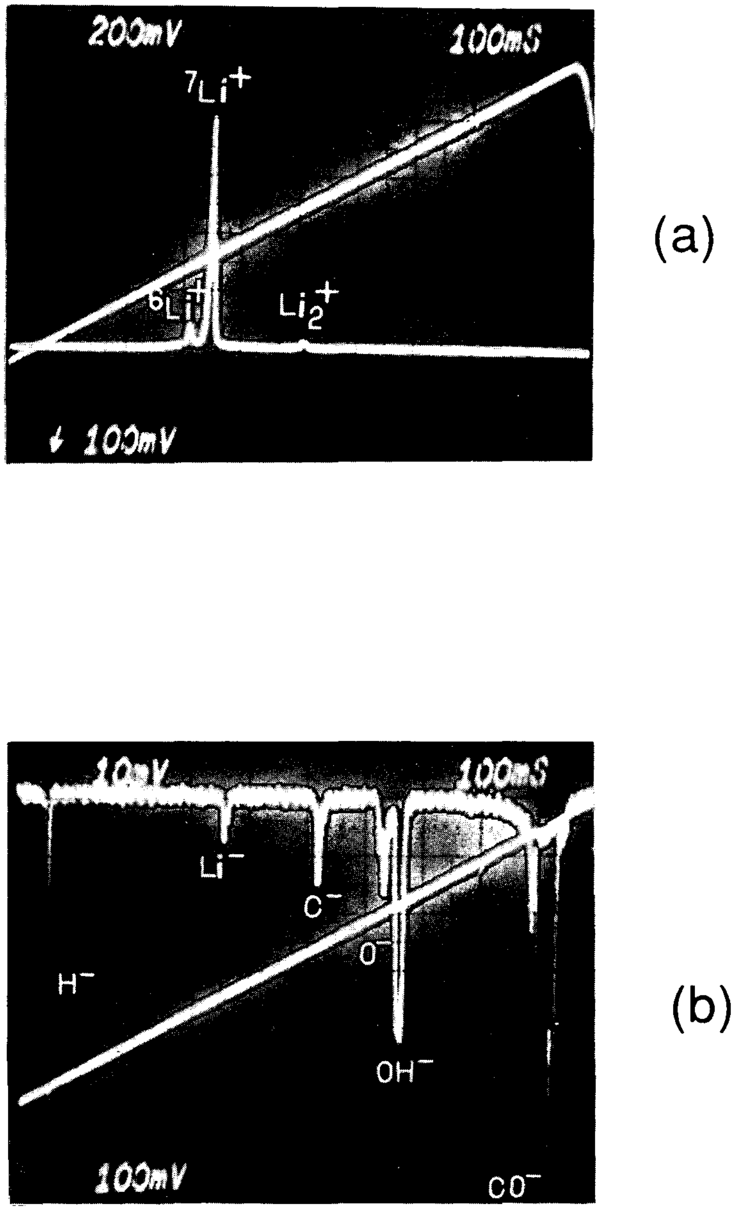

XBB 880-10624

Fig. 3-6 Mass Spectrometer Traces of (a) the Positive Ion Species, and (b) the Negative Ion Species, when the Lithium Oven is Used as the Source of Lithium evaporation, i. e. a hot spot. With a low neutral density and a low dimer fraction, the model would also calculate a low Li$^-$ current density as observed. However, the source could be operated in a steady state manner with the lithium oven.

With a low neutral density, the obvious remedy is to operate the lithium oven at higher temperatures in order to drive more lithium vapor into the ion source. However, as the temperature of the oven is raised, more and more impurities are released from the oven assembly and drift into the ion source. Some of these impurities are seen in the negative ion mass spectrum of Fig. 3-6 (b). The impurities are presumably caused by the outgassing of the oven components at elevated temperatures and are not eliminated by an extended bakeout of the oven. Thus operation with an oven would require some modification in design, in order to achieve the proper throughput of lithium vapor at lower temperatures. This could be done by shortening and enlarging the lithium transport tube. However, the dimer fraction would still be unacceptably low.

Shortcomings of These Experiments and Their Implications on Design of Future Negative Lithium Ion Sources

The Li$^-$ model shows further improvements are likely to be achieved with higher plasma densities and higher dimer fractions. Also, the source neutral density must be maintained for steady state operation. While evaporation of lithium directly in the discharge proved very successful in producing Li$^-$ ions, this result could not be maintained in steady state. Source operation with an oven resulted in a steady state discharge, but with a very low Li$^-$

output. Evidently the design of an improved Li^- ion source should incorporate features of both experiments. The following section details these design features based on the theoretical and experimental results of the previous work.

For diagnostic applications, a somewhat larger source would be desirable in order to increase the usable extraction area, improve plasma confinement, and allow better access for temperature control of the heat shield or liner. A source of ~7.5 cm diameter by 15 cm long should be large enough without making the source cumbersome. Such a source would require internal filter rods to generate the magnetic filter field, and use a tungsten or LaB_6 cathode. The use of ten rows of multicusp magnets would improve plasma confinement, while the loss in magnetic 'field-free' volume relative to sixteen rows of magnets is more than compensated by the increase in source diameter.

The most important improvement for source operation will be active control of the liner temperature through the use of adjustable heating elements, with independent control of the temperature of the 'hot zone' where evaporation takes place. Thus preferred temperature distributions can be maintained in steady state operation. Also, plasma heating can be compensated for and evaporation rates decoupled from the discharge parameters. Therefore the plasma density, neutral density, and dimer fraction, can be independently optimized.

As was done in the previous lithium experiment, the extraction electrodes should operate at high temperatures to prevent lithium condensation. This was accomplished by allowing the plasma to heat the first electrode, and by electrons in the extracted negative ion beam heating the second electrode. While this arrangement generally worked to keep the extraction aperture open, the first electrode was often the coldest part of the liner and a preferential area for condensation. The improved design would not leave the extraction electrode temperature to chance, but would use controllable heating elements similar to the liner.

Supplying lithium to the ion source in a controlled manner can be accomplished without a high temperature oven. A low temperature oven operating at ~500°K simply to melt the lithium would be connected to the ion source via a valve and a transport tube operating at temperatures of ~600°K. This system would deliver small amounts of liquid lithium controllable both by the valve and the pressure of an inert gas in the oven. The level of impurities introduced into the ion source from the oven should be negligible with these low operating temperatures and, due to the valve, the capability of loading lithium in an inert atmosphere.

Other parameters such as filter strength and axial position remain to be optimized in the new design. Plasma density should be increased to the 10^{13} cm^{-3} range for improved Li^- current density, while the dimer fraction should be maintained or improved through better liner temperature control. These improvements should provide current densities in the 10 mA/cm^2 range, which is more than sufficient for diagnostic purposes. The following chapter is devoted to using this upgraded Li^- ion source for a proposed diagnostic neutral beamline suitable for making magnetic pitch angle and magnetic field strength measurements in situ[4,39] in tokamaks of the ITER parameter range.

Summary

The results of experiments on a small multicusp Li^- ion source show that reasonable current densities for diagnostic applications are easily achieved. It remains to extend this result to steady state operation in a source with a larger usable extraction area. Key areas for improvement are control of liner temperature and supply of lithium to the ion source. However, there are no outstanding technical problems involved in doing so. Thus Li^- ion sources suitable for diagnostic applications can be achieved with only modest additional development.

Chapter 4 Design of a Lithium Diagnostic Beam to Measure Magnetic Pitch Angle on ITER

Introduction

This chapter is devoted to utilizing the negative lithium ion source previously developed (chapter 3), as the basis for a high energy neutral particle beam diagnostic system. A $^{6}Li^{\circ}$ diagnostic beam has been successfully used on the TEXT device for measurement of the radial profiles of the magnetic pitch angle and current density.[3,4] The objective here is the scaling of this system for use with an ITER size tokamak and achieve adequate beam penetration and signal-to-noise (S/N) ratio. Ultimately, the requirements for such a system will be calculated.

Although the magnetic pitch angle is an important parameter for MHD stability, plasma heating, and confinement, direct measurements of the radial profile have been difficult. For example, Faraday rotation of a linearly polarized EM wave by the poloidal field of the tokamak is a chord-averaged measurement requiring a simultaneous determination of the density profile.[5 6] Measurements of collisionally induced Zeeman split transitions of intrinsic or injected impurity atoms suffer from fluctuations in plasma density and temperature, which modulate the excitation rate. The diagnostic method used on TEXT avoids these difficulties by using laser induced fluorescence (LIF) of an injected $^{6}Li^{\circ}$ beam. This method allows the radial profile of the magnetic pitch angle and the current density to be measured during a single shot. $^{6}Li^{\circ}$ is used rather than the more abundant ^{7}Li° because the lighter isotope has better plasma penetration for the same beam energy.

The technique used for this measurement is described in references 3 and 4. Simply put, a ^{6}Li° beam is radially injected into the tokamak at the midplane, along with light from a tunable cw dye laser.[57] The laser excites the ^{6}Li° ($2^2S \rightarrow 2^2P$) transition. Collection optics perpendicular to the B-field allow the local field direction to be determined from the laser polarization angle which produces the maximum LIF signal. Rotation of the laser polarization at a constant angular frequency allows the S/N ratio to be improved by bandpass filtering of the LIF signal.

With the poloidal field known, the local current density can be deduced. Additionally, information about the plasma density and temperature can be obtained using the collisionally induced fluorescence (CIF) of the ^{6}Li° beam. It remains to state why ^{6}Li° was chosen as the beam species. Besides having an appropriate Zeeman splitting in the range of efficient cw laser dyes, lithium is a low Z material, which minimizes radiation losses and Z_{eff}, also a suitable ion source exists from which to generate this beam.

Overview of the TEXT Lithium Diagnostic Neutral Beam

This section briefly describes parameters of the TEXT diagnostic beam and presents a calculation of the attenuation of the beam inside the plasma. The beam is based on a small thermionic positive ^{6}Li$^+$ ion source typically producing ~2.5 mA of current.[3] This beam is electrostatically accelerated to a final energy of ~95 keV. The beam is then refocused and bent in a steering magnet where it is merged with the laser beam. The two beams then enter a sodium vapor cell where the $^6Li^+$ ions are converted to $^6Li^\circ$ with ~40% efficiency. The resulting beam has 1 mA equivalent current in an area of ~1.8 cm^2.

The S/N ratio for the TEXT diagnostic is determined by several factors. First, attenuation of the lithium beam via ionizing collisions, primarily with plasma ions, reduces the neutral atom flux as a function of distance into the tokamak. Second, bremsstrahlung and other radiation sources from the plasma provide an optical noise background to the LIF signal from the lithium beam. Third, CIF also masks the LIF signal. Since the TEXT system has already demonstrated an adequate S/N ratio, scale up to an ITER compatible system simply requires maintaining or improving this S/N ratio based on equivalent beam penetration and a proportional increase in the LIF signal to match the increased bremsstrahlung and CIF of the ITER environment.

The beam energy for the TEXT diagnostic is 15.8 keV/nucleon. At these energies, ionization is primarily by plasma ions. Although impurities are present in the plasma, their effect is usually small[58] and will be ignored. Ionization can also occur via multistep processes, however the density of the TEXT plasma and the low speed of the diagnostic beam makes this contribution negligible. The plasma is modeled as a slab of uniform density. The slab approximation results in only a small difference from a more accurate profile.[58] A density of 2×10^{13} cm^{-3} is chosen as representative, since that is given as an upper limit for adequate beam penetration on TEXT.[59] The cross sections for ionization and charge transfer at 15.8 keV can be estimated as 1.7×10^{-15} cm^2 and 8×10^{-16} cm^2 respectively.[60] This results in a combined beam attenuation cross section (σ) of 2.5×10^{-15} cm^2. Therefore the beam flux as a function of distance into the plasma (z) can be modeled as:

$$\Gamma(z)/\Gamma(0) = \exp[-\sigma n z], \qquad (4\text{-}1)$$

where $\Gamma(z)$ is the ^{6}Li° beam flux at position z in the plasma and n is the average plasma density. The result of this calculation is plotted in Fig. 4-1 as a function of z. The minor radius of the TEXT plasma is ~27 cm, so at the center of the plasma the beam has been attenuated by 74%, while at the far edge ($R = R_o - a$) the beam is 93% attenuated. For the ITER system, the beam penetration should be at least as good to allow some measurements of the magnetic pitch angle to be made on the far side of the plasma.

Although bremsstrahlung and CIF can be discriminated against by chopping the dye laser output, as done for the TEXT system, it seems prudent to scale the LIF proportionally for an ITER diagnostic so as to maintain resolution against fluctuations in the background signal. The appropriate scale up in diagnostic parameters is discussed in the following section. An improvement in S/N ratio could also be achieved by sinusoidally modulating the dye laser intensity at a frequency f, and bandpass filtering the LIF output signal at this frequency to remove almost all of the background noise.

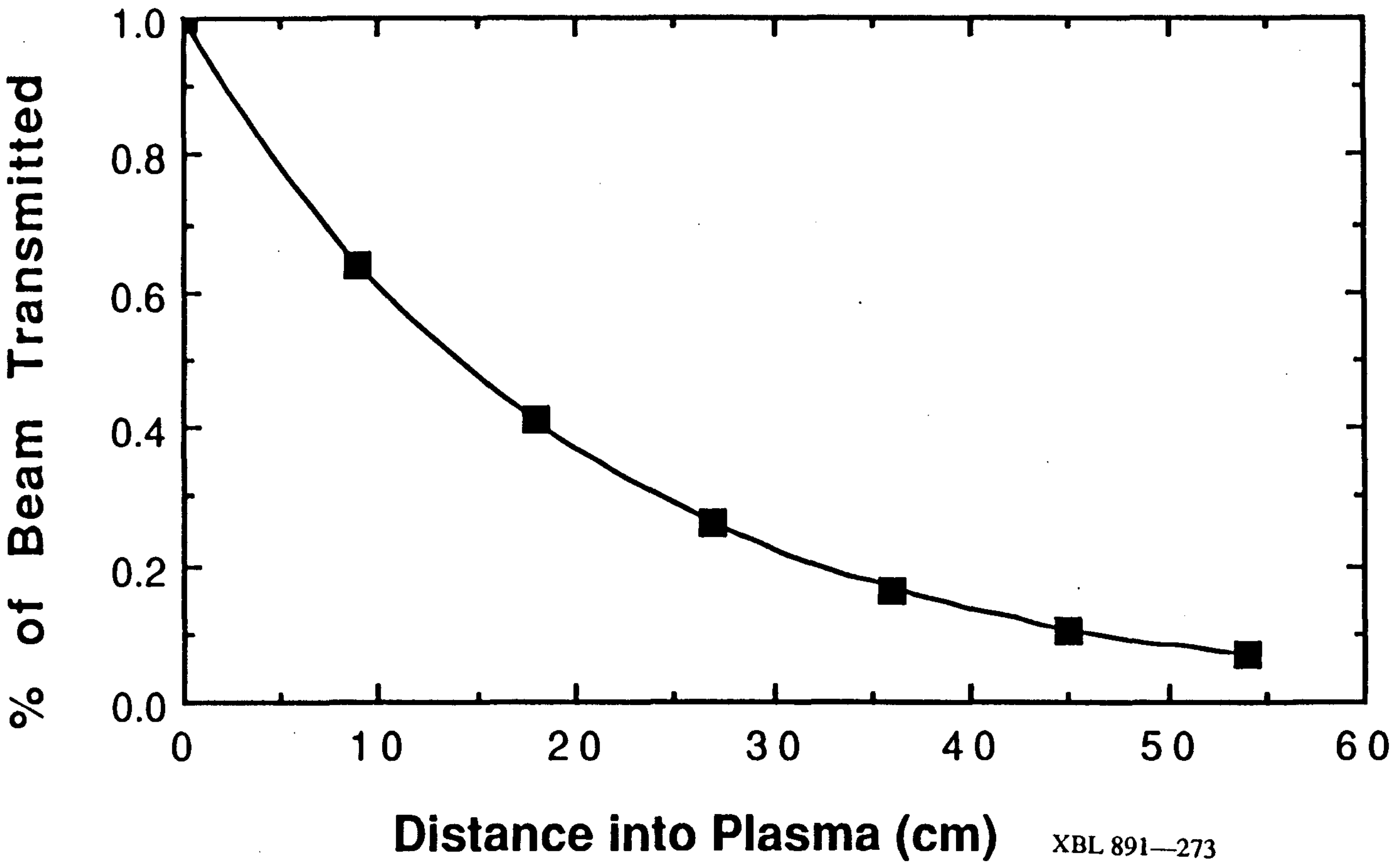

Fig. 4-1 Penetration of the TEXT Diagnostic Beam into the TEXT Plasma (a=27 cm)

^{6}Li° Beam Diagnostic for ITER

The first consideration for a diagnostic beam is the beam energy required to ensure adequate penetration of the ITER plasma. An attenuation cross section for D° beam penetration has been developed, which includes the effects of multi-step ionization and plasma impurities.[61] To adapt this for use with ^{6}Li°, the formula is multiplied by the ratio of the lithium ionization cross section to the deuterium cross section at the energy of interest.[54] This will in fact overestimate the ^{6}Li° beam attenuation slightly, because lithium has a shorter radiative lifetime than deuterium. This reduces the contribution of multi-step ionization. The resulting cross section has a strong dependence on energy. Using this cross section, the proposed ITER average plasma density (pulsed inductive drive) $<n> = 1.6\times10^{14}$ cm^{-3}, and equation 4-1, the beam attenuation at the plasma center can be plotted as a function of beam energy (Fig. 4-2). The beam penetration improves monotonically with increasing energy. Limitations due to cost, accelerator length, energy investment in the beam, and wall damage from complete beam penetration, place an upper bound on the beam energies. A reasonable cap on the beam energy is ~2 MeV/nucleon due mainly to accelerator length and beam penetration. The cost of the overall system will not be addressed. At an energy of 2 MeV/nucleon, the beam transmission to the center of the plasma is 42.4% of the initial beam, while 18% of the initial beam survives a complete transit of the plasma. This

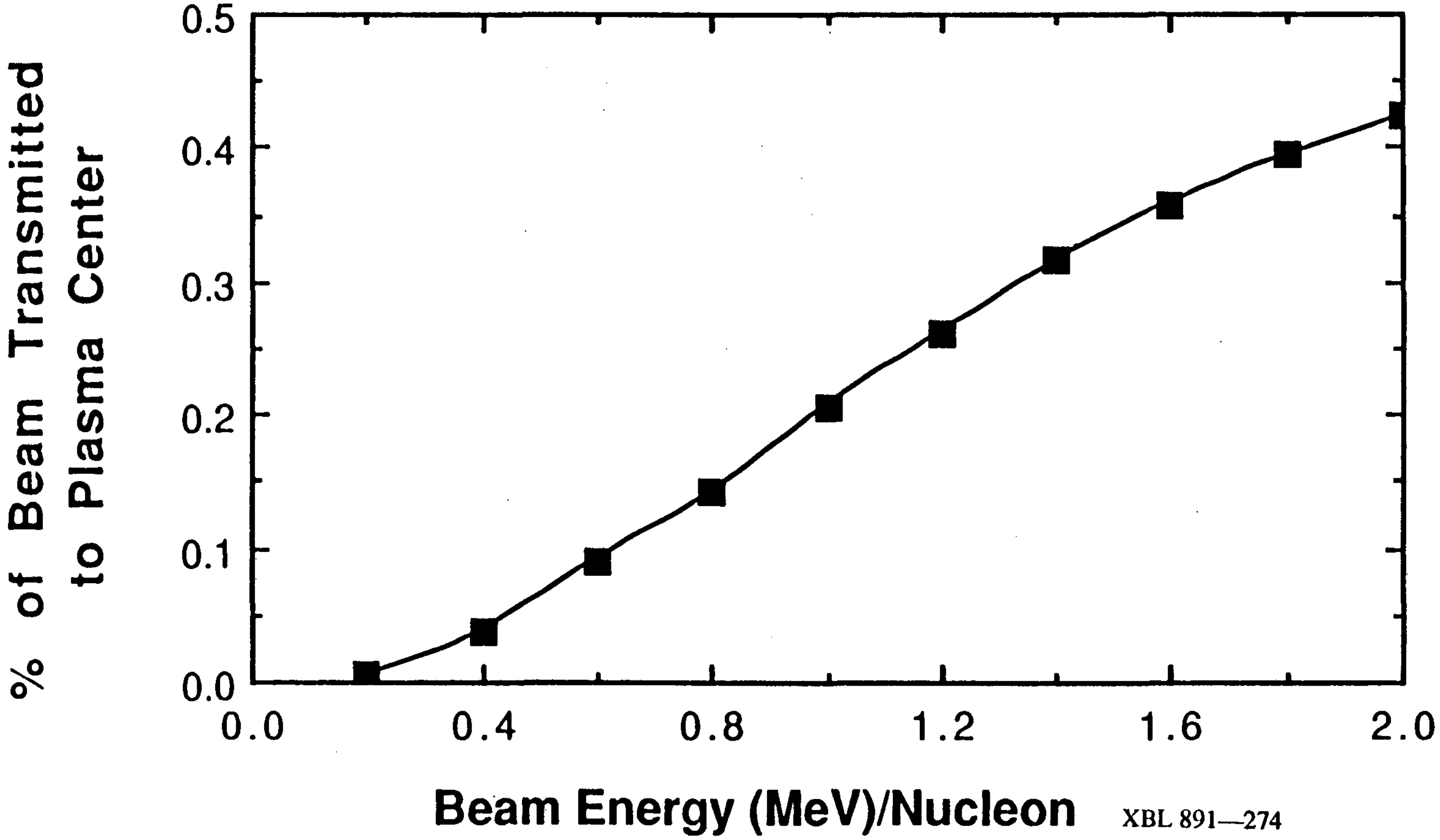

XBL 891—274

Fig. 4-2 Atomic Lithium Beam Penetration into the ITER Plasma as a Function of Beam Energy allows some measurements to be made near the interior boundary ($R = R_0 - a$) of the plasma.

The next consideration for the diagnostic system is to maintain an adequate S/N ratio in an environment of increased CIF and bremsstrahlung radiation. The effect of CIF can be estimated using the parameters of the TEXT diagnostic beam. The CIF signal from ITER will be roughly that found in TEXT multiplied by the ratio of the ion densities, atom velocities, and excitation cross sections. The density ratio is well known ($1.45\text{x}10^{14}$ cm^{-3}/$2\text{x}10^{13}$ cm^{-3}), as is the ratio of atom beam velocities (12 MeV/95 keV)$^{1/2}$. The ratio of the excitation cross sections can be estimated from the ratio of the attenuation cross sections ($4.2\text{x}10^{-17}$ cm^2/$2.5\text{x}10^{-15}$ cm^2). This gives an ITER CIF signal that is ~1.4 times that of the TEXT system. The LIF signal for the ITER diagnostic must be increased to compensate, which can be achieved by boosting the laser flux. This can be done by increasing the laser power and reducing the beam diameter. Increasing the ^{6}Li° beam flux would increase both the LIF and the CIF noise background.

The bremsstrahlung noise from a tokamak plasma is proportional to ($n_e^2T_e^{1/2}$).[62] Given the parameters for TEXT ($2\text{x}10^{13}$ cm^{-3}, ~1 keV), and ITER ($1.45\text{x}10^{14}$ cm^{-3}, 10 keV), the ratio of ITER/TEXT noise is ~166. This implies that the beam multiplied by the laser flux must be increased by 166 times from the values used on TEXT to maintain the S/N ratio of the TEXT diagnostic system. The CIF and bremsstrahlung noise considerations dictate the minimum laser and atom beam fluxes for a workable ITER diagnostic system.

To summarize the minimum requirements so far, a laser flux 1.4 times that used for the TEXT diagnostic, and an atom beam flux multiplied by a laser flux 166 times that used on TEXT will be necessary to maintain the S/N ratio attained with the TEXT diagnostic. This does not take into account any improvement in noise rejection that can be achieved with modulation of the laser intensity. For further calculations, a factor of ten improvement in laser flux and a factor of twenty improvement in atom beam flux from the values of the TEXT diagnostic will be assumed. This entails a beam flux of 1 mA/1.77 cm^2 (TEXT values) x 20 = 11.3 mA/cm^2. The improved plasma penetration of the ITER diagnostic beam will allow better S/N ratios for measurements made in the interior of the plasma at the proposed energy of 2 MeV/nucleon or 12 MeV for $^6Li^\circ$. The collection optics for the LIF. signal will be unchanged in design from that used on the TEXT system.

Once the minimum beam parameters for the ITER diagnostic are known, the beamline components can be specified. The beam neutralizer is the first stage back from the tokamak and is tackled first. The neutralization efficiencies for a high energy Li^- beam in both gas and plasma targets has been measured.[63] Photodetachment, while conceptually attractive, does not appear feasible due to the lack of high power cw lasers in the energy range of interest, even assuming that high reflectivity mirrors can be maintained in a lithium environment. The ITER diagnostic will use a plasma neutralizer. Although the demonstrated efficiency (56%) is only marginally better than a gas neutralizer (50%), there is great room for improvement in plasma neutralization using high charge state plasmas.[9] However, the 56% value will be assumed in calculations, resulting in a minimum input current density of 20.2 mA/cm^2.

Stepping back from the neutralizer, the accelerator is the next component of interest. In the MeV range of energies, the radio frequency quadrupole (RFQ) is an attractive accelerator candidate. A preliminary study of a 6 Mev $^6Li^-$ beam accelerator showed the feasibility of this concept for the $^6Li^\circ$ beam diagnostic.[64] Scaling this to a 2 MeV/nucleon system would simply require a longer accelerator, which can be compensated for by increasing the field gradient. However, by using the published parameters with the longer accelerator to give 2 MeV/nucleon, a conservative design can be implemented. This accelerator would accept ~93% of a 1.4 mA/cm^2 Li$^-$ beam which is focused to ~sixteen times the initial current density (20.5 mA/cm^2) and accelerated to 12 MeV over a length of approximately 14 m.[2] The accelerator is capable a handling up to 100 mA of Li$^-$.

These considerations lead to the ion source. A Li$^-$ current density of 1.9 mA/cm^2 has been demonstrated in a low power multicusp ion source.[48] For this application, the ion source size would be increased to create a larger extraction area with a uniform plasma density. This has been outlined in the improved Li$^-$ source of the last chapter. Although the Li$^-$ current density is likely to increase substantially in this larger source, the published value of 1.9 mA/cm^2 will be used. Transparencies of ~85% for multiple hole extraction grids are feasible.[65] In this case, a transparency of 1.4 mA/cm^2/1.9 mA/cm^2 = 74% is needed to meet the requirements of the diagnostic beam.

The last component considered is the laser. A factor of ten improvement in laser flux from that used on TEXT was required. This can be achieved in two ways. First, the beam diameter for both the laser and atom beam will be reduced to 1 cm from 1.5 cm used on TEXT. This increases the laser flux by 2.25 times for the same laser power. Second, the argon ion pump laser will be increased in power by a factor of ~five. The TEXT system uses a 4 W pump laser, but lasers of up to 40 W are commercially available for this purpose. Hence, scaling the laser flux by a factor of ten or more appears straightforward.

The parameters of the ^{6}Li° ITER diagnostic system are now specified. Laser power of 5.6 W in a beam of 1 cm diameter results in a factor of ~eleven improvement versus the TEXT system. The ion source will generate a Li$^-$ current density of 1.9 mA/cm^2. This current passes through an extraction grid of 74% transparency resulting in 1.4 mA/cm^2. Beam size at the ion source will be 4 cm diameter. Beam current is 17.6 mA versus ~2.5 mA for the TEXT Li$^+$ ion source. The accelerator will focus and accelerate ~93% of this beam to 12 MeV over a length of 14 m. The output beam will have a 1 cm diameter, a current of 16.4 mA, and a current density of 20.8 mA/cm^2. A plasma neutralizer converts 56% of the ^{6}Li$^-$ ions into ^{6}Li°. Therefore, the atom beam entering the tokamak will have an equivalent current of 9.2 mA in a 1 cm diameter. This represents a factor of 20.7 increase in beam flux versus the TEXT system. Overall, a factor of 233 increase in LIF signal versus TEXT should be achieved at the plasma edge. With the increase in bremsstrahlung noise in the ITER plasma, the overall increase in S/N ratio will be 233/166 = 1.40 or 40%. At the plasma center, the improvement increases to 1.4 x 0.42/0.26 = 2.27, and at the far edge to 1.4 x 0.18/0.067 = 3.76 due to the better penetration of the ITER beam versus the TEXT beam. Hence the S/N ratio of the ITER diagnostic system is expected to be somewhat better than that achieved with the TEXT system.

Conclusion

The feasibility of a confined magnetic pitch angle diagnostic using injected $^6Li^\circ$ and laser beams has been considered. The technology required for this system is largely available now. Assumptions used in scaling devices for this system have been extremely modest. No improvements over experimentally demonstrated parameters were assumed for the ion source or neutralizer, although their size would be increased. The RFQ accelerator has been implemented for protons[66] and extension to lithium appears feasible.[64] The required laser system has been demonstrated on TEXT. An increase in pump laser power has been assumed, but there appear to be no difficulties in scaling the dye laser output with the pump power.

In any case, there is a substantial margin of safety in the S/N ratio when compared to that achieved with the TEXT diagnostic. This S/N ratio is expected to be improved upon when the LIF signal is detected at the modulation frequency of the dye laser, the available Li^- current density is increased by increasing the plasma density in the ion source, and the plasma neutralizer utilizes a high charge state plasma. Drawbacks in this analysis include neglecting the effect of stripping of Li^- in the accelerator. This problem is not expected to be great, due to the gas restriction of the multiple small hole ion extraction grids and the lithium pumping effect of all of the colder wall surfaces.

Tokamak operation with the lithium beam injection should not be affected. The injected current is small (9.2 mA) so any increase in impurities (Z_{eff} and radiation) will be negligible. Some (18%) of the $^6Li^\circ$ beam will pass completely through the plasma. At 12 MeV of energy, this will represent a wall loading of about 25 kW/cm^2 over an area of ~0.8 cm^2. This is comparable to the peak wall load expected during normal tokamak operation. Hence the heat load is not critical, but may require a modification of the wall surface over the small beam impact area.

The measurement of magnetic pitch angle on the conceptual ITER tokamak appears to be scientifically feasible using an injected atom beam and coincident laser beam in a manner demonstrated on the TEXT device. Although the beam velocity required is large, present negative ion source, accelerator, and neutralizer technology is sufficient to meet this goal. Development is required to scale some components to the appropriate size, and to scale the dye laser output with the increased available pump laser power. It is recommended that further studies consider the economics and engineering of this diagnostic system to evaluate its true potential as a diagnostic tool.

Chapter 5 Production of H^- Ions in a Cesium or Xenon-Seeded Hydrogen Discharge

The development of high energy H^- ion beams is of great interest for fusion and other applications. Progress towards this goal depends on improving the current density of H^- ion sources. Further improvements in volume generated H^- ion sources are being achieved by increasing the plasma density.[67] However, limitations in steady state cathode operation and gas flow place an upper bound on plasma density. Therefore, an alternative way of enhancing H^- ion production is needed. This chapter investigates the effect on H^- production of cesium or xenon impurity seeding of a hydrogen discharge.

Previous work on cesiated H^- ion sources has been concentrated on surface production type ion sources,[21] but some recent work has been done on "cesiated" volume produced H^- ion sources.[68,69,70] These results, showing large increases in H^- output, imply that other source geometries may also provide enhanced H^- output with the addition of cesium. The effect of cesium on the H^- ion yield in the filtered multicusp source has not been carefully studied. The experimental results detailed in this chapter demonstrate that a substantial gain in H^- output can be achieved with the addition of cesium.

Mixing xenon with hydrogen in a filtered multicusp source discharge has been tested previously.[71] The reason for including xenon addition in this work is to compare xenon addition to cesium addition for the same ion source and filter geometry. Both species have large masses and consequently large ion gyroradii, large ionization cross sections, and lower thresholds for ionization relative to H_2. Differences in H^- output when either cesium or xenon are added may explain the function of cesium in volume H^- ion sources.

Part I Experiments with a Small Ion Source

Experimental Apparatus

The 1-inch multicusp ion source is fabricated from a cylindrical water cooled copper chamber (2.5 cm diameter by 5 cm long) with the open end enclosed by a two-grid ion extraction system.[72] This source is essentially identical to that used for the Li^- experiments of chapter 3, except that the liner used for the cesium-seeded discharges is somewhat different than that used for lithium. In the case of xenon-seeded hydrogen discharges, no liner is used at all. An extraction aperture of 1.6 mm (0.8 mm) in diameter, giving an extraction area of 2×10^{-2} cm^2 (5×10^{-3} cm^2), is used for the cesium (xenon) addition experiments. The plasma electrode can be biased independently of the anode to optimize H^- ion extraction. This electrode is also operated at high temperature to prevent condensation of cesium.

Experimental Results - Source Operation with Hydrogen and Cesium

For source operation with cesium vapor, an oven containing metallic cesium is connected to the ion source via a valve as shown schematically in Fig. 5-1. Initially, the oven is heated to 400°C

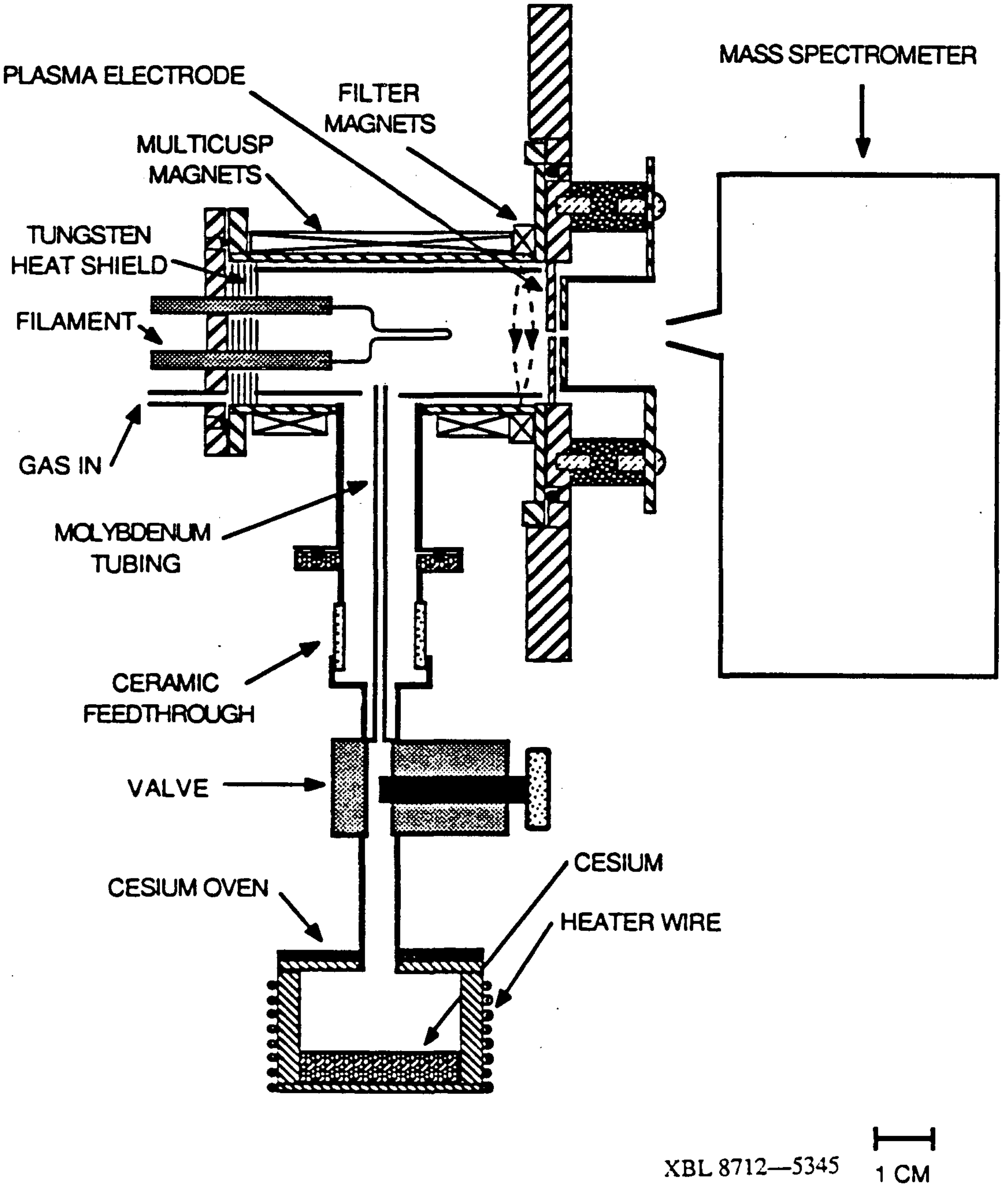

Fig 5-1 A Schematic Diagram of the Small Ion Source

with the valve closed to decompose an oxide layer that may form on the surface of the cesium during loading of the oven. The oven is then cooled to below 150°C and the valve is opened. During this time and throughout the experiment, heater tapes maintain the temperature of the valve and transport tubing at ~300°C to minimize cesium condensation. The oven is then heated to temperatures greater than 150°C to drive cesium from the oven into the discharge chamber.

The ion source was first operated dc without cesium to determine source performance when only hydrogen gas is used. The mass spectrometer was used to measure the positive ion species distribution and the H^- signal level. Figure 5-2(a) shows the positive ion species in the extracted beam for an arc voltage of 80 V and an arc current of 2 A. It can be seen that H_3^+ is the dominant positive ion species in the beam, with the distribution being 5% H^+, 12% H_2^+, and 83% H_3^+. The negative ion spectrometer signal is shown in Fig. 5-3(a). In this case, H^- ions are the main negative ion species in the discharge, and no other negative ion species was detected. Although the neutral gas density in the discharge was not measured directly, it can be estimated from the gas flow rate, liner or wall temperature (~400°C), and the extraction area. This gives a source pressure of the order of 130 mTorr.

Cesium was introduced to the discharge by opening the valve to the cesium oven. The H^- output signal was monitored while maintaining the same discharge parameters. Fig. 5-4 shows the H^- output signal as a function of the oven temperature. With the oven temperature adjusted at or below 150°C, no significant change in

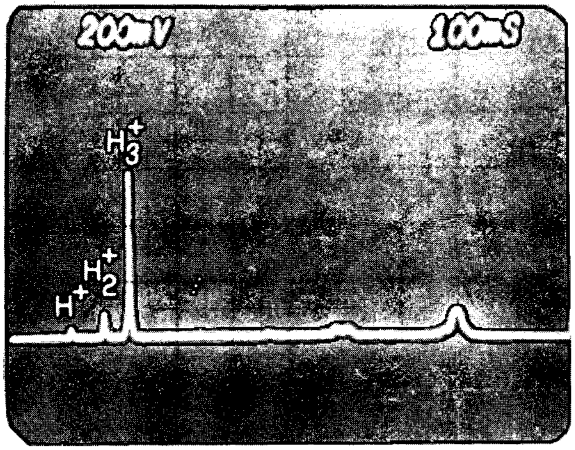

(a)

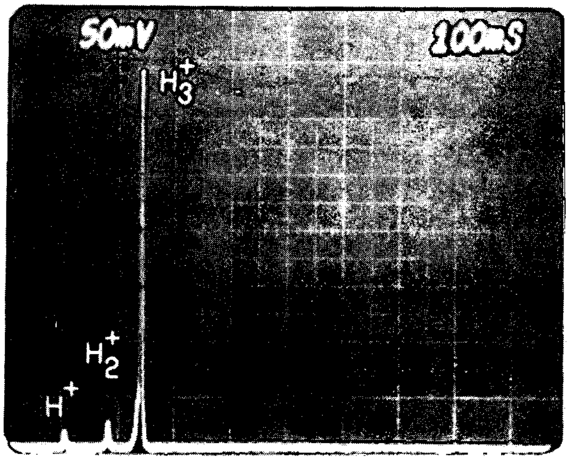

(b)

Fig. 5-2 Mass Spectrometer Traces of (a) the Positive Ion Species in a Pure Hydrogen Discharge, (b) with Cesium Added, and (c) at Low Extraction Voltage with Cesium Added

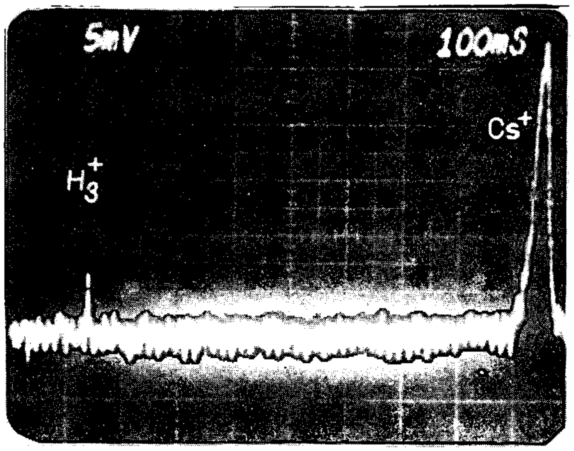

(c)

XBB 870-10664

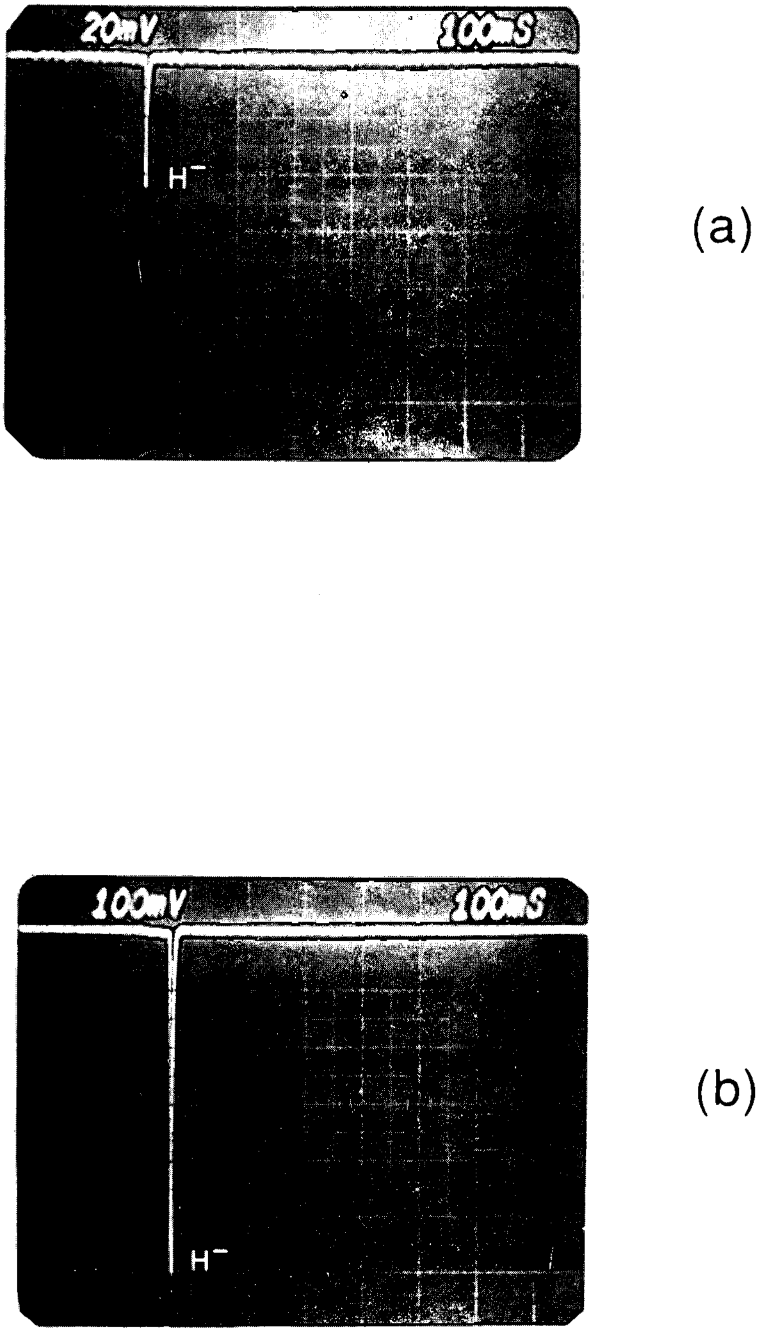

XBB 870—10662

Fig. 5-3 Mass Spectrometer Traces of (a) the Negative Ion Species in a Pure Hydrogen Discharge, (b) with Cesium Added

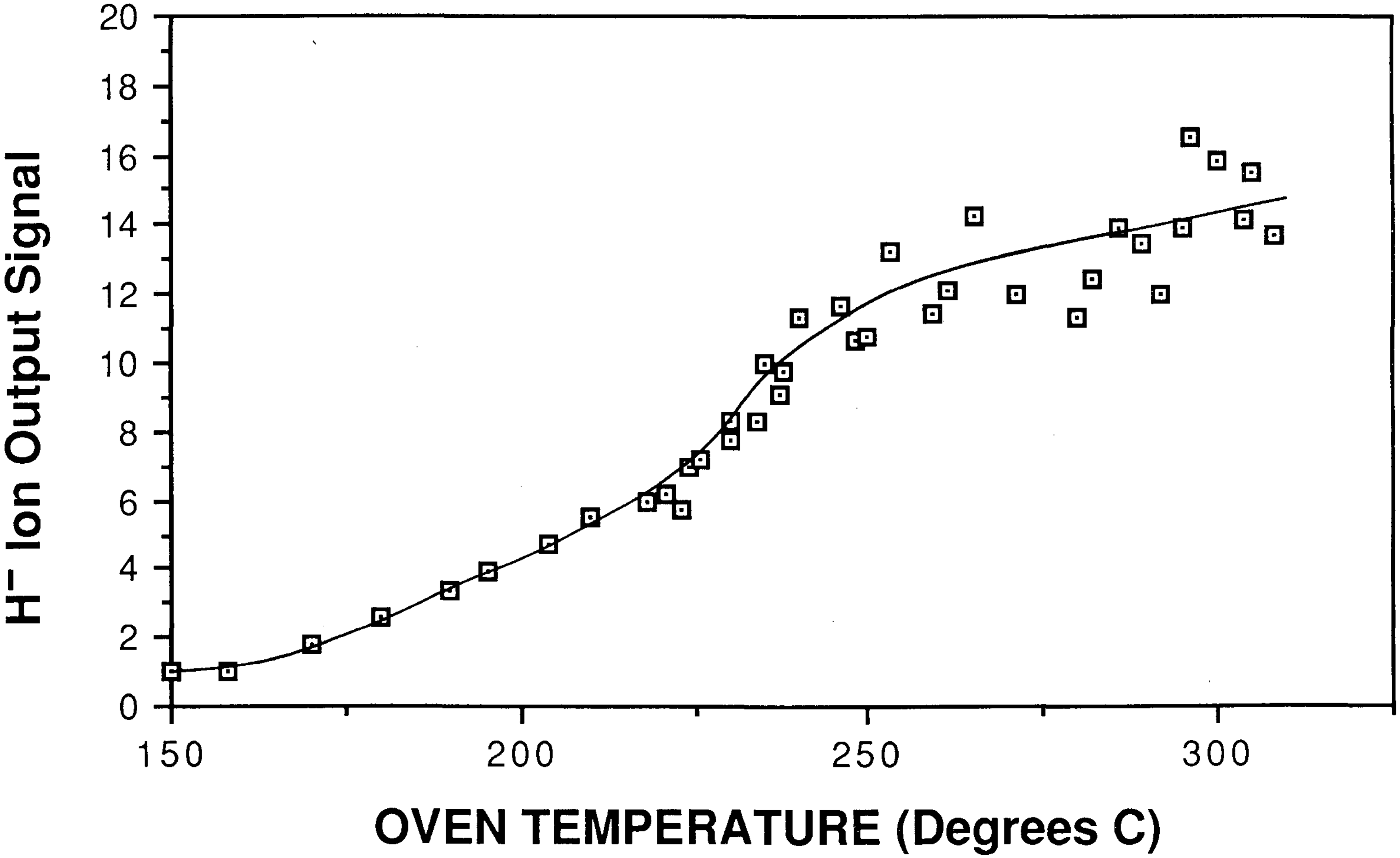

XBL 882-594

Fig. 5-4 A Graph of the H^- Output Signal as a Function of the Cesium Oven Temperature the H^- ion signal is observed. As the oven temperature exceeds 170°C, the H^- signal increases steadily with temperature until a plateau is reached at ~300°C. The maximum enhancement of the H^- signal with cesium is over sixteen times that for operation with pure hydrogen.

To verify that cesium was indeed in the plasma, a positive ion beam was extracted from the source and Fig. 5-2(b) and (c) illustrate the resulting positive ion spectrum. Fig. 5-2(b) shows that the hydrogen ion species distribution changes to 4% H^+, 7% H_2^+, and 89% H_3^+, very similar to operation without cesium but with a slightly higher percentage of H_3^+ ions. Cs^+ ions are not seen in the spectrum of Fig. 5-2(b) because they are too massive to be collected at this extraction voltage (187V). When the extraction voltage is lowered to 35V (Fig. 5-2(c)), the spectrum shows the presence of the Cs^+ ion peak, along with H_3^+ ions. Indeed, cesium ions are the dominant positive ion species in the discharge because cesium has a much larger ionization cross section, and a low threshold ionization energy (3.9eV). Because of its large mass, Cs^+ ions have a larger ion gyroradius than H_3^+ ions. Thus they can penetrate the magnetic filter much more easily. Fig. 5-3(b) shows the spectrometer signal for H^- with cesium in the discharge; this signal is much larger than that obtained for pure hydrogen operation (Fig. 5-3(a)). Again, H^- ions are the dominant negative ion species and no Cs^- ions have been detected.

After an hour of operation, the valve to the cesium oven was closed and the source was operated only with residual cesium. After several hours of additional operation, only a slight decrease in H^- output was observed. This indicates that neutral cesium leaves the ion source at a very slow rate, either through condensation at cold spots on the wall or through the extraction aperture. If the cesium is highly ionized, the potential barrier of negative ion extraction can keep the cesium ions from exiting through the extraction aperture. Thus, serious breakdown problems in high voltage accelerating structures can in theory be minimized.

The source has also been operated with no arc voltage present. In this case only the filament was on. The H^- ion signal was still detected with an amplitude comparable to the pure hydrogen discharge case. The filament was driven with a voltage of 5 V and a current of 20 A. Therefore, cesium ionization can still occur either by electron impact or by surface ionization on the filament. However, vibrational excitation of the hydrogen molecule cannot proceed by the usual mechanism of electron impact excitation of an electronically excited state of H_2 which decays into a vibrationally excited state, because the electron energy is too small (< 5 eV). Therefore, the dominant mechanism for vibrational excitation is gone. Recently it was found that vibrationally excited H_2 molecules could be generated by recombination of hydrogen atoms on a surface.[73,74] In this case, hydrogen atoms are produced by dissociation of H_2 on the hot tungsten filament. These atoms can subsequently recombine on the source chamber wall to form vibrationally excited H_2. Although hydrogen atoms are ordinarily deleterious to H^- production, since they have a large cross section for de-exciting vibrationally excited molecules, in this case they can also be the source of vibrationally excited molecules. However, the electron density of this filament driven discharge is extremely small due to the relatively low power dissipated by electron emission and cesium ionization. Therefore, the role of dissociative attachment in H^- ion production is also expected to be small. Hence recombinative desorption is unlikely to explain this result. No H^- ion signal is observed for pure hydrogen operation with the filament only. This is consistent with a surface formation process on the cesiated anode walls.

There are several reasons why the addition of cesium can improve the H^- output of the filtered multicusp source.[75] Cesium has a large ionization cross section at low electron energies relative to H_2. Hence, cesium is efficiently ionized in the discharge, resulting in a much higher plasma density for a given discharge power. This, coupled with its large gryoradius (6.5 cm at 250 gauss and $E = 1$ eV) compared to H_3^+ (1.0 cm at 250 gauss and $E = 1$ eV), will allow the cesium ions and low energy electrons to diffuse much more easily across the filter field and gives a much higher plasma density in the extraction region of the ion source. The presence of a large concentration of low energy electrons in the extraction region in turn, can greatly improve the conversion of vibrationally excited H_2 into H^- ions.

Since a molybdenum surface partially covered by cesium has a very low work function, the impact of positive ions or absorption of ultraviolet radiation may cause emission of additional electrons with energies in the range of 1 eV. In addition, cesium atoms may cool the electrons in the extraction region through inelastic collisions at low energy (1 - 10 eV). There is also a reaction between cesium atoms and H_3^+ ions to give vibrationally excited H_2:

$$Cs + H_3^+ \rightarrow Cs^+ + H_2\,(v^*) + H, \qquad (5\text{-}1a)$$

$$Cs + H_3^+ \rightarrow Cs^+ + 3H\ . \qquad (5\text{-}1b)$$

The cross section and branching ratio for the above reactions are known at higher energies (> 15 eV),[74] but not at the lower energies of interest (0-5 eV). For energies of 15-1000 eV, the cross-section for 5-1(a) is greater than 10^{-14} (cm^2).[74] Nevertheless, this reaction may also contribute to the increase in H^- output by providing more vibrationally excited molecules. Finally, it is also possible that the discharge chamber walls are not hot enough to prevent adsorption of a monolayer of cesium and thus can add H^- ions produced by surface conversion of H^+ ions, or desorption of H^- ions

Experimental Results - Source Operation with Hydrogen and Xenon

Source operation with hydrogen and xenon was investigated at a variety of hydrogen and xenon partial pressures. Fig. 5-5 shows the results of adding xenon to a hydrogen discharge at different hydrogen pressures. Here, the H^- output signal is plotted as a function of the ionization gauge reading obtained downstream from the ion source. For each point, the plasma electrode bias voltage was adjusted to provide the optimum H^- output. The curve marked by open squares denotes operation with hydrogen only. For

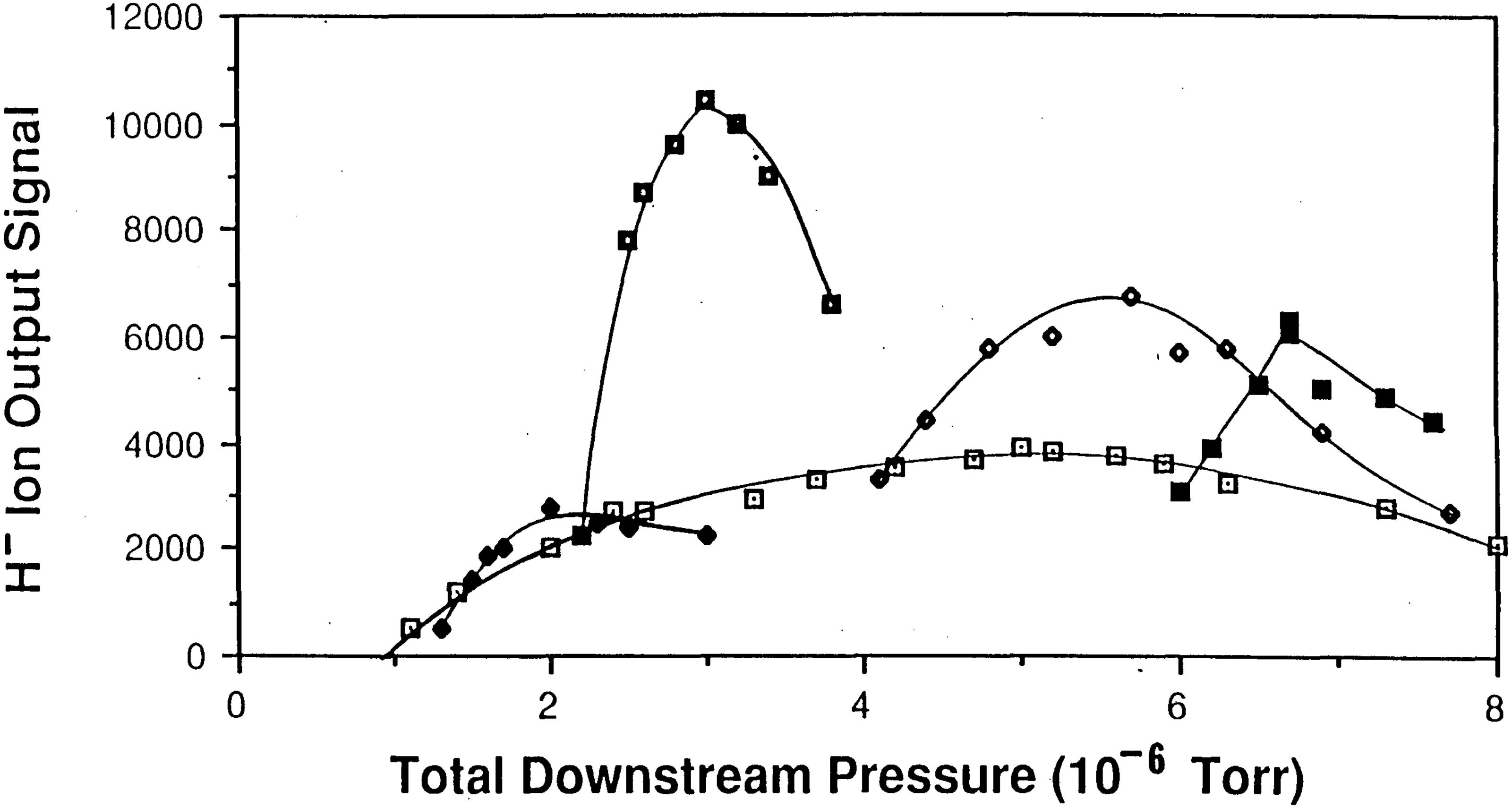

XBL 882-595

Fig. 5-5 A Graph of the H⁻ Output Signal as a Function of Hydrogen and Xenon Partial Pressures the other curves, the first point represents pure hydrogen operation, with higher pressures the result of adding xenon only. Since the ionization gauge is ~6.5 times as sensitive to xenon as to hydrogen, the real increase in downstream pressure due to xenon to achieve the best H^- output is only about 6% over the starting pressure (2.2×10^{-6} torr). The estimated pressure inside the source is about 11 mTorr of hydrogen and 1.8 mTorr of xenon. The best H^- output for hydrogen only is achieved at about 5×10^{-6} torr. In this case, the source pressure is estimated to be about 25 mTorr of hydrogen.

In order to verify the increase in H^- output recorded by the spectrometer, a Faraday cup was used to measure the total extracted negative ion current. The electrons in the beam were removed by a permanent magnet mass separator. Fig. 5-6 shows the H^- output versus pressure for both the spectrometer and the Faraday cup signal. There is very good agreement between the two except at the highest pressures. This may be due to the increase in stripping of the H^- ions inside the spectrometer.

The positive and negative ion species in the extracted beam were measured by the spectrometer for operation with and without xenon. Fig. 5-7(a) shows the positive ion species of the pure hydrogen discharge (6% H^+, 11% H_2^+, 83% H_3^+). When xenon is added to the discharge, the hydrogen species mix changes to 50% H^+, 12% H_2^+, and 38% H_3^+ (Fig. 5-7(b)). This spectrum is very different than that of Fig. 5-2(b) for cesium-hydrogen operation. The addition of xenon shifts the species mix to give a much larger percentage of protons in the beam.

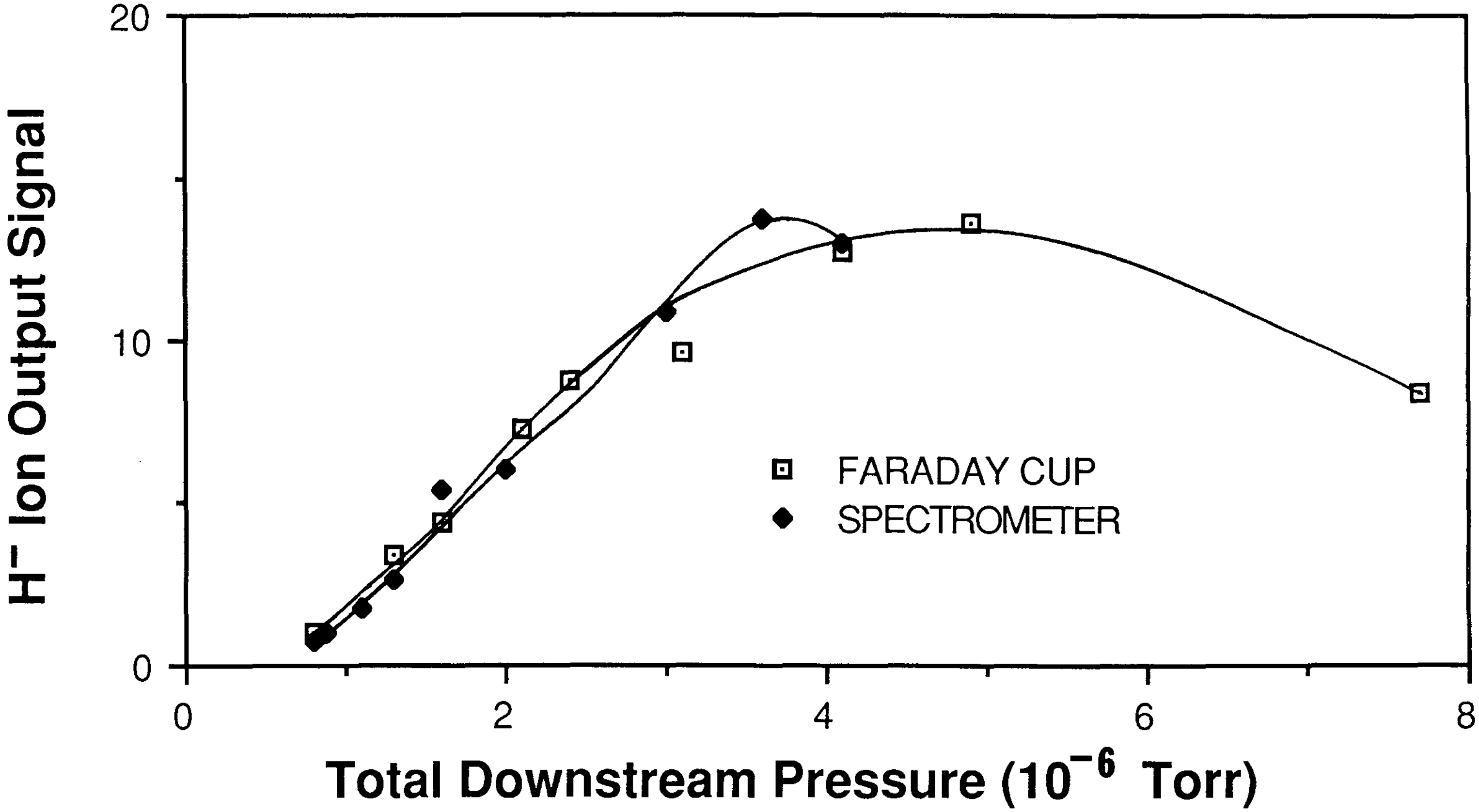

XBL 882-596

Fig. 5-6 A Graph of the H^- Output Measured by the Mass Spectrometer and the Faraday Cup as a Function of the Hydrogen Pressure

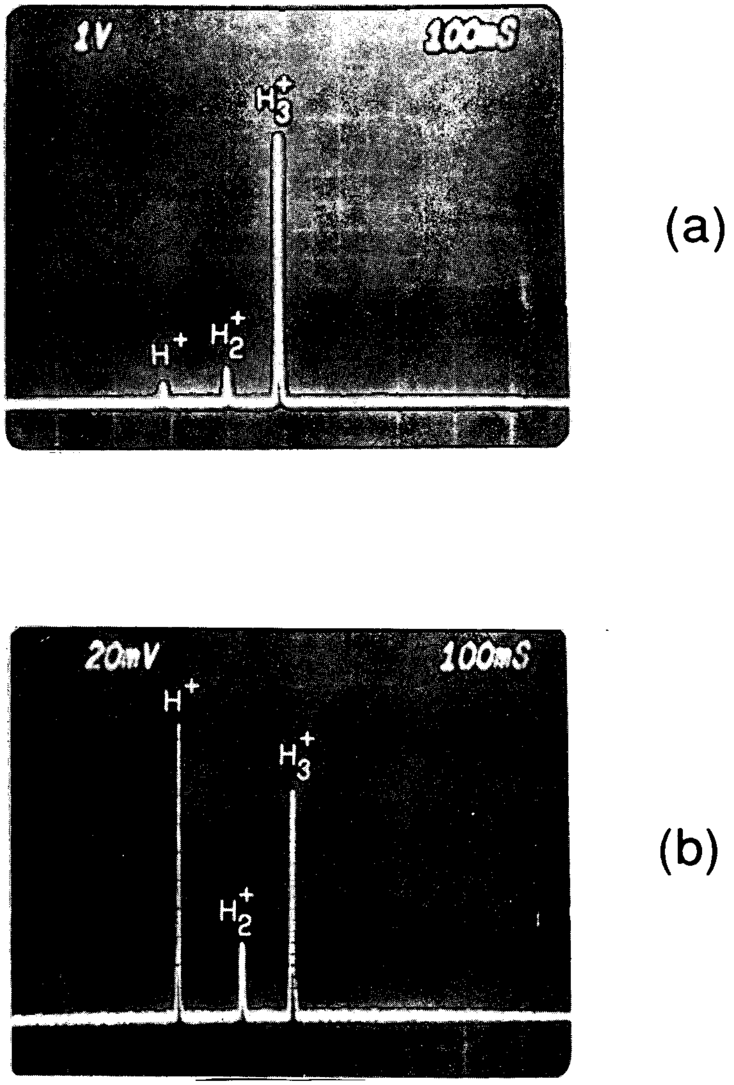

Fig. 5-7 Mass Spectrometer Traces of (a) the Positive Ion Species in a Pure Hydrogen Discharge, (b) with Xenon Added, and (c) at Low Extraction Voltage with Xenon Added

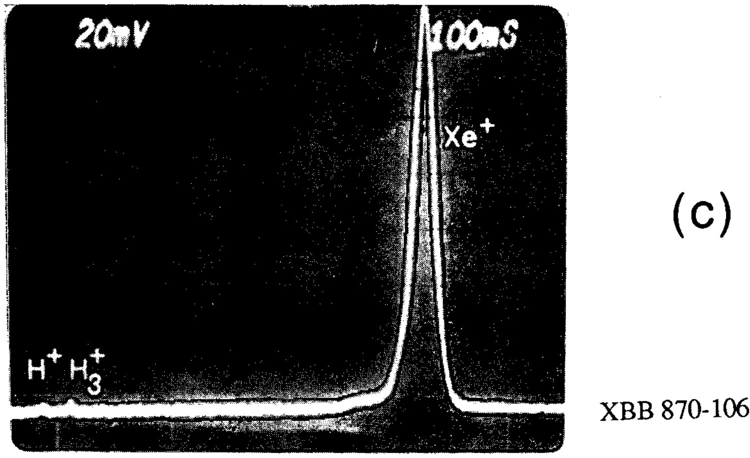

XBB 870-10665

To verify the presence of Xe^+ ions, the extraction voltage was lowered to 35 V to allow Xe^+ ions to be collected by the spectrometer. Fig. 5-7(c) demonstrates that the Xe^+ ion is the dominant species, with H^+ and H_3^+ ion peaks also visible. Fig. 5-8 shows the spectrometer output signal for negative ion extraction, with Fig. 5-8(a) obtained for operation with hydrogen only, and Fig. 5-8(b) for xenon-hydrogen operation. For the case of a xenon-hydrogen discharge, no negative impurity ions were detected.

Discussion

As in the case of cesium, xenon also provides a higher density of low energy electrons to the extraction region of the ion source. This increase in electron density enhances H^- ion production. It should be noted that the peak filter field strength used in these experiments is comparatively strong (B = 250 gauss at the center). While both cesium and xenon addition increase H^- output, cesium provides greater H^- enhancement even though the plasma electrode bias was not optimized in this experiment. There are several reasons why this is the case. Since cesium has a considerably lower ionization energy than xenon, cesium may provide a higher plasma density than xenon in the extraction region of the discharge. Also, cesium may cool the electrons in the extraction region more effectively than xenon. This would reduce H^- losses due to stripping by energetic electrons. Another possibility is the reaction given by equation 5-1(a), whereby H_3^+ ions are converted into vibrationally excited hydrogen molecules. However, more information about the cross section of this reaction in the energy

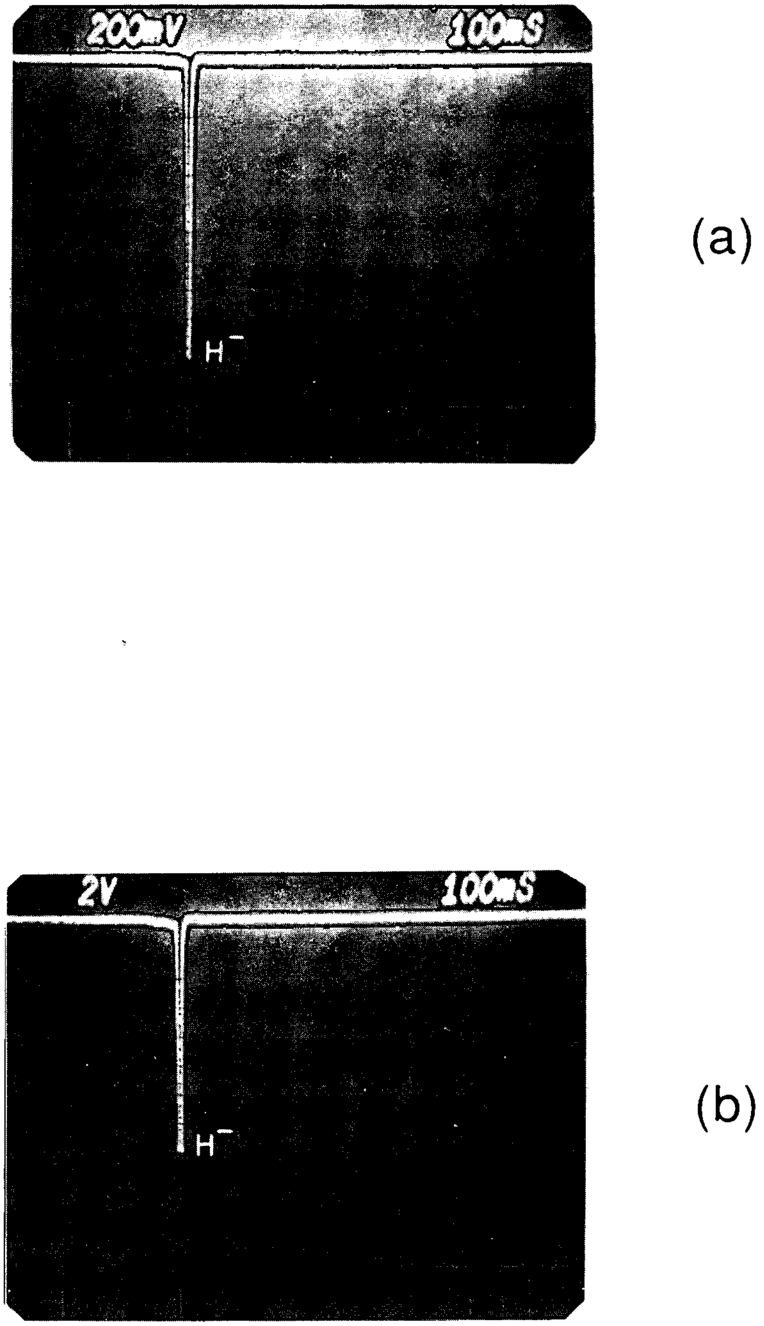

XBB 870-10663

Fig. 5-8 Mass Spectrometer Traces of (a) the Negative Ion Species in a Pure Hydrogen Discharge, (b) with Xenon Added range of interest is needed in order to determine the importance of this process. Additional surface production of H^- ions is also a possibility.

This experiment suggests that addition of cesium to higher power filtered multicusp ion sources may provide much larger H^- current densities than previously attained. Only minor modifications to the ion source are required for cesium operation, and with continuous negative ion extraction, very little cesium will escape from the source.

Part II Experiments with a Larger High Power Ion Source

Recently, a 3-inch multicusp source has been fabricated, and operated in a pulsed mode to generate volume produced H^- ions.[67] From this new source, H^- current densities higher than 250 mA/cm^2 have been extracted. To obtain these current densities, the source requires relatively high gas pressure and high discharge power. Experiments have been conducted to improve the arc and gas efficiencies, the shape of the beam pulse, and the H^- to electron ratio in the extracted beam by optimizing the filter magnetic field, the thickness and axial position of the extraction aperture in the plasma electrode. A recent experimental study, detailed in Part I of this chapter, on a smaller multicusp ion source, in steady state operation and at low discharge power, shows a very large increase in H^- output when cesium vapor is added to a hydrogen discharge.[76] To determine if the increased H^-

output scaled in larger sources operated at high discharge power, this multicusp source was modified to operate with cesium.

H^- current densities in excess of 1 A/cm^2 together with a substantial reduction in the e/H^- ratio were achieved when cesium was introduced into the hydrogen discharge.

Experimental Apparatus

A schematic diagram of the 3-inch multicusp H^- source is shown in Fig. 5-9. The source geometry has already been described in the literature.[67] In brief, the source chamber is a thin-walled (2-mm-thick) copper cylinder (7.5-cm-diam by 8-cm-long) surrounded by 14 columns of samarium-cobalt magnets for primary electron and plasma confinement. The permanent magnets in turn, are enclosed by an outer anodized aluminum cylinder. During pulsed high power discharges, adequate cooling of the magnets is provided by water circulating between the two cylinders.

In order to operate with cesium, a thin molybdenum liner was installed against the inner walls of the source chamber and around the permanent magnet filter rods. Radiation from the tungsten filament and discharge heating by the plasma maintain a high liner temperature. As a result, cesium will not easily condense on the chamber walls. In this experiment, cesium vapor was introduced into the source through a transport pipe from an external oven. The temperatures of the oven and the transfer tubes were regulated by adjusting the heating current of the surrounding coil.

The open end of the source chamber was enclosed by a two-electrode acceleration system. H^- ions were extracted from the

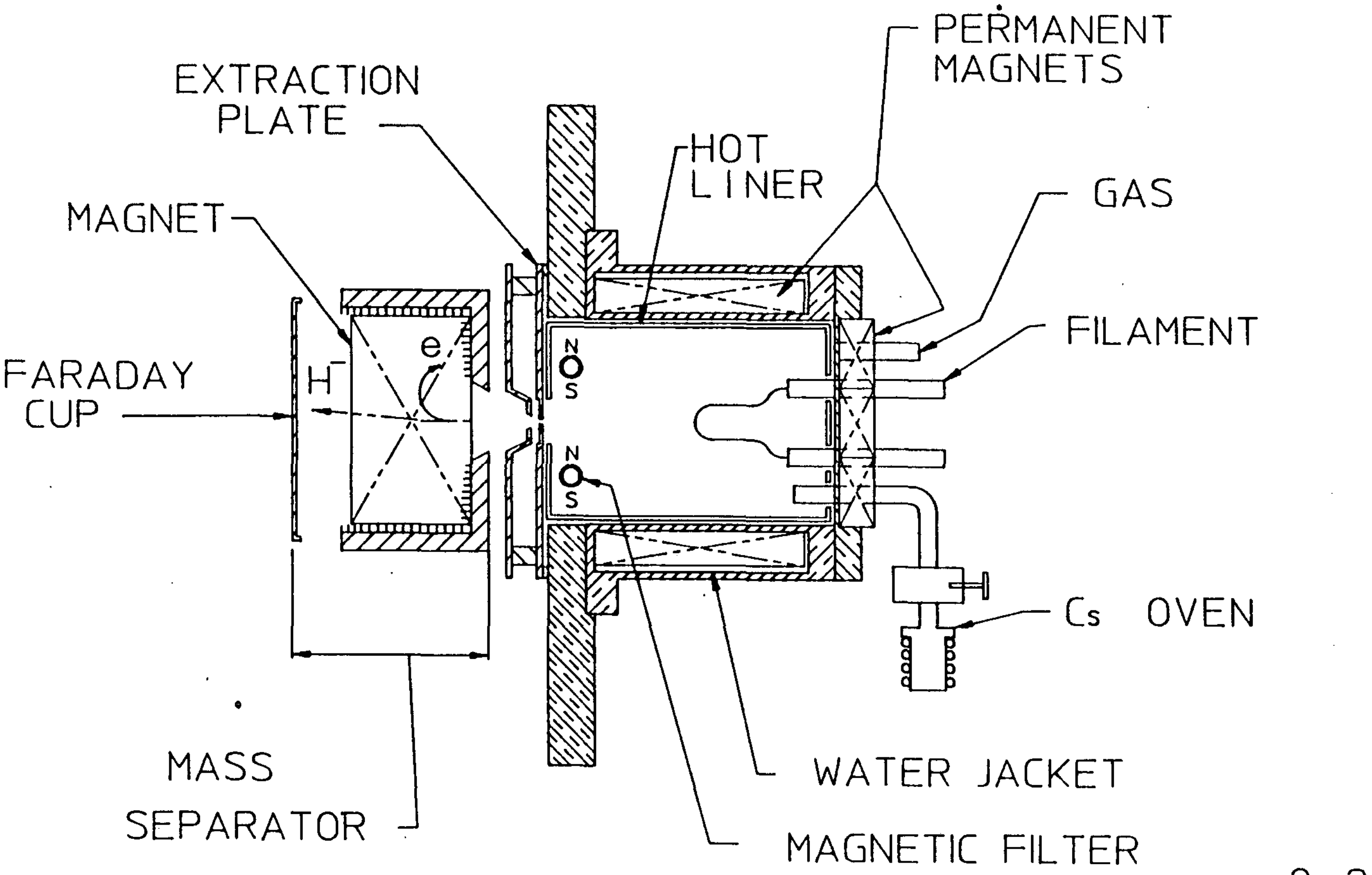

Fig. 5-9 A Schematic Diagram of the Three Inch Multicusp H^- Ion Source

XBL 887—2636

source through one or multiple small apertures. A hydrogen plasma was generated by primary electrons emitted from a cathode located at the center of the source chamber. The entire source chamber, together with the filter rods, served as the anode for the discharge. In this study, the discharge voltage was maintained at ~150 V and the source pressure was varied between 15 to 50 mTorr to achieve the highest H^- yield.

During source operation, the H^- output current was optimized by varying the bias potential of the first (or plasma) electrode with respect to the anode. The maximum extraction voltage used in this experiment was ~16 kV. Electrons in the accelerated beam were separated from the H^- ions by a permanent magnet mass separator (Fig. 5-9). The B-field of the spectrometer was strong enough to deflect the electrons, which were then collected on the grooved graphite plates. The accelerated H^- ions were slightly deflected and were then detected by a graphite Faraday cup which was biased slightly positive relative to ground potential for suppression of secondary electron emission.

Experimental Results for Hydrogen-Cesium Operation

The experiment with the cesium-seeded plasma was first studied with a 1-mm-diam extraction aperture. Figure 5-10 shows the H^- current density obtained from the source as a function of discharge current and the amount of cesium added to the discharge. All measurements were performed at a constant discharge voltage of 150 V and at optimum source hydrogen pressure. When some cesium was added to the source, the H^- current density increased

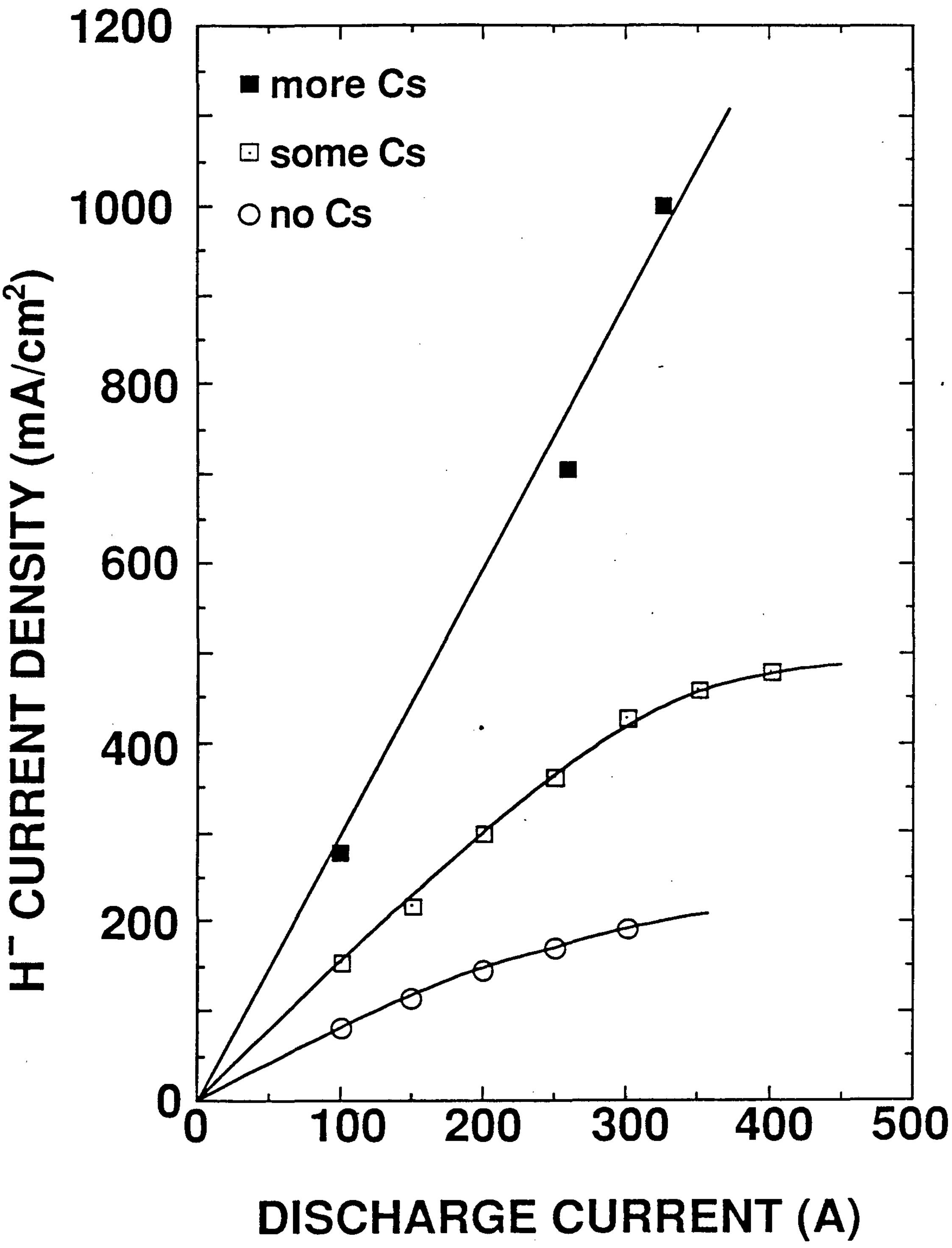

XBL 887—2646

Fig. 5-10 A Graph of the H^- Current Density as a Function of Discharge Current and Cesium Addition (1 mm Aperture) by about a factor of two relative to a pure hydrogen discharge. At this cesium level, no difficulties were encountered during source operation and beam extraction. Further addition of cesium (Fig. 5-10) resulted in an overall improvement of H^- output by a factor of five and H^- current densities exceeding 1 A/cm^2 were obtained. The limiting factor in increasing the cesium density and therefore the H^- output current was electrical breakdown across the extraction electrodes. For a source specifically designed for cesium operation, these problems could be alleviated.

The scaling of H^- ion current as a function of extraction area is of great interest when considering ion sources for accelerator and fusion applications. To address this issue, two additional plasma electrode inserts were fabricated with different extraction areas. One insert contained seven apertures (each of 0.7-mm-diam) inside a 2.26-mm-diam circle and the other contained nineteen apertures (each of 0.9-mm-diam) inside of a 5.0-mm-diam circle. Thus, the nineteen aperture insert has an extraction area of about sixteen times that of the single 1-mm-diam hole.

Figure 5-11 shows the extracted H^- current and current density as a function of discharge current when the seven aperture insert was used. The results are very similar to the single (1-mm-diam) aperture case. At a discharge current of 350 A, source operation with adequate cesium generated a H^- current density of ~1.2 A/cm^2. The corresponding H^- current was 33 mA.

Figure 5-12 is a graph of the e/H^- ratio versus discharge current for the seven aperture insert. Source operation with pure hydrogen produced a high e/H^- ratio that increased with discharge

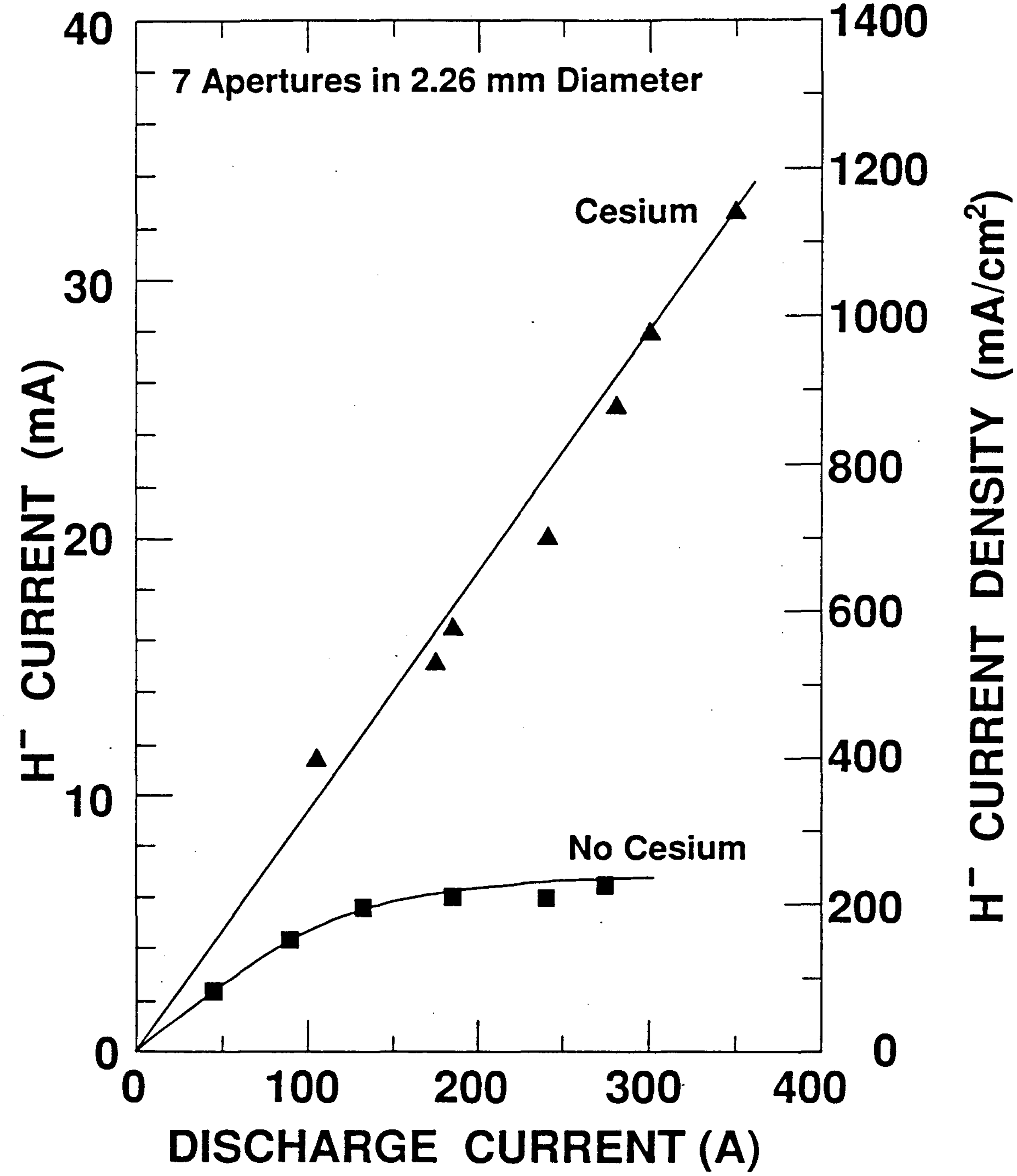

XBL 887-2667

Fig. 5-11 A Graph of the H^- Current Density as a Function of Discharge Current and Cesium Addition

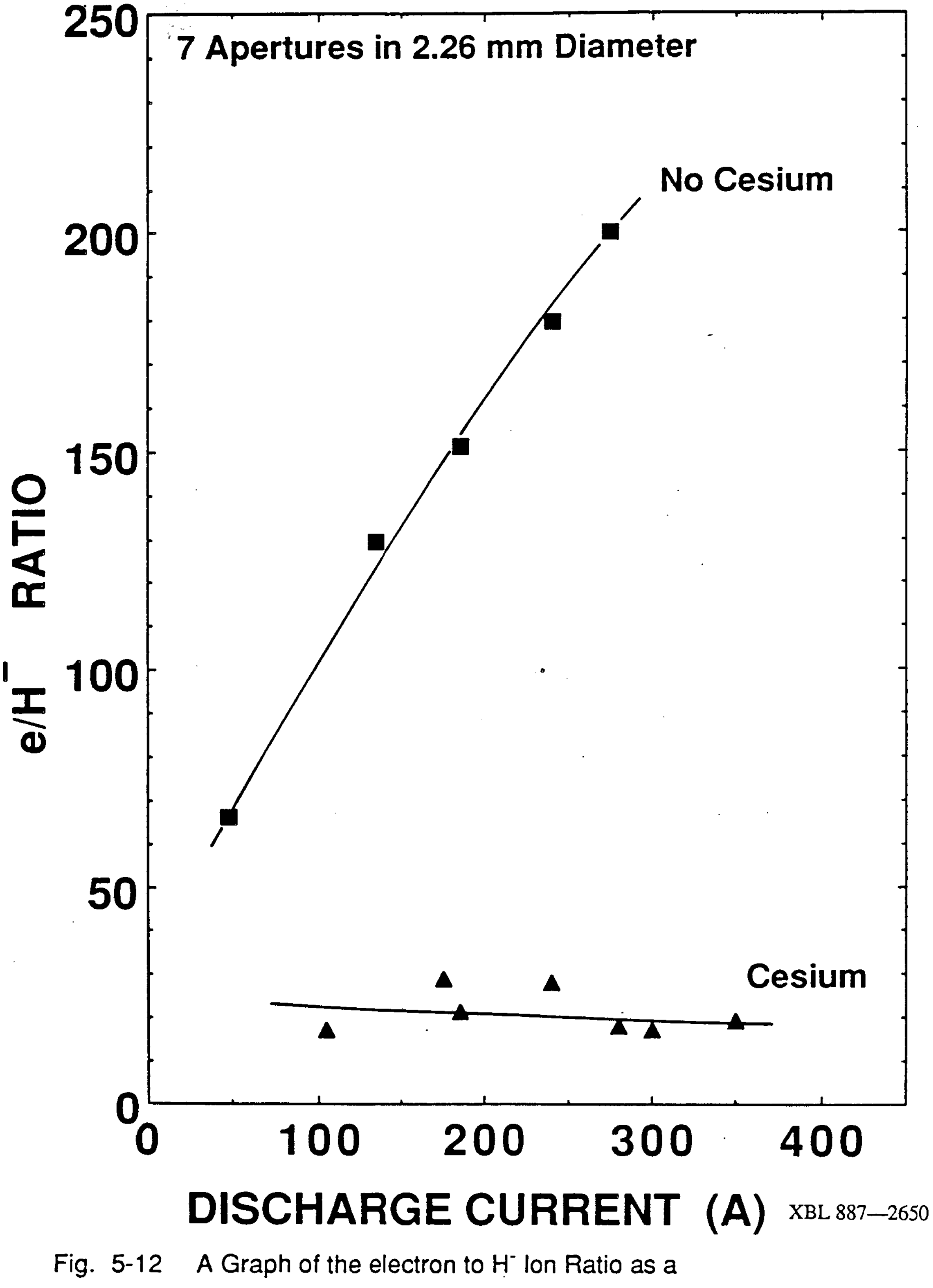

Fig. 5-12 A Graph of the electron to H^- Ion Ratio as a Function of Discharge Current and Cesium Addition

current. Addition of cesium to the discharge, however, reduced the ratio of e/H$^-$ from 200 to 20 at high discharge power. This reduction may be in part due to a decrease in electron temperature in the extraction region.

Source operation with the nineteen aperture insert was very similar to the case of the single or seven aperture insert. In this measurement, the total extracted H$^-$ current is improved to 150 mA at a discharge current of 350 A when cesium is added to the source plasma. The corresponding H$^-$ current density is about 1.2 A/cm^2. The results of these experiments with cesium indicate that the H$^-$ current scales directly with extraction area for the extraction geometries tested.

An oscilloscope picture illustrating the time dependence of the discharge current and voltage, and the extracted electron and H$^-$ currents is shown in Fig. 5-13 for cesium operation with the nineteen aperture insert. During the 500 μs discharge pulse, the H$^-$ current profile is very uniform. This is in contrast to pure hydrogen operation, where the H$^-$ time dependence is peaked early in the pulse. The reason for the improved pulse shape when operating with cesium has not been identified.

The effect of reducing the liner temperature was qualitatively investigated. All discharge parameters were held constant while the pulse repetition rate was reduced. This has the effect of lowering the average power dissipated by the discharge, which reduces the liner temperature. The measured H$^-$ ion current increased for lower liner temperatures. This result implies that cesium is involved with a wall process, since the lower

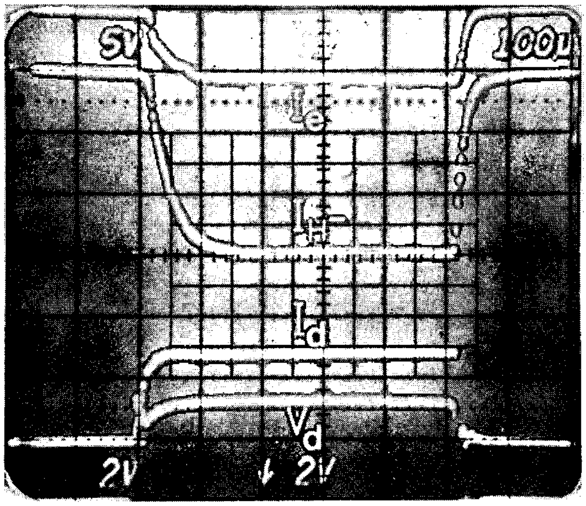

XBB 888—7335

Fig. 5-13 An Oscilloscope Picture Showing the Time Dependence of the Discharge Current and Voltage, and the Extracted Electron and H^- Ion Currents temperature would increase the surface concentration of cesium and lower the cesium partial pressure. Remember that H^- current always increased with the amount of cesium added by the oven. The effect of a further reduction in the pulse repetition rate is limited by the power dissipated by the filament, which is not pulsed.

Part III Conclusion

The results of these experiments show a substantial increase in H^- ion output when cesium is added to a hydrogen discharge. This result scales to high power densities. Although the mechanism for H^- production is not yet known in a cesium-seeded discharge, some possibilities may be inferred from qualitative observations. First, the ratio of H_3^+ to all hydrogen positive ion species in the discharge was relatively uncharged when cesium was added. This would tend to rule out the reaction between H_3^+ and Cs (Eq. 5-1), since the percentage of H_3^+ should be reduced in this case. Second, it was also found that a substantial amount of H^- was produced when no arc voltage was present. This implies a formation process that does not require a substantial electron density. Surface production could explain this result. Third, in the pulsed discharge, the dependence of H^- ion output on the liner temperature provides strong evidence that the H^- enhancement when cesium is added is due to a wall process. Further work is needed to confirm this interpretation.

These results show cesium addition to be an effective way to increase H^- output. Very few modifications were needed to adapt the volume H^- source to operation with cesium. Further increases in H^- current density may be obtained by using a temperature controlled liner in order to optimize this parameter. A new source design, incorporating this liner and a hot ion extraction system, is recommended. The use of a cesiated discharge may provide the key to developing the low pressure (<10 mTorr) high current density D^- sources needed to make fusion current drive viable.

Chapter 6 Production of H^- Ions in a Barium-Seeded Hydrogen Discharge

Previous experiments have shown that addition of cesium to a filtered multicusp ion source can result in large increases in H^- output.[76] H^- current densities exceeding 1 A/cm^2 have been extracted from a multicusp ion source which is seeded with cesium.[77] In order to avoid the problems that are sometimes associated with cesiated ion source operation (like voltage breakdown), a substitute material for cesium with a much lower vapor pressure is desirable. Recent work with barium converters has shown that the H^- conversion efficiency of a barium converter is similar to that of a cesium-on-molybdenum converter.[78,79] In addition, barium has a much lower vapor pressure than cesium as a function of temperature, as shown in Fig. 6-1.[80] This chapter presents experiments on H^- production when the hydrogen plasma in a filtered multicusp ion source is seeded with barium. An attempt is made to determine the dominant H^- formation mechanism.

Part I Experiments with a Small Ion Source

Preliminary experiments were performed in a small ion source identical to that described in chapter 3 for Li^- experiments, except that barium is used in place of lithium. A schematic diagram of the ion source is shown in Fig. 6-2. During source operation, the liner and the plasma electrode, which are thermally

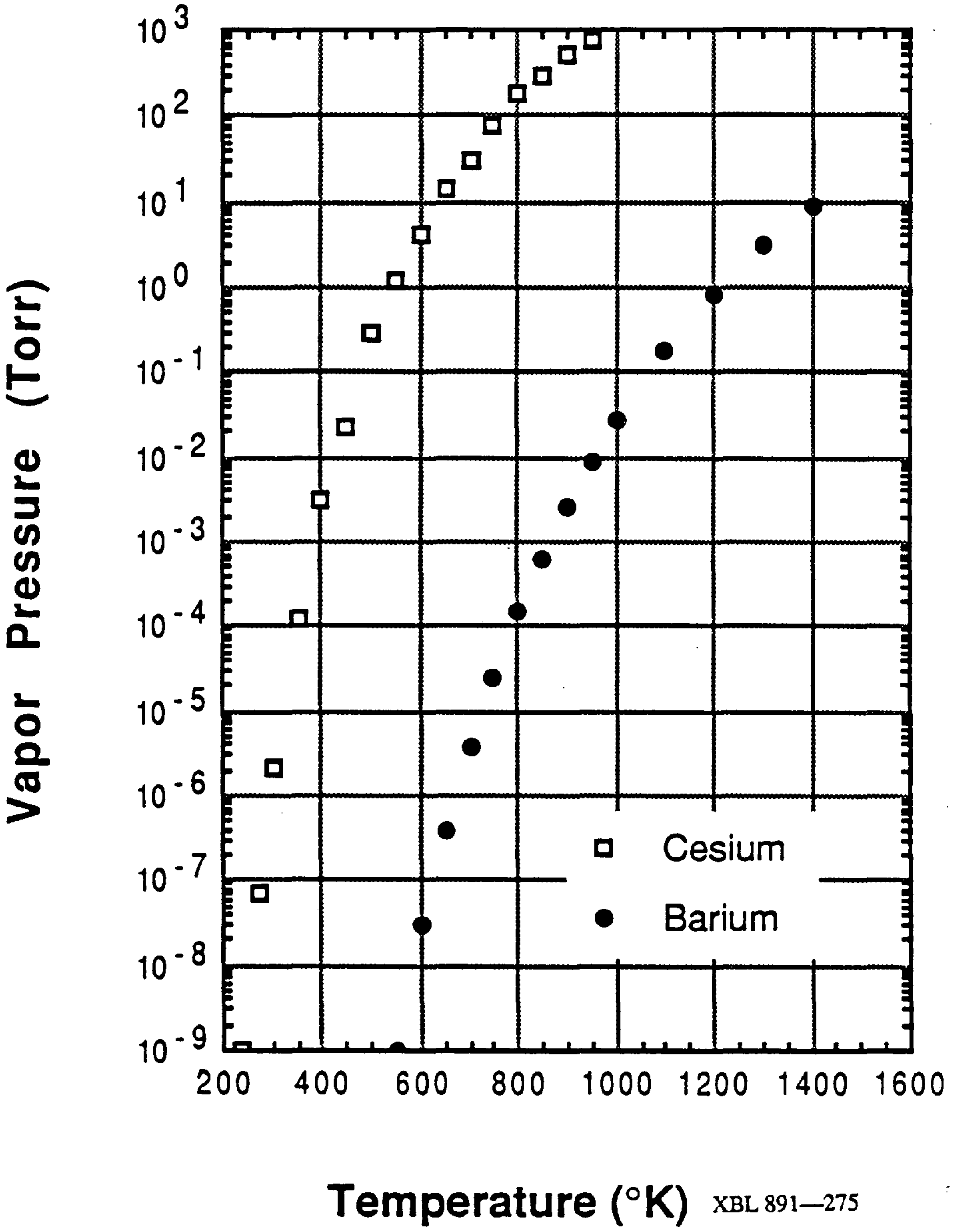

XBL 891—275

Fig. 6-1 A Graph of the Vapor Pressure of Cesium and Barium as a Function of Temperature

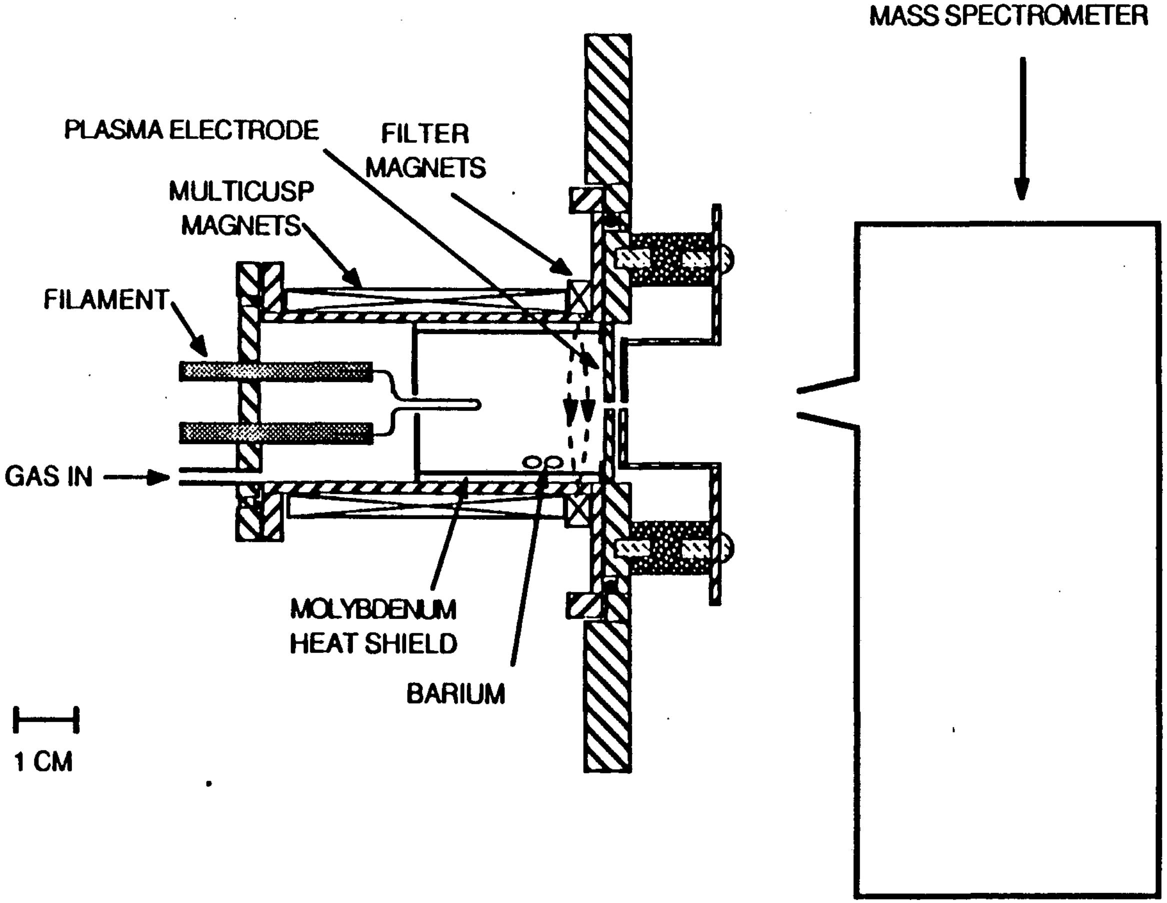

XBL 891—276

Fig. 6-2 A Schematic Diagram of the Small Ion Source Seeded with Barium isolated, are heated by the discharge. The temperature of the liner can be monitored with a thermocouple in contact with the outer surface of the liner. Seeding of the source with barium is accomplished by placing a solid sample of barium metal on the liner. The barium evaporates during source operation due to discharge heating of the liner. In this manner, barium can be deposited on all surfaces of the liner and the plasma electrode.

Located downstream from the second extraction electrode is a compact magnetic deflection spectrometer[53] for measurement of the negative or positive ion species in the extracted beam. For these experiments, the hydrogen pressure in the source is maintained at ~30 mTorr. With the ion source operating steady state at a discharge voltage of 80 V and a discharge current of 0.5 A, the mass spectrometer signal in Fig. 6-3(a) shows the negative ion species for pure hydrogen operation. H^- is the only negative ion detected in the accelerated beam. Fig. 6-3(b) shows the ion species in the extracted positive ion beam for pure hydrogen operation. The dominant ion species is H_3^+, with a smaller fraction of H^+. H_2^+ ions are also present in the discharge, but are not resolvable as a peak for this scale.

The extracted positive ion species for the source seeded with barium are detailed in Fig. 6-3(c). The spectrometer output signal shows the presence of H^+, H_3^+, Ba^{++}, and Ba^+ ions. In this case, the negative ion spectrometer signal detects only H^- ions, but with a much larger amplitude when compared with that in Fig. 6-3(a). In this measurement, both the H^- and the Ba^+ (also Ba^{++}) signals have a strong dependence on the temperature of the liner. Fig. 6-4 is a

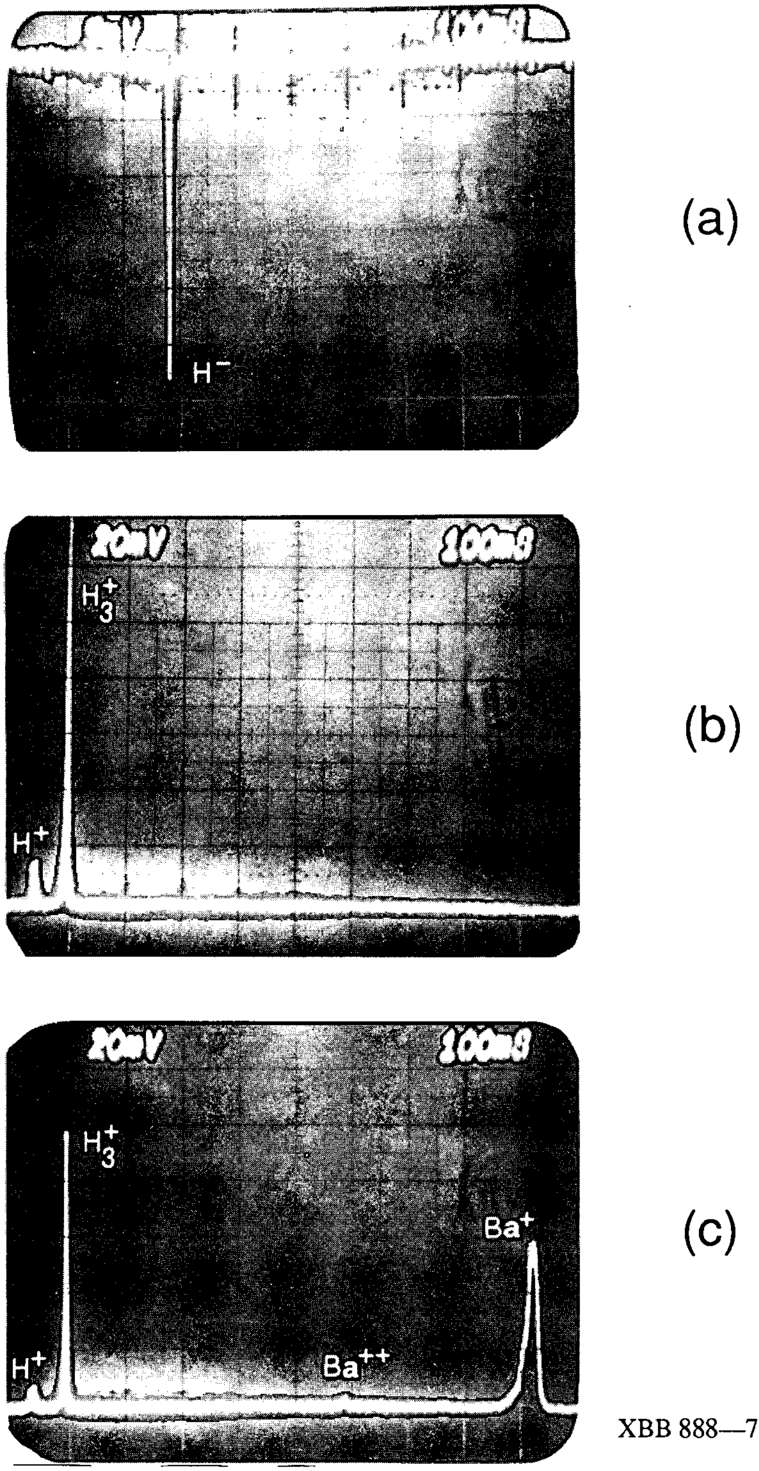

XBB 888—7842

Fig. 6-3 Mass Spectrometer Traces of (a) the Negative Ion Species, (b) the Positive Ion Species for Pure Hydrogen Operation, and (c) the Positive Ion Species for Operation with Barium in the Discharge

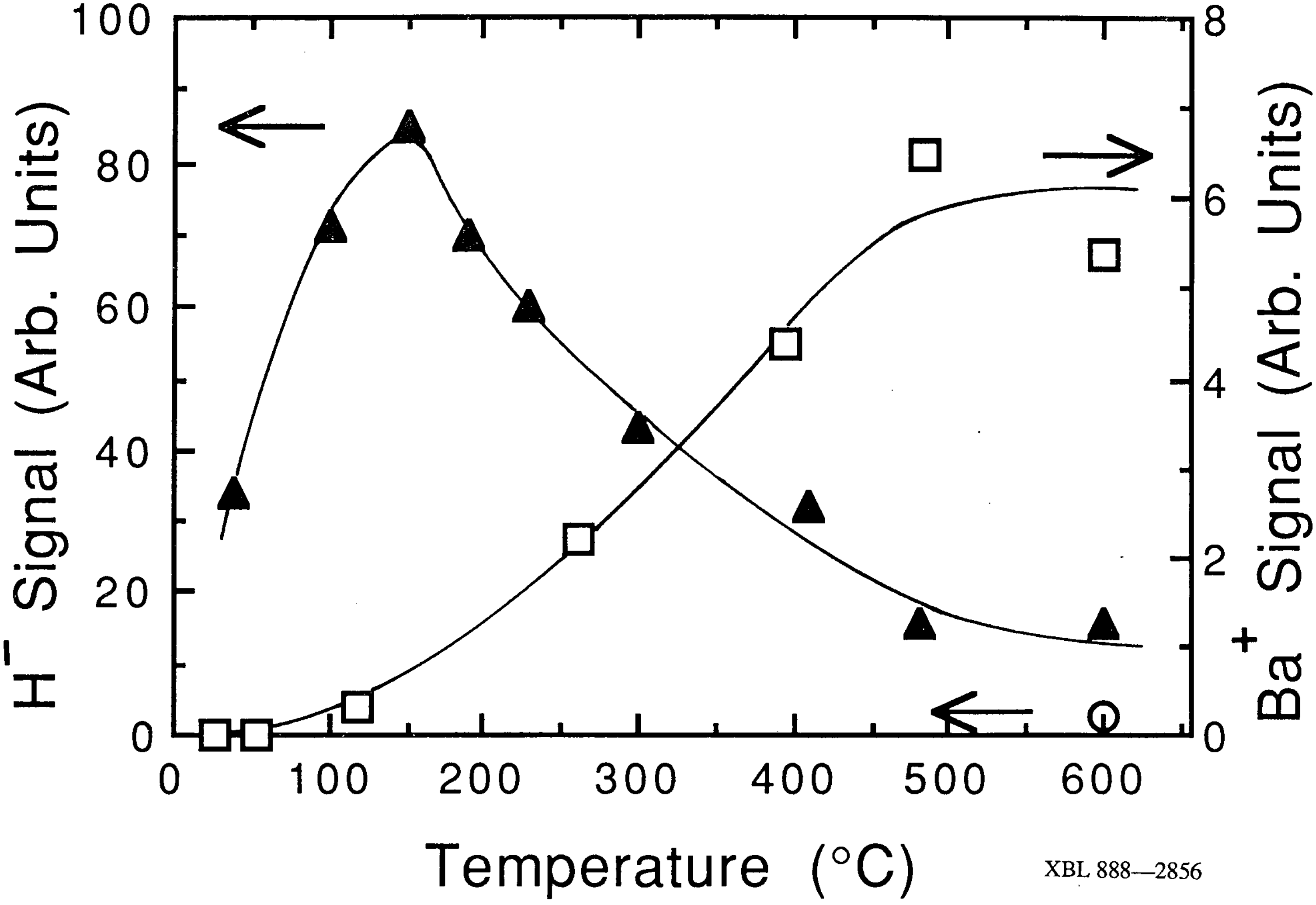

XBL 888—2856

Fig. 6-4 A Graph of the H^- and Ba(+) Ion Signals as a Function of the Temperature of the Liner plot of the H^- and Ba^+ signal amplitude as a function of liner temperature. The baseline value of the H^- signal amplitude for pure hydrogen operation is also displayed in the same figure (O). The maximum H^- output for the barium-seeded discharge is more than thirty times that for pure hydrogen operation. The maximum H^- output occurs for measured liner temperatures of ~150°C. This temperature is reached a short period of time after the discharge was turned on. A much higher liner temperature of ~600°C was obtained for steady state operation. The results of Fig. 6-4 are reproducible when the discharge is turned off, the source wall or liner allowed to cool, and the operating sequence repeated. The liner surface was not changed in any other way, so a barium coating remains after thermal cycling. The liner had an apparent thermal time constant of about a minute.

The dependence of the two signals (H^- and Ba^+ ions) on the liner temperature is very strong. The Ba^+ ion signal behaves predictably, requiring a high liner temperature before barium can be vaporized and enter the plasma. (It should be noted that the dynamic response of the thermocouple used to measure the temperature may be slow because it samples the outside of the liner, not the inside.) The H^- signal is initially ~10 times larger than the baseline value for pure hydrogen operation, and increases rapidly with temperature. At a temperature of ~150°C, the H^- signal reaches a maximum and then decreases for higher liner temperatures. The H^- output starts to decrease when a significant amount of barium is in the plasma. This behavior was reproducible over many thermal cycles. The effect of barium in the plasma on

H^- production is not understood, and these results show that it may reduce the H^- yield. The decrease in H^- output at high liner temperature may also be due to a depletion of barium from the liner surfaces. In all cases, the barium-seeded discharge produced a significantly larger H^- output than the pure hydrogen discharge. It should be noted that the H^- output for pure hydrogen operation is relatively insensitive to liner temperature.

The increase in extracted H^- current, when the discharge is seeded with barium, is very similar to that obtained when the source is seeded with cesium.[76] In that measurement, results showed a factor of ~16 improvement in the H^- output for steady state operation. Steady state operation of the source, with addition of barium and a much hotter liner than that used for cesium, produced approximately a factor of 5 increase in H^- output (see Fig. 6-4). A factor of 30 improvement in H^- output can be achieved at optimum liner temperatures with barium. Further investigation of these results in a larger source, and determination of the H^- production mechanism is the subject of the following section.

Part II Experiments with a Larger Ion Source

Previous experiments show that the H^- yield from a filter-equipped multicusp source can be increased substantially if the hydrogen discharge is seeded with cesium or barium.[77,81] The large enhancement in the H^- output (> a factor of 5) can only be explained if there is a substantial change in the population of vibrationally excited H_2 molecules or positive ion species, which in turn favors the formation of H^- ions via electron-molecule or electron-ion collisional processes,[26,82,83,84] or if surface generation of H^- ions[19] on the chamber walls becomes significant. In this section, the first experimental investigation which identifies the source of H^- formation when the plasma is operated with and without barium is reported.

The experiment was performed in a larger 3-inch diameter multicusp H^- source, which is shown schematically in Fig. 6-5. This is the same source described in Part II of chapter 5, with a few modifications. A steady-state hydrogen plasma was produced by primary electrons emitted from one set of tungsten filaments, and the entire chamber wall served as the anode for the discharge. A second set of tungsten filaments was used to supply additional primary electrons into the source plasma. It has been demonstrated that a negative plasma potential can be formed in a multicusp ion source by the low-energy electron injection technique.[85] If the energies of the injected electrons are lower than the ionization energy of the background gases, then they cannot make ionizing collisions, but they can be confined very efficiently by the multicusp magnetic fields. The presence of a large quantity of these low energy primaries will produce a negative plasma potential well.

Barium, instead of cesium, was employed in this experiment for several reasons. Due to the magnetic field generated by the filament, it is easier to inject primaries with energies below the ionization potential of barium (E_i = 5.2 eV), than primaries with

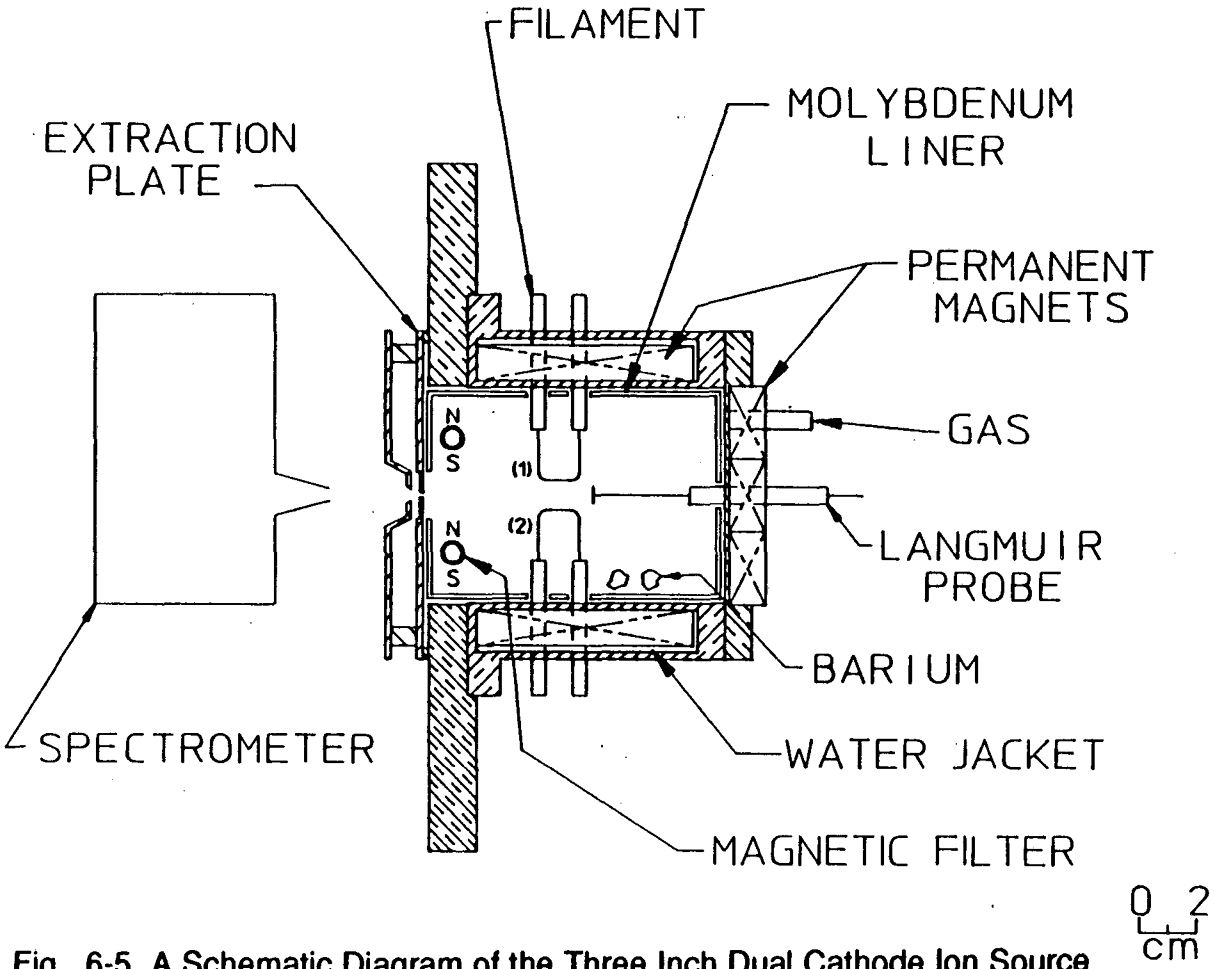

Fig. 6-5 A Schematic Diagram of the Three Inch Dual Cathode Ion Source

XBL 891—277

energies below that of cesium (E_i = 3.9 eV), into the plasma. Secondly, barium has a much lower vapor pressure than cesium, so that much less of its vapor effuses from the source, and voltage-breakdown problems in the accelerator region can be minimized.

Seeding of the source with barium was accomplished by placing some solid samples of barium on the liner. The barium evaporated during discharge operation and deposited on all surfaces of the liner. Negative ions were extracted from the source through a small (0.1 x 1.0 cm^2) aperture. A compact magnetic deflection mass spectrometer,[53] located just outside the extractor, was used for relative measurement of the extracted H^- ions as well as their energy spectrum. Plasma parameters were obtained with a small Langmuir probe located near the center of the source chamber.

The source was initially operated with pure hydrogen at a pressure of 4 mTorr. A background plasma with a density of 2×10^{11} cm^{-3} was maintained by a discharge voltage of 80 V and a discharge current of 0.5 A from filament set (1). Figure 6-6(a) shows the corresponding H^- signal as recorded by the mass spectrometer. The plasma potential V_p measured at the center of the source chamber was about 4 V positive with respect to the anode or chamber walls.

As more and more low-energy electrons were injected from the second set of filaments into the background plasma, Langmuir probe traces showed that the plasma potential V_p became less positive and eventually dropped below the anode potential. It was found that V_p was approximately 3 V negative relative to the anode walls when filament set (2) was operated with a discharge voltage

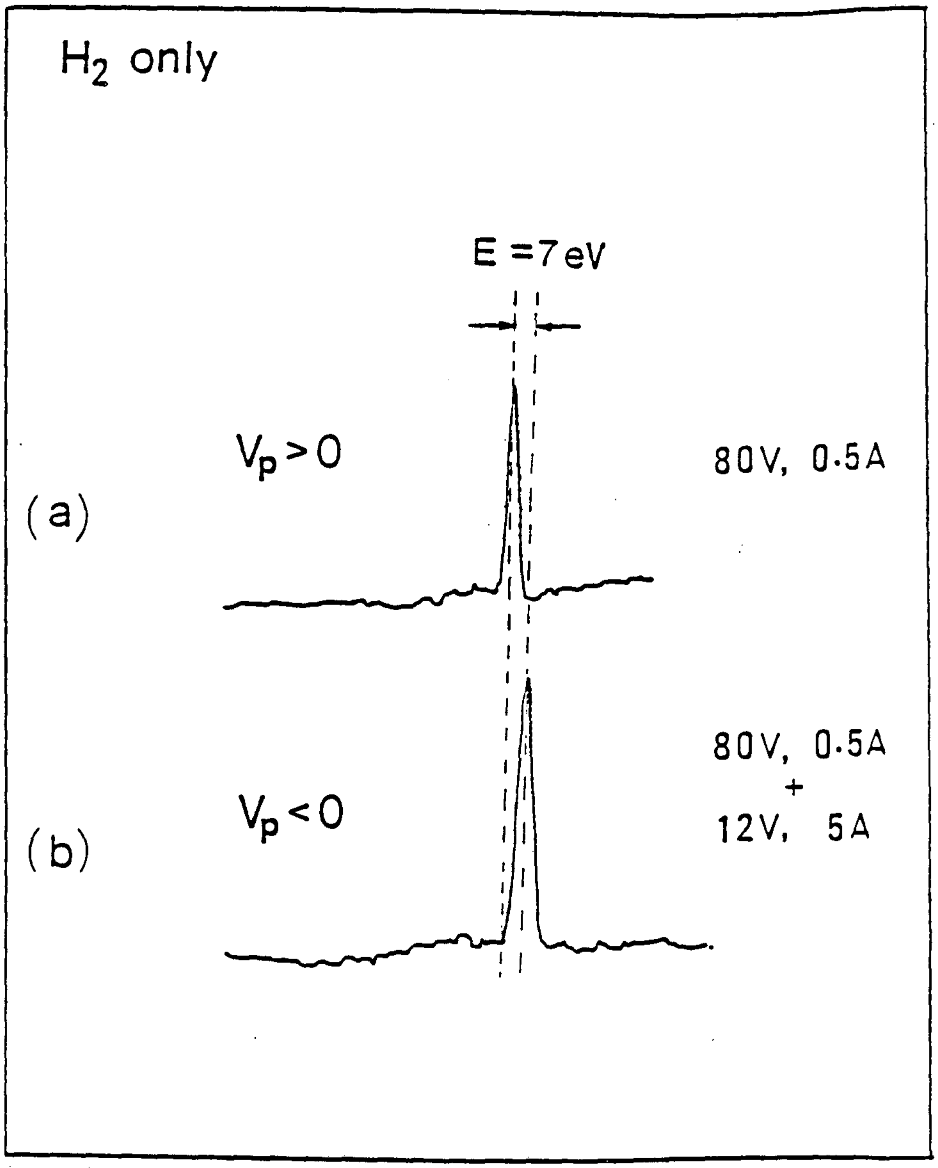

XBL 891—278

Fig. 6-6 A Plot of Mass Spectrometer Signals for operation with (a) a Positive Plasma Potential, and (b) a Negative Plasma Potential Produced by Injection Of Low Energy Electrons of 12 V and a discharge current of 5 A. Under this dual-cathode discharge condition, the plasma density in the source was found to increase by 62%. The H^- output signal, as shown in Fig. 6-6(b), also increased by about the same percentage. Thus, the enhancement in H^- output is directly proportional to the increase of the source plasma density. This result also indicates that vibrationally excited hydrogen molecules are unlikely to be formed via reflection of positive hydrogen ions on the anode walls.

The energy spectrum of Fig. 6-6 (b) also showed that the H^- ion peak has been shifted to the higher energy side. The increase in beam energy is due to the change in plasma potential before and after the injection of low energy electrons. The energy level diagram of Fig. 6-7 illustrates the relation between the energy of an H^- ion and the potential of the source plasma. If the plasma potential V_p is positive with respect to the anode and the H^- ion is generated in the plasma volume by a collisional process, then its energy $E = e(V_a - V_p)$ when it arrives at the detector, where e is the electronic charge and V_a is the extraction voltage. If the plasma potential V_p is negative, then the energy of the volume-produced H^- ion will become larger and the H^- peak will appear farther to the right or to the higher energy side of the spectrum.

On the other hand, if the H^- ion is born on the anode surface and the potential of the plasma in the source chamber is positive, then the energy of the H^- ion when it arrives at the detector will be $E = eV_a + \Delta E$ where ΔE is the amount of energy possessed by the H^- ion just when it leaves the anode surface. The actual H^- formation process on the anode surface has not yet been identified.

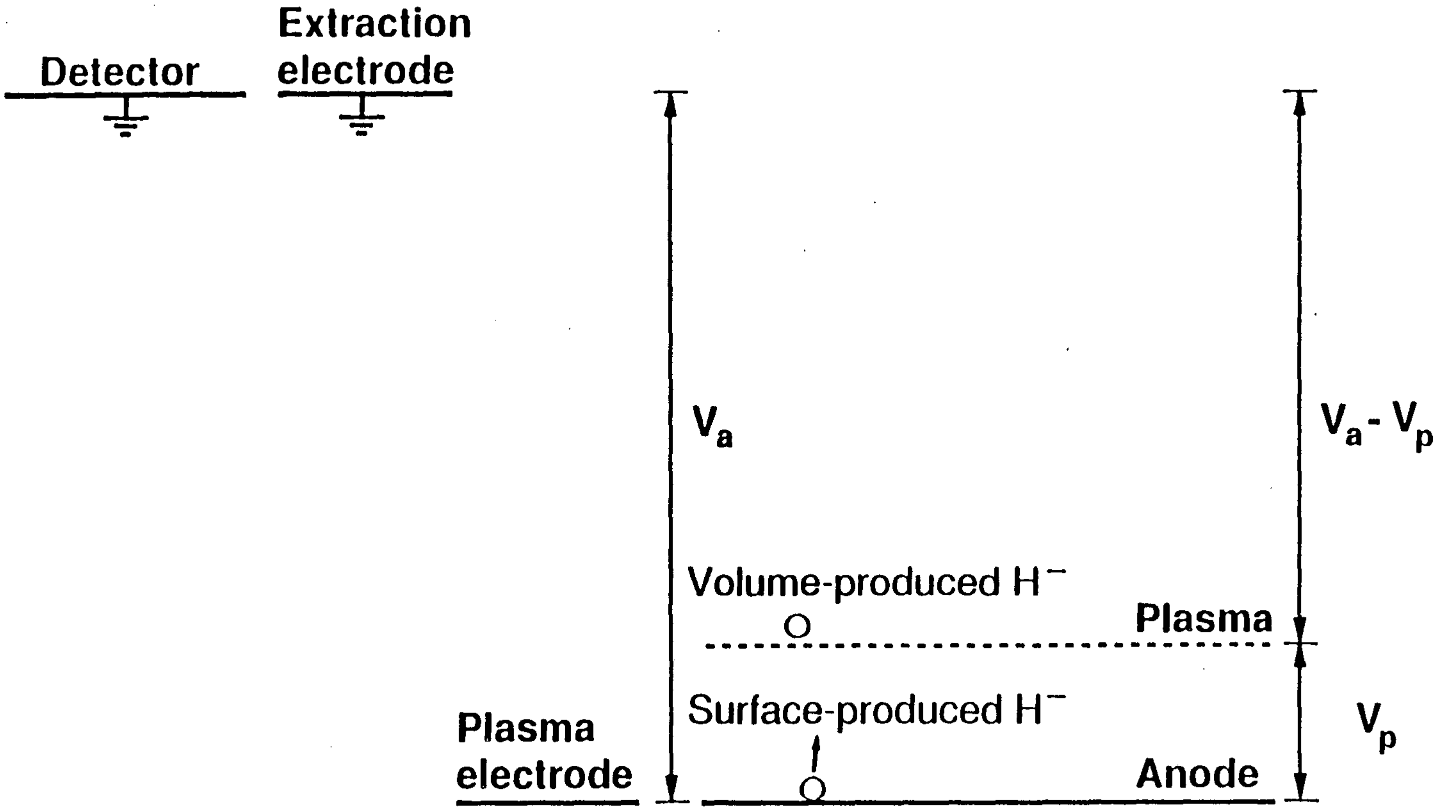

XBL 891—279

Fig. 6-7 An Illustration of the Relation Between the Energy of an H^- Ion and the Potential of the Source Plasma for Volume and Surface-Produced H^- Ions

If the H^- ion is generated by reflection of the positive hydrogen ion species,[86,87,88] then $\Delta E \leq eV_p$. If the H^- ions are formed by reflection of the neutral hydrogen atoms which include the Franck-Condon neutrals, then ΔE can be as large as 2 eV.[89] H^- ions can also be generated by a desorption process[90,91] on surfaces and the incoming projectile can transfer some energy to the adsorbed hydrogen atom. In all these cases, the majority of the H^- ions produced on the anode surface cannot reach the plasma volume if the potential of the plasma is sufficiently negative with respect to the anode. The H^- ions will be confined or trapped on the surface by the potential barrier and therefore cannot be extracted from the ion source. Only the volume-produced H^- ions will be extracted and subsequently detected by the mass spectrometer.

For a pure hydrogen discharge, the H^- output signal shown in Fig. 6-6(b) increased with the plasma density when the plasma potential became negative. It is also found that the increase in H^- energy (~7 eV) is equal to the overall change in plasma potential. Based upon this analysis, one can conclude that for pure hydrogen operation, the H^- detected in Figs. 6-6(a) and (b) are produced in the bulk of the plasma volume, most probably by the dissociative attachment process.[25,28]

Seeding of the hydrogen discharge with barium was carried out by placing some barium pellets on the liner. For this measurement, the source pressure was maintained at 2 mTorr and the background plasma was obtained with a discharge power of 80 V, 0.2 A from filament set (1). In this barium-seeded discharge, Langmuir probe characteristics showed that the plasma potential was ~1.5 V more positive than the anode. The spectrometer signal in Fig. 6-8 (a) demonstrates that the H^- output has increased by about a factor of 3 compared with pure hydrogen operation. A similar enhancement has previously been observed when H^- ions were extracted from a smaller multicusp source.[81]

In order to achieve a negative plasma potential, low-energy primary electrons were injected into the barium-seeded plasma. With filament set (2) operated at a discharge voltage of 4 V and discharge current of 2 A, the plasma potential at the source center was changed to ~1 V negative with respect to the anode. Under this discharge condition, the H^- peak in Fig. 6-8(b) is shifted to the higher energy side, similar to the result obtained for pure hydrogen operation. However, the H^- output signal is now reduced by a factor of 2.4 even though the plasma density has increased by a factor of ~2. This reduction in H^- output signal indicates that the majority of H^- ions observed in Fig. 6-8(a) are formed on the anode surface. When V_p becomes negative, the surface-generated H^- ions are unable to enter the plasma and only the volume-produced H^- ions can be extracted and detected by the spectrometer. The H^- signal decreases and it is not until V_p becomes positive that the H^- output can recover its original value of Fig. 6-8(a).

Part III Conclusion

The above observation demonstrates that surface-generated H^- ions are responsible for the large enhancement of the H^- output current when barium is added to a multicusp source. These results

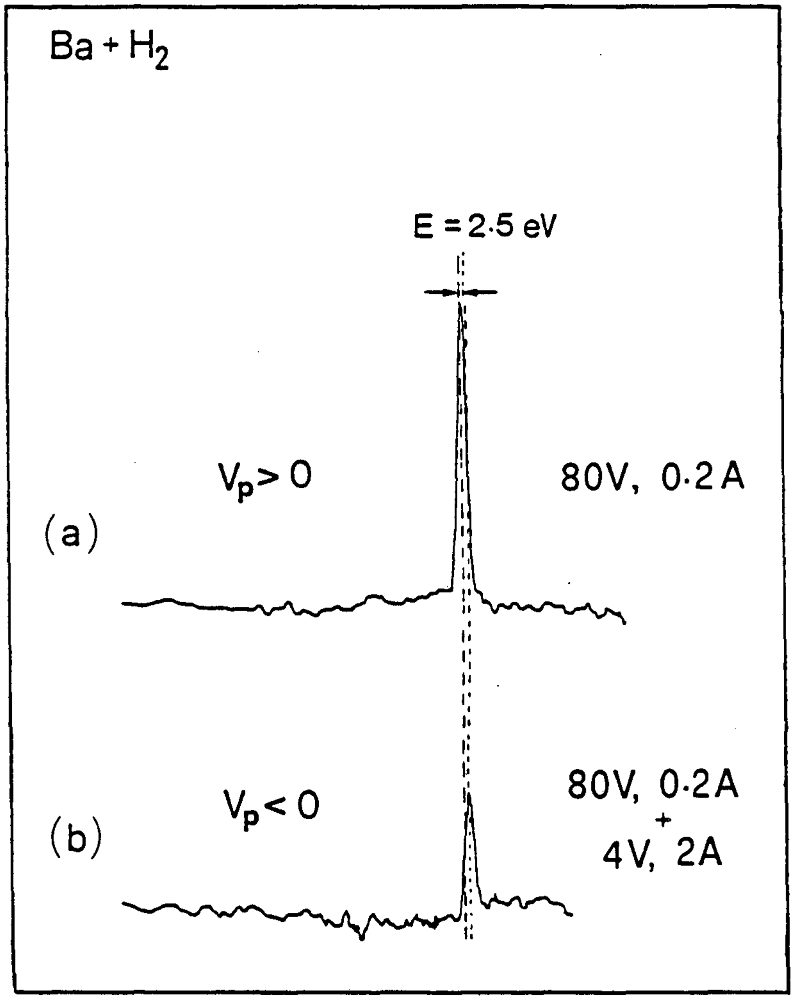

XBL 891-127

Fig. 6-8 A Plot of Mass Spectrometer Signals for Operation with (a) aPositive Plasma Potential, and (b) a Negative Plasma Potential Produced by Injection Of Low Energy Electrons into the Barium-Seeded Plasma are consistent with the observations of chapter 5. Hence, it is likely that H^- ions are formed on the anode walls for cesium as well as barium-seeded hydrogen discharges. It should be noted that the energies of the H^- formed on the anode surface can be quite different from those generated from a self-extraction type negative ion source.[21] In the latter configuration, a converter electrode with bias potential of -100 V or higher is employed. As a result, the average transverse energy of the "self-extracted" H^- ions is high (>5 eV).[92,93] In principle, the transverse energy of the H^- ions obtained from the barium-seeded source operation can be minimized by adjusting the potential difference between the plasma and the anode surface.

If the optimum liner temperature and barium coverage can be achieved during steady state operation, it appears that the H^- yield can be substantially improved. In that case, barium may in fact provide an enhancement in H^- output comparable to or even greater than cesium-seeded operation. The use of a temperature controllable liner, which does not rely entirely on discharge heating, may enable one to achieve the optimum liner condition and thus the best H^- output current. If this can be accomplished, then this new type of surface-production source can be used to provide large currents of high brightness H^- or D^- ion beams.

Chapter 7 Conclusion

Summary of Results

The intent of the experiments presented in the previous chapters was to improve the properties of negative ion sources for fusion applications. In the case of Li^- ions, production via volume processes had yet to be demonstrated in a discharge. The results of chapter 3 show not only that volume production of Li^- occurs, but that a volume discharge source of Li^- ions has sufficient current density to be useful for diagnostic applications. Chapter 4 details a proposed magnetic pitch angle diagnostic for the ITER tokamak conceptual design. This diagnostic uses a high energy Li° beam based on the Li^- ion source of chapter 3. Only modest improvements over demonstrated technology are assumed.

The lithium discharge has been adequately modeled using a rate equation approach in chapter 2. On the basis of the model parameter scalings, a significantly improved Li^- current density should be obtained by increasing the plasma density and neutral dimer fraction in the discharge. Li^- current densities in the range of 10 mA/cm^2 appear feasible. If this can be achieved, the possibility of using Li° beams for current drive should be investigated. The advantage of $^6Li^-$ based neutral beams versus D^- is that the energy required for equivalent beam penetration is three times higher. This allows the Li^- beam current to be reduced by a factor of three for the same energy deposition.

H^- ion sources are being intensively developed in order to address the problem of current drive in next generation tokamaks.

A viable H^- source must demonstrate steady state operation with a high H^- current density, low H_2 source pressure, and a low H^- ion transverse energy. Previous experiments on surface sources of H^- have shown that although the extracted current density is high; the negative ion transverse energy is also high.[21] These sources employed a converter biased at high negative potential to produce H^- ions.[21] Volume sources of H^- can produce negative ions with a low transverse energy, but at relatively low current densities and high H_2 source pressures.

The experiments of chapters 5 & 6 address this problem by using a new converterless surface H^- production geometry. In a barium-seeded discharge, it was demonstrated that H^- ions are predominantly formed on the anode walls. Experiments with a cesium-seeded discharge are consistent with this formation mechanism. Since the plasma potential is likely to be the dominant source of transverse energy for H^- ions, the emittance of an extracted H^- beam is expected to be good. The current densities achieved in a high power hydrogen discharge were significantly increased ($\geq$ factor of five) when cesium was added to the discharge. This result will allow the use of low H_2 source pressures while still obtaining high current densities. In addition, the fraction of electrons extracted with the H^- ions was reduced by a factor of ten for cesium-seeded operation.

Future Research Options

If pursued, further development of Li^- ion sources will allow extension of neutral beam based diagnostics to larger and denser fusion devices, and create a backup to D^- based current drive. Continued work on Li^- ion sources is needed to demonstrate steady state operation at high plasma densities, while maintaining or improving the dimer fraction in the ion source. The use of the lithium discharge model developed in chapter 2 should provide the information needed to produce a successful improved source design.

Continued work on the new type of surface production H^- ion source is certainly necessary. This type of source may provide the answer to the needs of neutral beam based current drive. There are many areas that require further exploration. The energy spread of the extracted H^- ion beam during cesium or barium-seeded operation needs to be measured, in order to confirm the suspicion that the transverse energy of the H^- ions in these sources is low. Operation of the barium-seeded discharge with low source H_2 pressures, at high power, and steady state, needs to be demonstrated. There exists substantial room for improvement. The best wall temperature and coating thickness should be investigated. The geometry of the ion sources was optimized for volume production. An ion source geometry relevant to H^- production on the anode surfaces should be designed. Thus, the outlook is promising for significantly improved H^- ion sources.

Appendix I Rate Constants for the Lithium Ion Source Model

This appendix details how the values of the various rate constants and other constants were evaluated. The dissociative attachment (D.A.) reaction is given by:

$$Li_2(v^*) + e^- \rightarrow Li + Li^-, \qquad (A1\text{-}2)$$

where $Li_2(v^*)$ denotes a vibrationally excited molecule. The 'rate constant' (k_d) is simply that given by McGeoch and Schlier without modification.[40] However, it should be noted that this 'rate constant' considers only low energy electrons (< 0.5 eV). Consequently, it is multiplied by a factor (S_1 or S_2) denoting the fraction of electrons with energies less than 0.5 eV. These factors are calculated by evaluating the fraction of electrons in this energy range for a maxwellian distribution of a specified electron temperature

The vibrational excitation of the lithium molecule by electron impact proceeds as:

$$Li_2 + e^- \rightarrow Li_2^* + e^- \rightarrow Li_2(v^*) + e^- + h\nu, \qquad (A1\text{-}2)$$

and has been analyzed by Wadehra and Michels.[29] The rate constant for this reaction (k_e) was also computed by McGeoch and Schlier.[43] Their rate constant included only the exothermic vibrational states for dissociative attachment. For H^-, the dissociative attachment cross section is also very large for endothermic states such as v =

6-9.[26,27] For lithium, the vibrational state equivalent to the $\nu = 6$ state in hydrogen was considered as the lowest state of importance for D.A. The equivalent state was determined by multiplying the threshold electron energy for D.A. in $H_2(\nu^* = 6)$ (1.0 eV), by the ratio of the molecular binding energies (1.06 eV/4.52 eV). This gives an equivalent threshold energy for the lithium system (0.234 eV), which corresponds to an energy just above $\nu = 5$ in lithium. Hence, all vibrational states from 6 on up are used to model the D.A. reaction for lithium. The rate constant (k_e), given by McGeoch and Schlier, was then multiplied by the sum of the cross sections for vibrational excitation of Li_2 to states from 6 on up (given by Wadehra and Michels), and divided by the sum of the cross sections of the states used by McGeoch and Schlier (10 on up). This gives a factor of 2.4 increase in the excitation rate constant used by McGeoch and Schlier ($5\text{x}10^{-9}$) resulting in $k_e = 1.2\text{x}10^{-8}$ cm^{3}s^{-1}.

Loss of vibrationally excited lithium molecules via wall collisions is given by a frequency $\Omega = 2\text{x}10^5/a$ cms^{-1}, where a is a characteristic dimension of the ion source.[40] This is simply used with a source dimension of 2 cm to obtain $\Omega = 1\text{x}10^5$ s^{-1}.

De-excitation of vibrationally excited lithium molecules by collisions with atoms proceeds as

$$Li_2(\nu^*) + Li \rightarrow Li_2 + Li, \qquad \text{(A1-3)}$$

with a rate constant k_R of $1\text{x}10^{-9}$ cm^{3}s^{-1} given by McGeoch and Schlier. This rate constant assumes complete de-excitation in a single collision. However, it is known that this process involves a statistical sharing of energies and that the lithium molecule on average retains 50-60% of the total energy as internal energy.[42] Considering that lithium atoms have some energy (~0.1 eV for evaporation at 1100 °K), and that the internal energy of $Li_2(v^*)$ is ~0.4 eV ($v = 10$), it appears that the internal energy lost by this process is small. As a conservative estimate, two collisions will be assumed effective in de-exciting $Li_2(v^*)$, which cuts the above rate constant in half and gives $k_r = 5\times10^{-10}$ cm^3s^{-1}.

Li^- ions can be lost by mutual neutralization

$$Li^- + Li^+ \rightarrow 2Li, \qquad (A1\text{-}4)$$

and by electron collisional detachment.

$$Li^- + e^- \rightarrow Li + 2e^- \ . \qquad (A1\text{-}5)$$

Mutual neutralization proceeds with a rate constant k_M of 1.5×10^{-7} cm^3s^{-1}.[44] This rate constant has not been modified from that used by McGeoch and Schlier. Detachment is important when energetic electrons are present. The cross section for this reaction is large[45] and results in a 'rate constant' k_d of 2.7×10^{-6} cm^3s^{-1} for electrons with energies of 5 eV or greater. The fraction of electrons with these energies in the first chamber is designated f_1, and is simply assumed to be ~0.05.

The velocities ascribed to the excited molecules and negative ions are important in order to calculate the average $Li_2(v^*)$ density in the second chamber, and the extracted Li^- current density respectively. The $Li_2(v^*)$ molecules are assumed to be in thermal equilibrium with the hot part of the wall surface of the ion source. This is reasonable since the hot part of the wall is the source of Li_2, and because of the short lifetime of Li_2 due to the high wall collision rate. The $Li_2(v^*)$ velocity ($\underline{v}$) is then calculated by computing the average velocity of a maxwellian distribution of Li_2 at the wall temperature. This average maxwellian velocity is given by:

$$\underline{v} = (8kT/\pi M)^{1/2}, \tag{A1-6}$$

where M is the mass of the particle of interest. In reality, the actual temperature of the $Li_2(v^*)$ molecules is not known, but the wall temperature is a good approximation.

The thermal or random velocity of negative ions in a discharge is not well understood. As previously mentioned in Chapter 2, there are many possible reasons for the high H^- ion temperatures commonly observed in extracted H^- ion beams. Since it is not the purpose of this thesis to solve this riddle, the negative ion temperature is simply assumed to be the same as the positive ion temperature (related to T_e). Although this is a common assumption in H^- ion source models, it is not presently justifiable in terms of the atomic physics. However, since the negative ions are formed in the spatially varying fringing magnetic field of the filter, it is likely that the ion temperature is dominated by the effects of the nonuniform space potential, which tends to scale with T_e. The velocity for the negative ion is then calculated in the same manner as for $Li_2(v^*)$ given above.

References

1 K. H. Berkner, R. V. Pyle, and J. W. Stearns, Nucl. Fusion 15, 249 (1975).

2 L. R. Grisham, D. E. Post, and D. R. Mikkelsen, Nuc. Technol. Fusion, 3, 121 (1983).

3 W. P. West, Rev. Sci. Instrum. 57, 2006 (1986).

4 W. P. West, D. M. Thomas, J. S. deGrassie, and S. B., Zheng, Phys. Rev. Lett., 58, 2758 (1987).

5 J. R. Trow, Ph. D. Thesis, University of California, Lawrence Berkeley Laboratory Report No. 19136 (1985).

6 W. S. Cooper, A. Faltens, and L. T. Jackson, Bull. Am .Phys. Soc., 32, 1748 (1987).

7 O. A. Anderson, L. Soroka, C. H. Kim, R. P. Wells, C. A. Matuk, P. Purgalis, W. S. Cooper, and W. B. Kunkel, Presented at the First European Particle Accelerator Conference, Rome, June 7-11, 1988; also Lawrence Berkeley Laboratory Report No. 25339.

8 J. Fink, Proceedings of the Fourth International Symposium on the Production and Neutralization of Negative Ions and Beams, p. 618, Brookhaven, 1983.

9 J. R. Trow, and K. G. Moses, Bull. Am .Phys. Soc., 32, 1748 (1987).

10 C. W. Drake and R. Kratkov, Phys. Rev. Lett., 16, 848 (1966).

11 E. B. Hooper and P. Poulsen, Proceedings of the II International Symposium on the Production and Neutralization of Negative Hydrogen Ions and Beams, p. 247, Brookhaven, 1977.

12 R. H. McFarland, A. S. Schlachter, J. W. Stearns, B. Liu, and R. E. Olson, Phys. Rev., A26, 775 (1982).

13 K. W. Ehlers, J. Vac. Sci. Technol. A1, 2, 974 (1983).

14 Yu. I. Bel'chenko, G. I. Dimov, and V. G. Dudnikov, Nucl. Fusion, 14, 113 (1974).

15 C. F. A. van Os, R. M. A. Heeren, and P. W. van Amersfoort, Appl. Phys. Lett., 51, 1495 (1987).

16 E. H. A. Granneman, J. J. C. Geerlings, J. N. M. van Wunnik, P. J. M. van Bommel, H. J. Hopman, and J. Los, Proceedings of the Third International Symposium on the Production and Neutralization of Negative Ions and Beams p. 206, Brookhaven, 1983.

17 W. G. Graham, Proceedings of the II International Symposium on the Production and Neutralization of Negative Ions and Beams, p. 126, Brookhaven, 1980.

18 M. Wada, R. V. Pyle, and J. W. Stearns, Proceedings of the Third International Symposium on the Production and Neutralization of Negative Ions and Beams, p. 247, Brookhaven, 1983.

19 J. R. Hiskes, Journal de Physique, 40, C7-179 (1979).

20 A. J. Freeman, E. Wimmer, S. R. Chubb, J. R. Hiskes, and A. M. Karo, Proceedings of the Third International Symposium on the Production and Neutralization of Negative Ions and Beams, p. 184, Brookhaven, 1983.

21 K. N. Leung and K. W. Ehlers, Rev. Sci. Instrum., 53, 803 (1982).

22 J. R. Hiskes and A. M. Karo, J. Appl. Phys., 56, 1927 (1984).

23 J. R. Hiskes, A. M. Karo, and P. A. Willmann, J. Appl. Phys., 58, 1759, (1985).

24 J. R. Hiskes, Comments At. Mol. Phys., 19, 59 (1987).

25 K. N. Leung and W. B. Kunkel, Phys. Rev. Lett., 59, 787 (1987).

26 M. Allan and S. F. Wong, Phys. Rev. Lett., 41, 1791 (1978).

27 J. M. Wadehra and J. N. Bardsley, Phys. Rev. Lett., 41, 1795 (1978).

28 J. R. Hiskes, J. Appl. Phys., 52,4592 (1980).

29 J. M. Wadehra and H. H. Michels, Chem. Phys. Lett.,114, 380 (1985).

30 J. R. Hiskes, A. M. Karo, and P. A. Willmann, J. Vac. Sci. Technol., A3, 1229 (1985).

31 I. Hall, I. Cadez, M. Landau, F. Pichou, and C. Schermann, Phys. Rev. Lett. 60, 337 (1988).

32 P. J. Eenshuistra, J. H. M. Bonnie, J. Los, and H. J. Hopman, Phys. Rev. Lett.,60, 341 (1988).

33 J. R. Hiskes and A. M. Karo, Proceedings of the International Ion Engineering Congress, p. 77, Kyoto, Japan, 1983.

34 R. Limpaecher and K. R. MacKenzie, Rev. Sci. Instrum., 44, 726 (1973).

35 Magnetic field computations made possible though use of a code authored by Dr. J. R. Trow.

36 F. F. Chen, Introduction to Plasma Physics and Controlled Fusion, vol. 1, p. 180 (Plenum 1984).

37 K. N. Leung, K. W. Ehlers, and M. Bacal, Rev. Sci. Instrum., 54, 56 (1983).

38 L. R. Grisham, D. E. Post, and D. R. Mikkelsen, J. Vac. Sci. Tech., 20, 1201 (1982).

39 W. P. West, Rev. Sci. Instrum. 57, 2006 (1986).

40 M. W. McGeoch and R. E. Schlier, J. Appl. Phys., 61, 4955 (1987).

41 J. P. Woerdman and S. S. Eskildsen, Chem. Phys., 65, 83 (1982).

42 J. C. Whitehead, Mol. Phys., 29, 177 (1975).

43 M. W. McGeoch and R. E. Schlier, Phys. Rev. A, 33, 1708 (1986).

44 B. M. Smirnov, Negative Ions, Chapter 5, McGraw Hill, 1982, New York.

45 Udit Narain and N. K. Jain, Can. J. Phys., 53, 1221 (1975).

46 K. N. Leung, private communication.

47 E. Schumacher, W. H. Gerber, H. P. Harri, M. Hofmann, and E. Scholl, Metal Bonding and Interactions in High Temperature Systems, Section 8, 83, American Chemical Society Symposium 179, Washington D. C. 1982.

48 S. R. Walther, K. N. Leung, and W. B. Kunkel, Appl. Phys. Lett., 51, 566 (1987).

49 A. N. Nesmeyanov, Vapor Pressure of the Chemical Elements, Elsevier Publishing Company, New York, 1963.

50 D. L. Doering and S. Semancik, Surf. Sci., 175, L730 (1986).

51 Gert Ehrlich, J. Chem. Phys. 31, 1111 (1959); and D. Olander, private communication.

52 V. K. Medvedev and T. P. Smereka, Sov. Phys. Solid State, 16, 1046 (1974).

53 K. W. Ehlers, K. N. Leung, and M. D. Williams, Rev. Sci. Instrum. 50, 1031 (1979).

54 C. F. Barnett, et. al., Atomic Data for Controlled Fusion Research, Oak Ridge National Laboratory, ORNL-5206.

55 K. N. Leung, K. W. Ehlers, and R. V. Pyle, Rev. Sci. Instrum. 56, 321 (1985).

56 C. H. Ma, D. P. Hutchinson, P. A. Staats, and K. L. Sluis, Rev. Sci. Instrum., 56, 911 (1985).

57 W. P. West, and D. M. Thomas, Rev. Sci. Instrum., 57, 1843 (1986).

58 A. S. Schlacter, J. W. Stearns, and W. S. Cooper, Lawrence Berkeley Laboratory Report No. 24235, Oct. 1987.

59 W. P. West, D. M. Thomas, E. S. Ensberg, J. S. deGrassie, and J. F. Baur, Rev. Sci. Instrum., 57, 1552 (1986).

60 R. D. Dubois, Phys. Rev. A, 32, 3319 (1985).

61 A. S. Schlacter, J. W. Stearns, and W. S. Cooper, Lawrence Berkeley Laboratory Report No. 25369, July 1988.

62 T. J. Dolan, Fusion Research, Vol. 1, p. 68, Pergamon Press, New York (1982).

63 A. I. Hershcovitch, B. M. Johnson, V. J. Kovarik, M. Menon, K. W. Jones, K. Prelec, and L. R. Grisham, Rev. Sci. Instrum., 55, 1744 (1984).

64 T. P. Wrangler and R. H. Stokes, IEEE Trans. Nuc. Sci., NS-28, 1494 (1981).

65 K. N. Leung, Private Communication.

66 R. M. Mobley, J. J. Brodowski, G. M. Gammel, J. T. Keene, A. W. Mashke, and R. T. Sanders, IEEE Trans. Nuc. Sci., NS-28, 1500 (1981).

67 K. N. Leung, K. W. Ehlers, C. A. Hauck, W. B. Kunkel, and A. F. Lietzke, Rev. Sci. Instrum.,59, 453 (1988).

68 S. P. Antipov, L. I. Elizarov, M. I. Martynov, and V. M. Chesnokov, Prib. Tekh. Eksp., 4, 42 (1984).

69 H. V. Smith, Jr., P. Allison, and J. D. Sherman, IEEE Trans. Nucl. Sci., Ns-32, 1797 (1985).

70 K. N. Leung, G. J. DeVries, K. W. Ehlers, L. T. Jackson, J. W. Stearns, M. D. Williams, M. G. McHarg, D. P. Ball, W. T. Lewis, and P. W. Allison, Rev. Sci. Instrum.,52, 235 (1987).

71 K. N. Leung, K. W. Ehlers, and R. V. Pyle, Rev. Sci. Instrum.,56, 2097 (1985).

72 S. R. Walther, K. N. Leung, and W. B. Kunkel, J. Appl. Phys., 63, 5678 (1988).

73 R. I. Hall, I. Cadez, M. Landau, F. Pichou, and C. Schermann, Phys. Rev. Lett, 60, 337 (1988).

74 P. J. Eenhuistra, J. H. M. Bonnie, J. Los, and H. J. Hopman, Phys. Rev. Lett, 60, 341 (1988).

75 J. R. Peterson, 4th International Symposium on the Production and Neutralization of Negative Ions and Beams, Brookhaven, 1986, AIP Conf. Proc. No. 158 (AIP, New York, 1987), p.113.

76 S. R. Walther, K. N. Leung, and W. B. Kunkel, J. Appl. Phys., 64, 3424 (1988).

77 K. N. Leung, C. A. Hauck, W. B. Kunkel, and S. R. Walther, Lawrence Berkeley Laboratory Report No. 25720 (Aug. 1988).

78 C. F. A. van Os, R. M. A. Heeren, and P. W. Amersfoort, Appl. Phys. Lett., 51, 1495 (1987).

79 C. F. A. van Os, C. Leguijt, P. W. Amersfoort, and J. Los, Proceedings of the III European Workshop on Production and Application of Light Negative Ions, p. 149, Amersfoort, Feb. 17-19, 1988.

80 A. Roth, <u>Vacuum Technology</u>, p. 159 (North Holland, New York, 1983).

81 S. R. Walther, K. N. Leung, and W. B. Kunkel, Lawrence Berkeley Laboratory Report No. 25788 (July 1988).

82 J. M. Wadehra, Phys. Rev. A., 29, 106 (1984).

83 B. Peart and K. T. Dolder, J. Phys. B., 8, 1570 (1975).

84 B. Peart, R. A. Forrest, and K. T. Dolder, J. Phys. B., 12, 3441 (1979).

85 K. N. Leung, R. D. Collier, G. R. Taylor, and R. E. Kribel, Appl. Phys. Lett., 31, 154 (1977).

86 J. R. Hiskes, A. M. Karo, and M. Gardner, J. Appl. Phys., 47, 3888 (1976).

86 P. J. Schneider, K. H. Berkner, W. G. Graham, R. V. Pyle, and J. W. Stearns, Phys. Rev. B., 23, 941 (1981).

87 J. N. M. van Wunnick, J. J. C. Geerlings, E. H. A. Granneman, and J. Los, Surf. Sci., 131, 17 (1983).

88 W. G. Graham, Phys. Lett. A, 73, 186 (1979).

89 M. L. Yu, Phys. Rev. Lett., 40, 574 (1978).

90 M. Seidl and A. N. Paragellis, Phys. Rev. B., 26, 1(1982).

91 M. Kaminsky, <u>Atomic and Ionic Impact Phenomena on Metal Surfaces</u>, (Springer, Berlin, 1965).

92 A. F. Lietzke, K. W. Ehlers, and K. N. Leung, <u>Proceedings of the 3rd International Symposium on the Production and Neutralization of Negative Ions and Beams</u>, edited by K. Prelec, AIP Conf. Proc. No. 111 (American Institute of Physics, New York, 1983).

LAWRENCE BERKELEY LABORATORY
TECHNICAL INFORMATION DEPARTMENT
1 CYCLOTRON ROAD
BERKELEY, CALIFORNIA 94720